Interdisciplinary Spectroscopy: The Detection and Characterization of Solar CMEs, Stellar CMEs, and Exoplanets

Citation
Wilson, Maurice. 2022. Interdisciplinary Spectroscopy: The Detection and Characterization of Solar CMEs, Stellar CMEs, and Exoplanets. Doctoral dissertation, Harvard University Graduate School of Arts and Sciences.

Permanent link
https://nrs.harvard.edu/URN-3:HUL.INSTREPOS:37371931

Terms of Use
This article was downloaded from Harvard University's DASH repository, and is made available under the terms and conditions applicable to Other Posted Material, as set forth at http://nrs.harvard.edu/urn-3:HUL.InstRepos:dash.current.terms-of-use#LAA

Share Your Story

The Harvard community has made this article openly available.
Please share how this access benefits you. Submit a story .

Accessibility

HARVARD UNIVERSITY
Graduate School of Arts and Sciences

DISSERTATION ACCEPTANCE CERTIFICATE

The undersigned, appointed by the

Department of Astronomy

have examined a dissertation entitled

Interdisciplinary Spectroscopy: The Detection and Characterization of Solar CMEs, Stellar CMEs, and Exoplanets
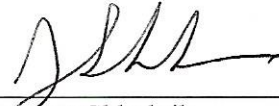
presented by

Maurice Wilson

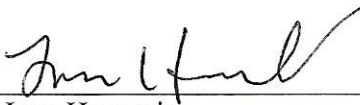candidate for the degree of Doctor of Philosophy, and hereby

certify that it is worthy of acceptance.
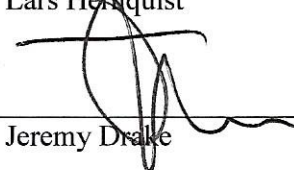
Signature _____

Typed name: John Raymond

Signature _____

Typed name: Jason Eastman

Signature _____

Typed name: David Charbonneau

Signature _____

Typed name: Evgenya Shkolnik

Signature _____

Typed name: Lars Hernquist

Signature _____

Typed name: Jeremy Drake

Date: April 28th, 2022

Interdisciplinary Spectroscopy: The Detection and Characterization of Solar CMEs, Stellar CMEs, and Exoplanets

A DISSERTATION PRESENTED
BY
MAURICE WILSON
TO
THE DEPARTMENT OF ASTRONOMY

IN PARTIAL FULFILLMENT OF THE REQUIREMENTS
FOR THE DEGREE OF
DOCTOR OF PHILOSOPHY
IN THE SUBJECT OF
ASTRONOMY AND ASTROPHYSICS

HARVARD UNIVERSITY
CAMBRIDGE, MASSACHUSETTS
APRIL 2022

Thesis advisors: John Raymond and Jason Eastman   Maurice Wilson

Interdisciplinary Spectroscopy: The Detection and Characterization of Solar CMEs, Stellar CMEs, and Exoplanets

Abstract

In the field of Astrophysics, spectroscopic instruments have become a foundational component of the observers' toolkit when studying starlight. The fundamental principles of spectroscopy can be applied ubiquitously throughout all subfields of Astrophysics. For the study of solar coronal mass ejections (CMEs), we use ultraviolet spectroscopic measurements to determine the plasma diagnostics for a CME. For the study of stellar CMEs, we make predictions for the feasibility of detecting CME-specific signatures from distant stars. For the study of exoplanets, we determine the degree of instrumental broadening in the optical spectral lines detected by a ground-based spectrograph that reveals exoplanet-induced Doppler shifts from bright stars. Within this breadth of research topics, the common denominator is our application of robust spectroscopic techniques to precisely detect a specific signal or precisely determine the characteristics of an astrophysical object of interest. Specifically, our exoplanet analysis focuses on the commissioning of an exoplanet observatory's spectrograph. We determine the stability of the fiber-fed KiwiSpec spectrograph belonging to the MINiature Exoplanet Radial Velocity Array (MINERVA). The instruments' stable conditions allow us to find the spectrograph's systematic noise floor. Our solar CME analysis makes use of a unique archival dataset from the Ultraviolet Coronagraph Spectrometer (UVCS) instrument on the *Solar and Heliospheric Observatory* (*SOHO*) spacecraft. The spectra from UVCS derived from the emission of the CME's prominence core plasma as it was observed at two heights in the corona. We use the spectra at both heights to constrain our modelling of the plasma's physical conditions, and thus, determine the energy budget as well as the rate of heating within the CME core. Our stellar CME analysis capitalizes off of the results of our solar CME analysis. Based on a few solar CMEs that have well-defined plasma diagnostics, we use the solar CME properties to estimate the brightness of its spectroscopic signal as if it belongs to a distant star system. We emphasize that three ultraviolet emission lines in particular would most likely be sufficiently bright to detect and would improve the credibility of interpreting the spectroscopic signatures as belonging to a stellar CME. We also suggest that the search for undeniably detected stellar CMEs should work in tandem with exoplanet surveys.

Contents

List of Figures

This is dedicated to the Link Unlimited Scholars, may the ambitious youth remain steadfast in their quest for knowledge and pursuit of higher education.

Acknowledgments

The works of this dissertation would not have been completed without the advice, guidance, compassion, and patience extended to me from my PhD advisors, Jason Eastman and John Raymond. I am grateful to Jason for believing in my ability to take on difficult research problems that initially felt foreign to me. His confidence in my potential to learn and solve the problems of our exoplanet instrumentation served to reinforce the confidence that I had in myself. This newfound confidence allowed me to remain calm and optimistic whenever we faced severe issues with the instruments' hardware and software that would take time to fix. It was truly an honor for me to see, with my own eyes, Jason's ability to remain calm under pressure as we tackled one problem after another for years on end. Being the pupil of Jason was an invaluable experience for me as I was still in the early stages of my development as a (student) scientist. Seeing his excellent, relentless, and selfless work ethic was a life-changing experience that molded my perception of what it means to be a "scientist" and "advisor." His exemplary character embodies the best qualities of academia, and the world would be a better place if more humans like him existed.

My desire to study the research problems of magnetic activity led me to yet another great advisor, John Raymond. Knowing that I had no experience in the field of solar physics, he was very patient with me as I spent a lot of time studying the historical context and standard techniques of the field. As a graduate student, this and all of my other time-consuming actions are subject to generating long-term consequences. Despite this, I remained confident in my ability to learn the craft and conduct excellent research on solar and stellar CMEs; but, this confidence stemmed from the consistent support and wise advice that I have been receiving from John since the first day that I met him as a third-year graduate student. Since then, my tedious pursuit of knowledge in a wide breadth of research topics felt manageable thanks to the many candid conversations I have had with John.

Additionally, I would like to thank the many collaborators of my instrumentation work and my magnetic activity work. Also, I have given many posters, talks, and colloquia over the years and I have appreciated each time an admirer of my talk would speak with me later and brainstorm with me on ideas that might improve my research. Those were short but significant moments that I cherished on a personal level.

Outside of research, my personal support is firmly found in the hearts of my mother, father, sister and brother. The often unsteady lifestyle of my graduate school career becomes easy to handle when the support and understanding of my family is unwavering. Regardless of the very difficult challenges I face in this profession, they have all faith and no doubt in my ability to make my dreams a reality. I am grateful also to the Emerson family for taking me under their wing for so many years and treating me like family every step of the way. I have learned and I continue to learn so much about the world that is outside of my narrow astronomy-focused gaze. I have become a more well-rounded individual thanks to the kindness and guidance extended to me by the Emersons. Even outside of my small sphere of social influence, I understand the professional world much better

now, and this has saved me from much confusion as I continue to navigate through the world of academia.

Throughout this PhD, there are many who have "stood in my corner" as I have faced adversity and have had to slowly but surely overcome many trials and tribulations. The astronomers of the Adler Planetarium are among those who have cared for my well-being and happiness. My success stems from the mentorship, emotional support, and helpful conversations that I have received from them and a plethora of more people whom I cannot all name here. Thank you all!

1

Introduction

Light detected by spectroscopic instruments is spatially dispersed according to its wavelengths. The recorded spectrum should mimic the wavelength-dependent output of radiation from the astrophysical object being observed. However, the spectrum recorded by instruments is never exactly the same as the spectrum radiated by the light source. The ambient medium and astrophysical objects between the Earth-based (or solar system-based) instrument and the observed light source will alter the electromagnetic radiation in some way before it is detected. Furthermore, the very act of recording the spectrum becomes a source of uncertainty that can alter the original signal that was radiated by the source.

Despite these astrophysical and instrumental sources of uncertainty, a precisely recorded spec-

trum can act as a "fingerprint" for the composition of the light source. If the nature of atomic transitions between quantum states is first understood in the laboratory, the radiation given off by certain atomic transitions can be compared to the radiation that is seen from the incredibly hot, magnetized, and electrically charged environment of a star.

In general, the fingerprint nature of the radiation manifests through the synergy of wavelength-dependent emission lines, absorption lines, and a broad continuum of emission. Such a spectroscopic fingerprint was once used by Payne (1925) to prove that the atmospheres of stars, including our Sun, were composed primarily of hydrogen and helium atoms. Since then, a much deeper understanding has been acquired of the Sun's chemical composition and the slightly different compositions of the Sun's atmospheric layers thanks to the enhancements of spectroscopic instruments.

Evidence from solar spectra suggest that as plasma rises from the photosphere and eventually reaches the corona, its photospheric chemical composition can change in the chromosphere and remain unaltered in the corona. This is revealed through estimates of the elemental abundances, which, among a variety of techniques, can be determined from observed photospheric absorption lines or coronal emission lines (Grevesse, 1984; Feldman et al., 1992; Raymond, 1999). The physical mechanism that is responsible for the height-dependent stratification in the elemental abundances is not understood. One clue to this mystery lies within the relationship between the change in elemental abundance and the first ionization potential (FIP) of the element's neutral atom. Known as the FIP bias, the magnitude of this vertical elemental fractionation differs between elements with a FIP lower than 10 eV and elements with a higher FIP. Without this FIP-dependent elemental fractionation, the ratio of elemental abundances between a low-FIP and high-FIP element would be same in the photosphere as it is in the corona. However, the ratios are usually different:

$$\left(X_L/X_H\right)_{\text{corona}} \neq \left(X_L/X_H\right)_{\text{photosphere}}, \tag{1.1}$$

where the relative abundance (X_L/X_H) between a low-FIP element (e.g., magnesium) and a high-FIP element (e.g., oxygen) can be estimated from the spectroscopic technique that uses the ratio of intensities between a strong spectral line for each element (Meyer, 1985; Feldman et al., 1998;

Raymond et al., 1997).

In addition to using spectra as fingerprints that identify the light source's composition, spectra can also be used to determine the behavior of the light source. When spectra are recorded repeatedly over time, the spectral lines that derive from a moving light source can exhibit a Doppler shift. The shifted frequency ν of a spectral line that was originally emitted a frequency of ν_0 can be expressed as

$$\frac{\nu}{\nu_0} = \left(\frac{c \pm v_{rec}}{c \pm v_{source}} \right), \tag{1.2}$$

which accounts for the speed of light in a vacuum c and the velocities of the light source v_{source} and an observer receiving the radiation v_{rec}. For an observer at rest ($v_{rec} = 0$), this expression can be simplified to

$$\frac{-\Delta\nu}{\nu_0} = \frac{\Delta\lambda}{\lambda} = \frac{v}{c} \tag{1.3}$$

as the light source travels at a speed v away from the observer that receives the redshifted radiation. If a slit spectrometer is used to observe the Doppler shift, this velocity information can be combined with the (one-dimensional) spatial information of the light source seen along the slit.

The conditions of the light source's environment can also be deduced from spectra. The different layers of the solar atmosphere exhibit different temperatures, densities, and ionization states within the radiating plasma that are observed. These plasma conditions can be diagnosed from the aforementioned intensity ratio technique. This is because atomic models (of the radiating plasma) have been constrained well by laboratory atomic physics experiments and recorded in CHIANTI database (Dere et al., 1997, 2019). The atomic models utilize the empirically derived transition rates for a plethora of prominent spectral lines. These atomic models make use of the rates of atomic excitation and de-excitation, which are coupled with the plasma environment's temperature, density, and ionization states. Thus, the intensities and intensity ratios can be modelled as functions of these plasma parameters.

The physical properties will evolve over time as the plasma flows through each layer of the solar atmosphere and eventually escapes the corona to join the solar wind. Due to the dense and dynamic environments in the solar atmosphere, it is difficult to find an individual, isolated clump of plasma

that can visibly be tracked and studied continuously while it is emerging from the solar surface to eventually escape the solar atmosphere. Tracking a specific plasmoid and monitoring the evolution of its properties becomes more feasible when the material belongs to a dense, bright coronal mass ejection (CME).

1.1 SOLAR CME SPECTROSCOPY

CME events occur after unstable magnetic field structures abruptly release free magnetic energy along with all of the plasma that was frozen-into the magnetic fields. These massive clouds of plasma can easily be tracked as they travel through the corona and out to the interplanetary medium. However, specific structures within the CME are still difficult to monitor since the morphology and thermodynamics of the CME bring about changes in its large scale bulk properties as well as the small scale properties that can distinguish one internal structure from another. Multi-band photometry and white light imagery have been used to estimate the CME's bulk properties, such as the mass and kinetic energy. Ultraviolet spectrometers have been used for the relatively small scale properties.

Photometry from white light coronagraphs detect the Thomson scattering radiation of the K-corona free electrons. As a result, the column density of the CME can be measured when it crosses the the coronagraph's field of view. The field of view captures the two-dimensional structure of the CME structure and when combined with column density can yield the CME mass. The CME's motion within a coronagraph's field of view gives the bulk velocity along the plane of sky (POS). Thus, a lower limit on the kinetic energy can be obtained.

Slit spectrometers provide little information regarding the geometry of the observed plasma, but plenty of the plasma properties can be derived. Assuming an optically thin corona, several ultraviolet emission lines from distinct ions can be used as intensity ratios to constrain the plasma ionization states. However, this usually assumes that both ions experience the same local conditions despite the spectra coming from radiation that is averaged along the line of sight (LOS).

For the environment's free electron density, the ratio between a forbidden emission line and an intersystem emission line can serve as a diagnostic. Such metastable states, particularly for the

forbidden transition line, have relatively slow rates of spontaneous decay (i.e., low Einstein-A coefficients). Consequently, the rate of collisional de-excitation is comparable. The emissivity from the collisional de-excitation is a density-dependent process while the spontaneous decay is not; therefore, the ratio between the two processes isolates the electron density and treats it as a free parameter that is constrained by the observed intensity ratio.

For the environment's electron temperature, the ratio between emission lines of very different wavelengths can be useful. This is a consequence of the Boltzmann distribution,

$$N_j \propto w_j e^{-E_j/k_B T}, \tag{1.4}$$

which describes the electron population of a given energy level j as being dependent on the statistical weight w_j, the energy E_j of the jth atomic level, and the thermal energy $k_B T$. Since the intensity of a given transition line is directly proportional the Boltzmann (exponential) factor, the intensity ratio between emission lines of the same ion would depend on the following expression,

$$\frac{I_{g,j}}{I_{g,k}} \propto \exp\left[\frac{\Delta E_{g,k} - \Delta E_{g,j}}{k_B T}\right], \tag{1.5}$$

which shows the ratio between the intensity of two emission lines the are excited from the ground state g and later spontaneous decay from the excited state of either j or k. The difference between the change in energy levels ΔE corresponds to a difference in frequencies. In order for the temperature-dependent exponential factor to have a significant influence on the intensity ratio, the exponential factor (i.e., the exponential function of temperature) becomes more dependent on temperature as it takes on a larger value:

$$\frac{\Delta E_{g,k} - \Delta E_{g,j}}{k_B T} >> 1. \tag{1.6}$$

These spectroscopic techniques for deducing plasma properties can be applied to solar CMEs observed by spectrographs. The diagnostic capabilities of these techniques should be considered when searching for stellar CMEs and characterizing their plasma properties.

1.2 Stellar CME Spectroscopy

The aforementioned Doppler shift method has been used extensively in the search for CMEs. Similarly, the presence of asymmetric line profiles indicates the bulk motion of plasma along the LOS. Gunn et al. (1994) discerned asymmetric line profiles for Ca II H and K as well as for Balmer lines like H_δ in the spectra of the M dwarf star, AT Mic. A broadened blue-wing excess in the line profiles indicated Doppler velocities of $\lesssim 600$ throughout the duration of a flare. They interpreted this as the bulk motion of a large mass flow of chromospheric material.

Vida et al. (2019) searched through more than 5500 spectra to find CME-related line asymmetries in the Balmer lines of M dwarfs. They found 478 asymmetries with corresponding maximum velocities in the range of 100-300 km s^{-1}, which were mostly slower than their respective host star escape velocities.

In the context of stellar CMEs, the Doppler and line asymmetry techniques are subject to uncertainties from projection effects, rotational modulation, and non-CME plasma flows. The CME interpretation becomes less credible when the measured velocities are in agreement with the rotational velocity the star. Also, as illustrated by Moschou et al. (2019), projection effects permit the presence of redshifts (or red wing asymmetries) being correctly interpreted as the propagation of a CME travelling partially away from the observer. However, redshifts of a few hundred km s^{-1} can be the product of confined (i.e., "failed") CMEs or flare-induced chromospheric plasma flows (Teriaca et al., 2003; Joshi et al., 2013). These potential uncertainties and misinterpretations can be problematic for those who hunt for stellar CMEs while simultaneously giving hope to those who hunt for habitable exoplanets that just so happen to orbit the many low mass, cool stars within our solar neighborhood.

1.3 Star-Planet Spectroscopy

Among the low mass, cool stars have have captured the interest of the exoplanet community, late-type M dwarfs are known to have strong and frequent magnetic activity phenomena that may excite CME-seekers but discourage habitable exoplanet-seekers. Active M dwarfs can pose a problem

for the detection and characterization of exoplanets. Various forms of stellar magnetic activity can limit the precision that is required to confidently deduce the physical properties of the exoplanet that is orbiting the observed target star. Such magnetic phenomena is typically considered to be astrophysical "noise" or stellar "jitter" for exoplanet-enthusiasts but, conversely, is considered to be astrophysical "signal" or stellar "activity" for flare-CME-enthusiasts.

The activity, or noise, that can exacerbate the characterization of a newfound exoplanet can be seen in the observation runs that utilize the radial velocity method. As an exoplanet follows a Keplerian orbit about its host star, the gravitational influence induces a stellar wobble. This is indicated through periodic Doppler shift measurements that represent the wobbling star's radial velocity motion along the LOS (e.g., Campbell et al., 1988).

The periodic signal can be contaminated by the radial velocity motion of the host star's pressure waves (p-modes). For solar type stars, the convective envelope can induce surface oscillations from turbulent convection over timescales of a few minutes. The periodic noise can have amplitudes of tens or hundreds of cm s^{-1} that, when in phase, can introduce a radial velocity contamination of several m s^{-1} (e.g., Broomhall et al., 2009).

On the timescale of about 10 minutes, other solar convective motions can contaminate the radial velocity signal via granulation. Plasma flows in the outer layer of the convective envelope can introduce photospheric cells of relatively bright upflows and dark downflows. When the spectral signal is not averaged over the plasma's periodic brightenings (heating) and dimmings (cooling) or blueshifts and redshifts, the contamination can have radial velocity amplitudes of about 1 km s^{-1} (e.g., Dravins, 1990).

Magnetic activity cycles, such as the 11-year sunspot cycle, can also act as a source of noise for the radial velocity signal. On the timescale of years, the number of sunspots and active regions that cover the solar surface varies. Therefore, the brightness and spectral (activity) signatures vary as well and can limit the precision obtainable by the spectroscopic radial velocity method (e.g., Wilson, 1978).

1.4 Overview

As an arbitrary choice of words, my use of "we" will describe the implicit and explicit support that was collectively given to me throughout the making of these research findings. *We* (or the term *our*) includes all of those who have collaborated directly with me, as well as those who have indirectly helped by sharing their knowledge with me via word of mouth (e.g., colloquium) or written word (e.g., paper publication) or other forms of media.

The contents of this dissertation include three research studies that make use of spectroscopic techniques to learn more about various astrophysical objects of interest. The studies are discussed in chronological order of when the study was undertaken: the exoplanet instrumentation work is first (in §2), the solar CME work is second (in §3), and the stellar CME work is third (in §4). "Our" final remarks regarding these topics are given in §5.

2

First radial velocity results from the MINiature Exoplanet Radial Velocity Array (MINERVA)

The discovery of the first planets orbiting solar-type stars was achieved using Doppler spec-

troscopy (Campbell et al., 1988; Latham et al., 1989; Mayor & Queloz, 1995). As the first exoplanet detections and confirmations were made, Doppler spectroscopy instruments gradually improved from attaining a radial velocity (RV) precision of $\sim$15 m s^{-1} (Campbell et al., 1988) to $\sim$3 m s^{-1} (Butler et al., 1996) thanks to the advent of the iodine absorption cell technique. Two decades later, the next generation of precision RV instruments aims for instrumental stability at the 30 cm s^{-1} level (Wright & Robertson, 2017). However, our sensitivity to exoplanets is likely limited by stellar activity at the $\sim$1 m s^{-1} level for most stars (e.g., Saar & Donahue, 1997; Haywood et al., 2016). Detections below this level will not be achieved until astrophysical noise sources are understood as well as sources of instrumental noise. Observing with high cadence throughout a planet's full orbit may allow us to understand and correct for non-planetary RV signals induced by stellar activity (O'Toole et al., 2008; Pepe et al., 2011; Dumusque, 2012).

The MINiature Exoplanet Radial Velocity Array (MINERVA) is a dedicated observatory aiming for both high cadence and high precision RV measurements (Swift et al., 2015). It is a robotic array of four 0.7 m telescopes located on Mt. Hopkins in Arizona. The MINERVA mission ultimately has two objectives.

The primary science objective is to detect and characterize super-Earths in the habitable zones of nearby stars. Our RV target list is a subset of the targets monitored during the NASA/UC $\eta_{\oplus}$ Survey performed by the California Planet Search (CPS) group at the Keck Observatory using the HIRES spectrograph (Howard et al., 2009). Out of the 230 GKM stars they surveyed, 166 are considered chromospherically quiet (Wright et al., 2004; Isaacson & Fischer, 2010). The MINERVA RV target list consists of 125 of the brightest ($V \lesssim 8$) chromospherically quiet stars from their survey that can be observed from southern Arizona. With MINERVA's effective aperture of 1.4 m and use of the NASA/UC $\eta_{\oplus}$ targets, the RV precision goal of the MINERVA mission was set to detect planets at the 80 cm s^{-1} level (Swift et al., 2015). At this level, we plan to characterize super-Earths while providing insight into the importance of cadence as a tool for understanding the problem of stellar activity. We show that we are about a factor of 2 of that goal in §2.7.1, which is already within the top tier of the current generation of precision RV instruments. Coupled with our unmatched observational cadence, we are already operating in a unique parameter space that will enable us to

detect new planets and provide valuable insight about the importance of cadence in understanding stellar jitter. We can do this with our cost-efficient, four-telescope, robotic array observing at an unprecedented cadence. The high cadence is attributed to the autonomous, flexible target scheduling, and quick slewing of the CDK-700 telescopes. Most importantly, the majority of the robotic array's time is not split between multiple teams or science goals.

The secondary science objective is to search for transits of the super-Earths we find. This requires a broadband photometric precision of <1 mmag in the optical: a goal that has already been demonstrated by Swift et al. (2015). Multiband light curves provide information that otherwise cannot be deduced from Doppler spectroscopy alone. For example, the minimum mass of the planet can be found from radial velocities, but if the planet happens to transit, the transit photometry can determine the radius and inclination of the planet (see, e.g. Winn, 2010). Therefore, both exoplanet detection methods used together can indicate the true planetary mass and bulk density.

MINERVA's secondary objective has already contributed to a variety of exoplanet science endeavours (Swift et al., 2015; Vanderburg et al., 2015; Croll et al., 2017; Lund et al., 2017; Pepper et al., 2017; Rodriguez et al., 2017; Siverd et al., 2018; Labadie-Bartz et al., 2019). Thus, in this work we focus on the commencement of MINERVA's primary objective. We report our survey performance in §2.1, the changes to our hardware since our last paper in §2.2, the environmental stability of the spectrograph in §2.3, our revised telescope control software in §2.4, our one-dimensional extraction in §2.5, our Doppler pipeline in §2.6, our first RV results in §2.7, and our final remarks in §2.9.

2.1 Survey Performance

Observing at Mt Hopkins is divided naturally into seasons by the July/August monsoon shutdown. The first full-season MINERVA observing campaign in radial velocity survey mode began 2017 September 14 and ran through 2018 June 29. Spectra were obtained on 196 of 293 nights. Weather prevented observations on 44 nights, and 53 nights were spent on engineering or lost to system malfunctions. We obtained 1936 exposures with 4 spectra each of 28 survey target stars, with a maximum of 222 exposures of a single (high decl.) target. Fourteen targets had at least 60 exposures. In

addition, we obtained 199 exposures of hot stars, at least one per night, used for spectral calibration. A typical night full of observing led to 12 to 19 exposures (most in December, less on shorter nights) of 8 to 10 target stars. The open shutter fraction was highly variable at the beginning of the season, but stabilized at $\sim$ 69% after implementation of the autonomous scheduler in late October. Given the rapid slewing and settling time of our telescopes, the majority of the overhead per spectrum was the result of robotic target acquisition on the fiber tip.

The 2018-19 observing campaign began 2018 October 15 and is in progress at the time of writing this manuscript. Through 2019 March 31, spectra have been obtained on 107 of 168 nights, with 35 nights lost to weather and 26 spent on engineering or lost to system malfunctions. We have obtained 1455 exposures with 4 spectra each of 19 survey target stars, a 32% increase in spectra obtained over the same period from the previous season. Twelve targets have at least 60 exposures thus far. In addition we have obtained 137 exposures of hot calibration stars. Changes in our acquisition algorithm have reduced the overhead, resulting in an average open shutter fraction of 86% since 2018 November. Historically, April through June provide very reliable weather at the site (in 2018-2019 we lost only 3 of these 91 nights to weather), and we anticipate that this observing season will lead to a larger set of RV data than the previous season — 43% of our 2017-18 spectra were obtained in April–June.

2.2 HARDWARE

The overall hardware design for the MINERVA facility has remained largely unchanged from that described in Swift et al. (2015). However, we have made several changes to improve our science capability, which we discuss in detail below.

2.2.1 FIBER ACQUISITION UNIT (FAU) CAMERAS

The SBIG ST-i cameras originally used in the FAUs had two major problems. First, their small field of view ($3'.6$ x $2'.7$) coupled with a surprisingly quick degradation of the telescope pointing meant that we could not blindly point to a target and be confident it would fall on the detector. We had

to redo the pointing model weekly to ensure the pointing was sufficient for robust acquisition—a time-consuming task that must be done manually at night, when the telescopes would otherwise be carrying out science observations. The source of the pointing degradation is not clear, and the telescope manufacturers have not seen such degradation for other users, suggesting a problem with the robotic control software that we have not been able to fully investigate.

Second, the SBIGs had a high failure rate. During the initial month-long spectrograph commissioning, three out the four cameras in use experienced critical failures.

The manufacturers were aware that this problem affected a small batch of cameras and repaired them. After those repairs, the cameras performed better, but over the three years that followed, several more failures occurred. Given that replacing a failed camera requires a site visit, at a cost significantly greater than that of the cameras themselves, we decided to replace the SBIG cameras with ZWO ASI 174 cameras.

In the six months of daily use on four telescopes since their installation, we have not had a single camera failure. These cameras have a CMOS detector with 1936 x 1216, 5.86 μm pixels, and is similarly priced. This provides us an 8.5' x 5.4' field of view that allows us to robustly acquire our targets despite the pointing degradation of the telescopes. One downside to these cameras is that they are incompatible with our Black Box USB extenders, and so we had to move our control computers into the domes in order to use them.

2.2.2 Fiber

The science fiber was originally purchased from CeramOptec and has a 50 μm octagonal core and 330 μm cladding. As is typical for CeramOptec, they actually have two slightly different claddings for octagonal fibers – one deposited onto the octagonal core to make it circular, and another with the core drilled out that they plug in with the circularized octagonal core. As was the case with our fiber, the boundary between the two claddings can be problematic if the indices are not well matched, since it can guide starlight through the cladding. Light transmitted through the cladding reduces the resolution of the spectrograph and the instrumental profile can vary dramatically as a function of how much light couples with the cladding—both of which are catastrophic for preci-

sion RV measurements. In addition, the cladding was too large to pack together at the focal plane with the required core-to-core spacing, and the standard Ferrule Connector (FC) connectors at each end, done by CeramOptec, suffered from severe Focal Ratio Degradation (FRD) and thus led to a major loss in throughput.

As a short-term solution, we re-terminated the original fibers to improve the FRD, and coupled the fibers into a short section of fiber with a 50 μm circular core and a 125 μm cladding to remove light from the cladding of the octagonal fiber. One side is butt-coupled to each of the four telescope fibers, and the other four ends combine into a V-groove at the spectrograph end, spaced 220 μm center to center.

As a long-term solution, we ordered a new fiber with a custom preform (a macro-sized piece of glass from which the fiber is drawn), which had a 50 μm octagonal core and 110 μm cladding from Polymicro, with the intention of packing seven of them cladding to cladding to allow for future expansion should we decide the significant ($\sim$ 10%) crosstalk from such tightly packed fibers is manageable. Polymicro deposits the entire cladding onto the octagonal core to avoid the secondary cladding issue. However, our cladding was much thicker than typical, and during the lengthy deposition, the core melted and mixed into the cladding, creating the same effect as a secondary cladding. Light was still transmitted through the cladding of the fiber. A second attempt was no better, at which point they would not attempt the expensive process again. We could not afford a thinner cladding because we split the expensive custom preform with two other groups that required a thicker cladding.

So, our short term solution has become our final fiber solution. While the butt-couple is lossy, it makes the installation easier, it provides an easy point to add a double scrambler if we decide it is necessary in the future, and a change in the fiber geometry improves the near-field scrambling (Halverson et al., 2015). Meanwhile, MINERVA Australis (Addison et al., 2019) has created a fiber similar to our desired long-term solution, with enough for a spare if we decide it is worth the effort to replace in the future.

2.2.3 Spectrograph

The KiwiSpec spectrograph was installed in 2015 December, and is a commercial adaptation of the spectrograph designed and described in Barnes et al. (2012) and Gibson et al. (2012), with a new camera designed by Prime Optics[*]. With a few exceptions highlighted below, it is as we described in Swift et al. (2015). Instead of the simultaneous etalon or thorium argon wavelength reference described in Swift et al. (2015), we used the thorium argon lamp during the installation as a rough wavelength solution and now rely solely on the iodine to provide the exact wavelength solution. The simultaneous wavelength reference in addition to iodine is unnecessary, and removing them allowed us to reduce the scattered light and increase the spacing between fibers, reducing the crosstalk to $\lesssim 0.1\%$.

We determined our total system throughput to be $\sim 5\%$ using Doppler Tomography observations of KELT-24b without the iodine cell (Rodriguez et al., 2019). We computed the expected flux from the V=8.33 host star between 6175-6185 Å and compared it to the actual flux in the extracted 1D spectrum at the same bandpass (at the peak of the blaze). This throughput estimate includes all losses, including the atmosphere, coatings, beam splitter, fiber coupling, Echelle, and charge-coupled device (CCD).

Light from each of the four telescopes is focused directly onto our 50 μm octagonal fibers at f/6.6 in our FAU (see §2.2.1). Three meters before the spectrograph entrance, each of the fibers are butt-coupled to circular 50 μm fibers, which are then arranged into a V-groove at the entrance to the spectrograph, separated by 220 μm center to center. The light exits the four fibers and is collimated. A pupil mask truncates the beam to ensure the beam is precisely f/6, allowing for some focal ratio degradation within the fibers. The collimated light travels to the iodine stage, where the iodine gas cell can be moved into or out of the beam. The fibers are then re-imaged onto the entrance slit, and the light follows the path to the detector shown in Figure 1 of Barnes et al. (2012).

We empirically determined the resolving power per resolution element of the spectrograph by forward modeling high signal to noise spectra taken of the daytime sky and numerically solving for

---

[*]http://www.primeoptics.com.au/

the FWHM of the fitted IP for each chunk. As expected, there is a slight wavelength dependence in our resolving power. The best-fit line of the resolving power per resolution element as a function of wavelength is $R = 84,000 + (\lambda - 5500\text{Å}) \times 10/\text{Å}$, in good agreement with our theoretical expectation. We also plot the best-fit dispersion per resolution element as a function of wavelength for each chunk in Figure 2.1 for a representative night on a representative telescope.
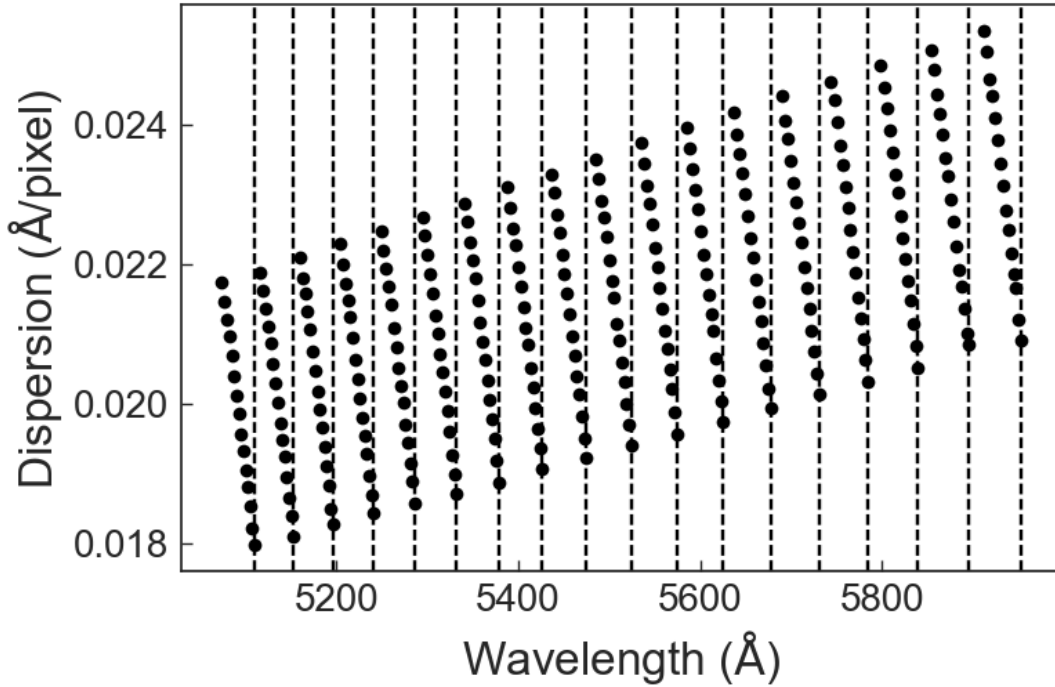
Figure 2.1: The dispersion fitted for each chunk (black points) that we use to extract the radial velocity as a function of wavelength, for a representative night on a representative telescope. The variance of the dispersion over time and for different telescopes is much much smaller than the size of the data points in the figure. The vertical dashed lines represent the edge of each order.

2.2.4 EXPOSURE METER

We have always had an exposure meter inside the spectrograph that picks off the reflection of the nearly collimated beam from the vacuum window. We have since added a V-band filter to approximate the bandpass of the spectrograph. The major downside to this design is that the exposure meter reports an average flux from all four telescopes, so we cannot use it to apply a per-telescope barycentric correction. Instead, we use the guide images from the FAU (at $\sim$5 s cadence), with an

aperture the size of the fiber drawn around the measured fiber position to determine the relative flux during the exposure for each telescope. We have confirmed that, when only one telescope is used, we can use the FAU guide images reproduce the relative exposure meter flux to within the uncertainties, in order to compute a per-telescope barycentric correction.

2.2.5 Backlight

The FAU design described in §2.2.1 and Swift et al. (2015) flexes depending on its rotation angle and the telescope's altitude. This flexing causes the apparent position of the fiber on the acquisition camera to move by $\sim$ 10 μm over the sky—or 20% of the fiber diameter, which would be a significant source of light-loss if left uncorrected. We knew this would be a problem and the FAU was designed to be able to locate the fiber tip on the acquisition unit by backlighting the fiber, but we had not yet fully fleshed out a solution at the time we wrote the Swift et al. (2015) paper. We considered using the exposure meter to refine the star's position, but that would dramatically increase our acquisition time since it would have to be done serially with each telescope and it can be difficult to make such a procedure robust during variable weather conditions. Ultimately, we added a disk of LEDs that swings in front of the V-groove to illuminate the fibers from inside the spectrograph. We do this before each exposure to refine the reference pixel to move the star to, and after to evaluate how much throughput might have been lost due to drift during the exposure. By evaluating a large number of these backlight images, we may be able to map the flexure and eliminate this step and/or compensate for drift during an exposure in the future.

2.2.6 Slit flat

Because the fibers do not provide much signal to noise in the wings of their profile, it is difficult to determine the pixel-to-pixel variations in the spectrograph detector with flat fields illuminated through the fiber. We added a light, mounted on the iodine stage, that illuminates a slit where the fibers are re-imaged. We use this flat field to correct for the pixel to pixel variations in the detector, as described in §2.5. The flat field lamp simply shines onto the entrance slit, with no attempt to match

the *f*/6 science beam. We see no significant scattered light contamination with this approach, but we have yet to perform a detailed investigation.

While our iodine cell was designed to have counter-rotated wedges to eliminate fringing with minimal beam deflection, we believe the parallelism of the iodine cell faces was not within specification. As a result, when the iodine cell is in place, the position of the fibers shifts by almost the entire diameter of the fiber in the dispersion direction. Originally, the slit was only slightly oversized relative to the fiber size. We replaced it with a much wider slit to accommodate both the undeflected and deflected beams. While this significantly degrades the resolution of our slit flat fields, the flat only varies slowly as a function of color and its change across the degraded resolution is negligible. The resolution of our science images is set by the fiber size, not the slit width and therefore widening the slit has no impact on our science images.

Figures 2.2a and 2.2b show the cross section of the bluest and reddest orders, respectively, of the slit flat (without the iodine cell) overlayed on the same cross section of a daytime sky spectrum (with the iodine cell) to show that the slit flats give us adequate signal to calibrate the pixel to pixel variations under the science fibers, despite the deflection of the science fibers due to the iodine cell.
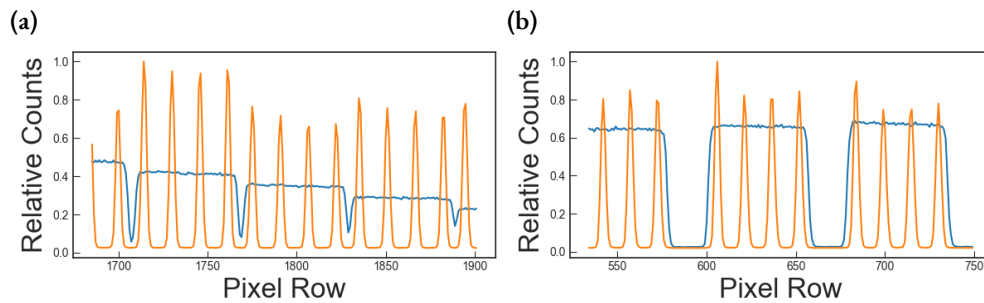
Figure 2.2: The blue lines show a normalized cross section of the slit flat calibration image. In orange, we overlay the same cross section of the normalized traces in the science frame taken the same day, showing that the slit flats give us adequate signal to calibrate the pixel to pixel variations under the science fibers. Figure 2.2a shows the most crowded orders at the blue extreme, and Figure 2.2b shows the least crowded orders at the red extreme, showing that we have adequate signal and sufficient separation at both extremes.
(A color version of this figure is available in the online journal.)

2.3 Spectrograph environmental performance

Here we show the pressure stability of the spectrograph (Figure 2.3a) from 2017 March through 2018 July at 3 s intervals. It should be noted however that during 2017 mid-April, a power outage occurred at the MINERVA facility. Typically, the spectrograph is continuously pumped, but the outage caused the valve from the pump to the spectrograph to close, which went unnoticed for an extended period of time (mostly during the monsoon when we were not operational). We have since implemented a watchdog that sends an email notification if the pressure rises above 10 μbar (see §2.4). This power outage resulted in a swift increase in pressure as it leaked up toward atmosphere. By early October, the pressure once again became sufficiently stable for the collection of good quality data, and remained so through 2018 July aside from some minor fluctuations due to maintenance. Figure 2.3b shows this stability over the month of 2018 March with a RMS of 0.065 μbar (dramatically exceeding our requirement of 12 μbar).

(a)   **(b)**
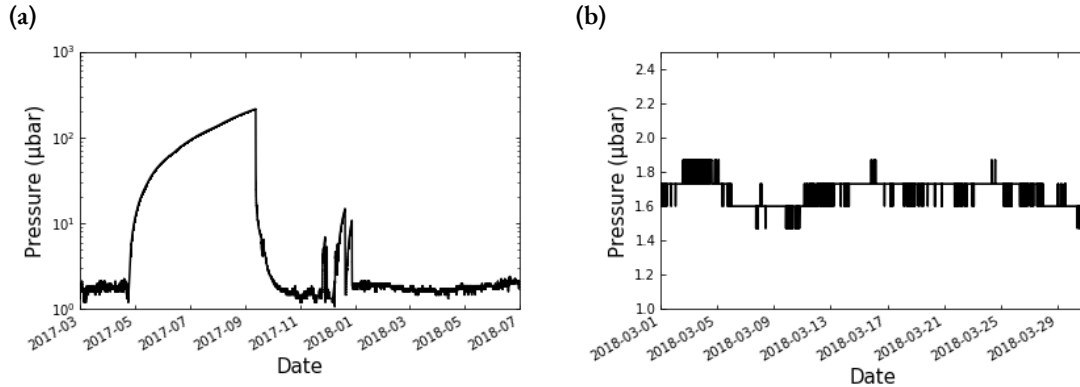
Figure 2.3: Spectrograph pressure inside the KiwiSpec spectrograph. The plotted measures were taken between 2017 March and 2018 July. A power outage at the MINERVA facility resulted in the pressure spike seen during 2017 mid-April. Alongside is plotted the month of 2018 March to show the shorter term stability after this was resolved. Note the pressure shown here is quantized because we are approaching the limit of our Granville Phillips 275 Convectron Gauge.

Temperature readings meanwhile, were recorded for MINERVA over the period of 2018 January through July (Figure 2.4a). These measurements were taken at the side of the cell holding the Echelle grating, and so it is most relevant for RV stability. Throughout that time period we manage to remain fairly stable from January to May, one such example being Figure 2.4b which depicts the stability over the month of March, with an RMS of 0.0052 K (two times better than our re-

(a)   **(b)**
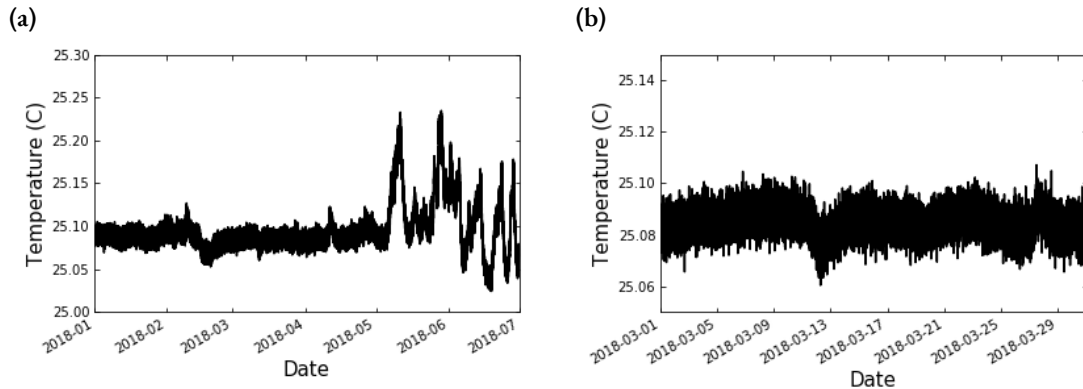
Figure 2.4: Temperature reading taken at the echelle side location on MINERVA. Measurements were taken from 2018 January through July, with small fluctuations occurring from May onward. We also plot 2018 March to more directly show the stability during a typical month of operation.

quirement of 0.01 K). Slightly larger fluctuations were seen to occur from May onward, where we removed and reinstalled the outer thermal enclosure for maintenance.

Moving forward, we intend to investigate the causes of some of the more minor fluctuations present in the environmental data. These could be a result of events such as the backlight being turned on and off, moving of the iodine stage in and out (which holds the cell which must be heated to 55 °C), fluctuations of the room HVAC, or other events related to the operation of MINERVA itself.

The scatter in the empirically determined wavelength solution of a single chunk for all our targets on sky (0.003 Å, or about 0.1 pixels, for the zero-point and 0.07% for the dispersion) dominates any trends seen on nightly or monthly timescales.

2.4   Telescope Control Software

2.4.1   Architecture

In Swift et al. (2015), we described robotic control software based on the Robo-AO control software written in C (Riddle et al., 2012). In the following years, we determined that the growing popularity of Python, the many easily importable libraries, and vendor-provided APIs made it an attractive alternative to write and maintain the code while simultaneously allowing more complex

features and capabilities. Our entire operational code base, written in Python, is hosted on Github[†].

A computer called "main" runs a 64 bit Ubuntu operating system and is responsible for most of the high-level operations. On startup, it begins three continuous functions. First, it operates an NTP server to which all other MINERVA clocks sync. It syncs itself to one of several stratum 2 time servers in the Western United States. Second, it runs a watchdog routine to monitor the temperature of the spectrograph in many locations and alert us via email if any are out of their operating range. Third, it runs a "domeControl" daemon that monitors the weather from several local weather stations: one at the MEarth building about 300 m away (Irwin et al., 2009), one at the HAT building about 230 m away (Bakos et al., 2002), one at the FLWO 1.2 m robotic telescope (home of KeplerCam) about 60 m away (Szentgyorgyi et al., 2005), and one we installed at the MINERVA building. It automatically evaluates if it is safe to open the domes based on cloud coverage, rain, humidity, wind speed, and Sun altitude, allowing overrides to open during cloudy weather or during the day for engineering. If it has been below freezing and wet (i.e., a potential for ice or snow), it sends us an email notifying us that manual approval is required to open the domes. Snow or ice on the roof can fall on the telescopes or overload the motors that open the shutters, which can prevent further robotic or remote control. Snow at the base of the enclosure can prevent it from fully opening. It must either melt or be cleared by the local site staff before we can safely open.

All automated safety checks must pass for 30 consecutive minutes and it must be requested to open before it will actually open. Once the enclosures are open, the criteria for closing are somewhat looser. These two requirements prevent rapid cycling of the enclosure during marginal conditions.

The domeControl daemon runs through its safety checks, sends a "heartbeat," and updates a status file every 15 s. The heartbeat is a firmware-level safety feature that protects us against a variety of potential failures. If a minute has elapsed and the enclosure has not received a heartbeat, it will automatically close, independent of any other activities. Should a failure of some kind prevent the enclosure from closing, emergency text messages are sent to several people to investigate immediately.

Finally, the "main" machine orchestrates the observations, which start each night at 4 pm local

---

[†] https://github.com/MinervaCollaboration

time via cron job, which we will describe in detail later in the next subsection.

Each of the four telescopes is controlled by its own computer running a 64 bit Windows 7 Professional operating system. Windows is required to run MaximDL for camera control and the PlaneWave Interface (PWI) software for telescope control. MaximDL controls our Andor and Apogee imagers and filter wheels for photometry (see Swift et al., 2015), as well as our ZWO imagers (see §2.2.1). We wrote our own server that runs locally on each Windows machine and can relay commands from our main control computer on the network to MaximDL. All images are saved to their own control computer on a drive that is cross mounted on the main computer. This allows us to run more complex image analysis like Source Extractor (Bertin & Arnouts, 1996) and astrometry.net (Lang et al., 2010) to perform automated world coordinate solutions for acquisition and guiding or automatic exposure time adjustment during sky flats.

PWI hosts its own server that can be controlled by any computer on the network through simple XML commands. PlaneWave provided several example functions in Python, which we integrated into our software. Each windows computer has "scheduled tasks" (the Windows equivalent to a cron job) that reboot the computers daily and start the servers.

The spectrograph is controlled by two additional Windows 7 computers provided with the KiwiSpec spectrograph from KiwiStar Optics (a business unit of Callaghan Innovations). One computer is dedicated to the thermal control servo that maintains the spectrograph temperature and runs independently of all others.

The other computer operates much like the telescope control computers, and runs our server to relay commands from the main computer to the hardware connected directly to the spectrograph control computer. While KiwiStar Optics provided software to control the spectrograph manually, there was no API to interact with it robotically. We wrote our own spectrograph control software to enable robotic operations. This computer is responsible for operating the iodine stage, iodine heater, the spectrograph detector, the backlight, the flat field lamp, the exposure meter, and the vacuum pump and valves. The server also doubles as a watchdog that emails us if the vacuum pressure goes out of its operating range.

2.4.2 OPERATIONS

The observations begin at 4 pm local time. Our software computes the time it takes for a standard suite of biases, darks and flats for the spectrograph necessary for calibrating our RV observations. If photometric observations are desired, we upload a schedule file that contains the observations and corresponding calibrations. At 4 pm, the software computes how long the requested photometric calibrations will take, then begins the calibrations so they will finish 10 minutes before sunset.

Under normal spectroscopic observations, a dispatch scheduler reads active targets tabulated in a Google spreadsheet, and computes a score for each target based on the current time, the target's visibility, when it was last observed, how many times it has been observed that night, and how many times we would like it to be observed each night. In addition, it computes a weight for a single B-star observation that grows throughout the night until it is observed to ensure we obtain one B-star observation per night for calibrations.

When photometric observations are requested for any subset of telescopes, we schedule our RV observations around the allocated times for the allocated telescopes. When only a subset of telescopes are scheduled for photometric observations, the others continue obtaining RV observations. Each telescope within the subset is capable of observing a distinct photometric target while the other telescopes obtain RVs on a single target.

During a typical spectroscopic observation, with all telescopes that are in RV mode, we slew to the target, turn on the backlight inside the spectrograph to illuminate the fibers, and expose the FAU camera. This provides us with the precise pixel location of the fiber on the acquisition camera. Next, we do a fine acquisition to put the star onto the fiber. Because our targets are so bright, it is a safe assumption to move the brightest star in the field to the position of the fiber. Then we perform an autofocus and begin guiding to keep the star onto the fiber. While we use an Alt/Az telescope, we do not correct for field rotation, opting to keep the target star on the fiber and letting all other stars rotate about it to minimize the change in the pupil illumination during the exposure.

During a typical photometric observation, we can either cycle through a list of filters throughout some observing window (e.g., a predicted transit window), observe continuously in one filter,

or take some number of exposures in each of several filters. While we have an off-axis guider for the imager, MaximDL does not allow us to control three cameras simultaneously, nor does it provide an API to switch between them robotically. However, the tracking performance of the CDK700s is superb and the direct drive motors have no periodic error, allowing us to take 5 minutes exposures unguided without any measurable trailing. Therefore, instead of the off-axis guider, we use the previous science image to correct for any long-term drift in tracking. This also has the advantage of not being subject to flexure or differential field rotation between the off-axis guider and the science camera, allowing us to easily maintain sub-pixel guiding accuracy throughout an hours-long transit—a capability that is critical to obtaining precise differential photometry.

We observe either RV targets or photometric targets throughout the night as desired, all the while monitoring the status of the dome and pausing if it closes. At the end of the night, we perform another set of calibrations, and close the dome. The data are backed up to our local RAID6 NAS (which can suffer two simultaneous drive failures without data loss), and our spectroscopic reduction pipeline is initiated at 10 am local time.

2.5   Spectroscopic Data Reduction

The first step in our spectroscopic data reduction is to calibrate the science exposures of our spectrograph's CCD. We collect and median stack eleven frames each night for the bias, dark current, and slit flats. For each science exposure, we subtract the overscan from the raw exposure. We experimented with dark current subtraction but omit this in our present pipeline because the corrections are negligible and it only serves to increase the noise. We re-normalize each bias-corrected exposure by the stacked slit flats, similar to the procedure developed in Bernstein et al. (2015), although we retain the blaze function. Finally, we interpolate between fiber bundles to estimate and subtract scattered light.

With our calibrated science frames, we are prepared to extract the one-dimensional spectrum from the two-dimensional CCD exposure. We wrote a custom pipeline using the optimal extraction algorithm (Horne, 1986; Piskunov & Valenti, 2002; Zechmeister et al., 2014; Bernstein et al., 2015).

Optimal extraction requires that flux is a separable function of x and y so that $F(x, y) = F(x)F(y)$, a condition that is very nearly satisfied in our instrument. This allows us to independently find the observed flux in each row, x, through

$$F(y) = \boldsymbol{p}(x, y)F(x) + n(y). \tag{2.1}$$

Here $F(x)$ is the underlying spectrum we wish to extract. We determine this from the observed flux in the cross-dispersion direction, $F(y)$, a model for the noise $n(y)$, and a normalized cross-dispersion profile, $\boldsymbol{p}(x, y)$.

Our pipeline presently uses a modified Gaussian for $\boldsymbol{p}(x, y)$. This gives us the form

$$\boldsymbol{p}(x, y) = N(x)\, e^{\left(-0.5\left(\frac{|y - y_c(x)|}{\sigma(x)}\right)^{p(x)}\right)}. \tag{2.2}$$

The free exponent $p(x)$ is slightly broader than a typical Gaussian with $p \approx 2.2$. The value $N(x)$ is a numerically determined normalization coefficient and $y_c(x)$ indicates the trace centroid, determined during calibration from archival fiber flats. We model $\sigma(x)$ and $p(x)$ as slowly varying polynomials along the dispersion direction

We simultaneously extract all fibers within each column, accounting for any cross-talk. During extraction, we include a slowly varying background term to account for any additional scattered light. We also apply a cosmic ray rejection algorithm and mask any hits. Although our precise wavelength solution $\lambda(x)$ is found with the Doppler pipeline, we generate an initial solution from archived thorium argon exposures we took during the installation and maintenance of the spectrograph. This allows the subsequent code to quickly lock on to the correct solution.

The spectra from individual telescopes are extracted and modeled independently all the way through to the orbital modeling. This gives us four data points per exposure and a unique insight into systematic errors having to do with the telescope and the position of the trace on the detector (cosmic rays, scattered light, and flat-fielding).

2.6 Doppler Pipeline

The one-dimensional spectrum is the primary input for our Doppler code[‡]. The architecture and general principles of our Doppler code are inspired by the code that is comprehensively described by Wang (2016), although the algorithm is originally introduced by Butler et al. (1996). Our code implements a forward modeling procedure on this spectrum that can be summarized mathematically as

$$F_{obs}(x) = [F_{I_2}(\lambda(x)) \times F_{\star}(\lambda'(x))] * \text{IP}(x), \qquad (2.3)$$

where x is the pixel position in the dispersion direction, $\lambda(x)$ is the wavelength solution, $\lambda'(x)$ is the Doppler-shifted wavelength solution, F_{obs} is the one-dimensional spectrum extracted from our observations, F_{I_2} is the normalized absorption spectrum of our iodine cell, $F_{\star}$ is the stellar flux, and $\text{IP}(x)$ is a model of the spectrograph's intrinsic instrumental profile (which is sometimes referred to as the spectrograph response function or the one-dimensional spectral point spread function). After determining the product of the iodine absorption spectrum and stellar spectrum, the observed spectrum is modeled as this product convolved with the instrumental profile.

2.6.1 Iodine Absorption Spectrum

We obtain F_{I_2} from a high resolution Fourier Transform Spectrometer (FTS) scan of the gaseous iodine cell as it is illuminated by a high signal-to-noise-ratio (S/N) continuum light source. We have two FTS scans of the MINERVA iodine cell. The first one was obtained at the Pacific Northwest National Laboratory a few years ago together with the CHIRON iodine cell (Tokovinin et al., 2013). The second FTS scan was done by Dr. Gillian Nave's group at NIST (e.g., see Nave, 2011; Crause et al., 2018). Both scans were taken with the iodine cell at its operating temperature specification of 55 °C. Unfortunately, the two scans disagree in terms of line depths and line depth ratios, and we are further investigating the origin of this discrepancy. For concreteness, the results shown here use the second FTS scan, though both produce similar results.

The FTS scan is sufficient for determining our fiducial wavelength solution $\lambda(x)$ because the

---

[‡] https://github.com/MinervaCollaboration/minerva-pipeline

resolving power of the FTS ($R \approx 300,000$) is about a factor of 4 greater than that of our KiwiSpec spectrograph ($R \approx 80,000$). Because the molecular iodine lines span from 500 to 630 nm, the wavelength solution is determined solely within this range.

2.6.2 CHOICE OF IP(x)

In our Doppler code, we choose between two functional forms for our model (IP(x)) of the spectrograph's instrumental profile. One form is a time-invariant spline function that is introduced in §2.6.5 and the other is a time-varying summation of satellite Gaussian profiles stacked on one central Gaussian profile that is described in §2.6.7. When using the former, we characterize our instrumental profile by using observations of a continuum light source with a high S/N while it illuminates the iodine gas cell in our KiwiSpec spectrograph. For reasons discussed later, we use the scattered sunlight of the daytime sky as our light source. For the Gaussian-like IP(x), however, we characterize the instrumental profile simultaneously with each stellar spectrum during our forward modeling. As a precaution, we also observe a B-type star each night (with iodine cell in place) to allow a more precise characterization of our instrumental profile as it changes over long periods of time.

2.6.3 REFERENCE STELLAR SPECTRUM

A reference stellar spectrum is needed to determine the magnitude of the Doppler-shift seen when observing the science target. We use reference stellar spectra previously constructed by the CPS group using Keck/HIRES. They find the references by observing the science target without contamination from the iodine gas absorption lines. In this case, the IP(x) can be deconvolved with this observed (iodine-free) spectrum to get a reference stellar spectrum. In other words, $F_\star(\lambda_{\mathrm{ref}}(x))$ is solved for via $F_{\mathrm{obs,ref}}(x) = F_\star(\lambda_{\mathrm{ref}}(x)) * \mathrm{IP}(x)$. This IP($x$) and $\lambda_{\mathrm{ref}}(x)$ here however are found using observations taken immediately before and after the iodine-free observation. The iodine-free observation of the science target is bracketed by iodine-calibrated observations of a nearby B-type star. The bracketed observations are particularly helpful if the instrumental profile is known to fluctuate on very short timescales, which is true in the case of Keck/HIRES. An IP(x) and $\lambda_{\mathrm{ref}}(x)$ is evaluated for each iodine-calibrated B-type star observation and subsequently averaged. The resul-

tant $IP(x)$ is then deconvolved with the spectrum from the iodine-free science-target observation $F_{obs,ref}(x)$ to get $F_\star(\lambda_{ref}(x))$, whose wavelength solution is assumed to be the averaged $\lambda_{ref}(x)$. The aforementioned CPS group refers to the reference stellar spectrum as the Deconvolved Stellar Spectral Template (DSST).

Using these DSSTs may limit our ability to accurately model $F_{obs}(x)$ because the two spectrographs may suffer from different systematics. Furthermore, the observatory locations (Hawaii and Arizona in the U.S.) have significantly different water columns, dramatically changing the telluric features in our spectra. These differences may be a source of systematic error in our forward modeling procedure via the DSSTs. We will investigate the extent of these errors in the future. Meanwhile, we find that the DSSTs are sufficient for the first RV results of our RV survey. We have yet to derive our own reference stellar spectra because their development requires a substantial amount of observing time for each of our targets. The DSSTs are derived from observations with a higher S/N, and Keck's large aperture allows it to obtain such high S/N observations in a shorter time compared to MINERVA, which minimizes complications due to barycentric motion. In addition, unlike our fiber size, Keck's slit width is adjustable, allowing higher resolution templates which is helpful in developing the template.

2.6.4 DOPPLER-SHIFTED WAVELENGTH SOLUTION

The forward modeling procedure finds the best fit to $F_{obs}(x)$ in Equation 4.3. Our Doppler code uses a least-squares algorithm to evaluate the best fit parameters. One of the parameters is the Doppler shift of the stellar spectrum $F_\star(\lambda'(x))$. The Doppler-shifted wavelength solution can be decomposed as $\lambda' = \lambda_{ref} \cdot (1 + z)$, where z is the Doppler shift from the radial velocity of the star and the motion of the telescope with respect to the star. This relative motion of the telescope is our barycentric velocity and it is dominated primarily by the Earth's rotation (~ 0.5 km s^{-1}) and orbital motion around the Sun (~ 30 km s^{-1}). The methods introduced in Wright & Eastman (2014) are used in our Doppler pipeline to correct for the telescope's barycentric velocity and subsequently determine the radial velocity of the star – which may or may not contain information about a planetary companion.
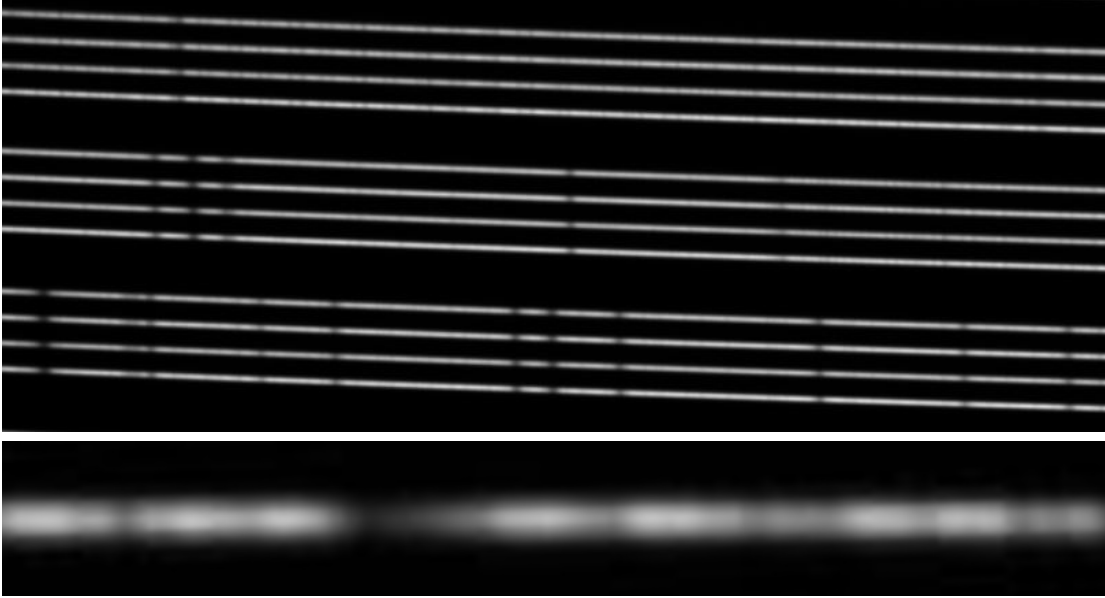
Figure 2.5: Top: snippet of MINERVA's two-dimensional echellogram. Each order contains 4 traces. Each trace belongs to each telescope. The full width of a frame is 2048 pixels. Bottom: a close-up of one chunk of one trace in one order is shown. A chunk spans 128 pixels in the dispersion direction and ∼10 pixels in the cross-dispersion direction. The 128 pixels translates to ∼2 Åfor our KiwiSpec spectrograph. Each column of the chunk is treated as an independent crosscut of data. The dark regions along this chunk indicate the presence of absorption features.

2.6.5 Fixed IP and IP Stability

Our optical system can be divided into three general components: the telescope, the optical fibers, and the spectrograph. As the stellar rays trace this path, the optics distort the star's image. To determine the radial velocities from our observed spectra, we must know the manner of distortion that occurred en route to the spectrograph's CCD. The $\text{IP}(x)$ is the shape a delta function would have when distorted by the entire optical system. The convention for determining an $\text{IP}(x)$ is to assume it follows some function comprised of Gaussian structures that extend in the dispersion direction. This section describes how we have taken a unique approach.

In developing our new $\text{IP}(x)$, we do not use a B-type star nor do we use calibration lamps. Instead, we take spectra of the sky during the daytime. Unlike our nightly stellar spectra, these daytime sky spectra yield a S/N/pixel > 150. With our stable spectrograph, the $\text{IP}(x)$ characterized from daytime sky spectra should not change by the time we take stellar spectra at night. While the daytime sky is uniformly illuminated and may mask IP variations due to imperfect scrambling, such

spectra give us a starting point to evaluate IP variations due to changes beyond the fiber.

The daytime sky spectra have proven to be a reliable source of data for determining the time scales at which our instrumental profile is stable. To find this time scale, we create an IP(x) that is time-invariant, which we refer to as the "fixed IP." By deducing the instrumental profile in these spectra, we can determine when and why it evolves.

We use the profile in the cross-dispersion direction to model the instrumental profile's shape in the dispersion direction. While the circular fiber makes this approximately correct, the distortions caused by the spectrograph's optical design certainly invalidate this assumption in detail. However, we can still evaluate the stability of the IP regardless, and we suspected that as long as the IP was stable and systematically wrong the same way each time, it would not impact the RV precision. Indeed, the results of long-term stability described later in this section justify this assumption.

The two-dimensional echellogram from MINERVA has four traces per order as shown in Figure 2.5. There is a trace for each telescope, and we divide each of the 18 orders into 15 "chunks." Each chunk consists of 128 columns of the trace. The total number of chunks in a frame is the number of chunks per order times the number of telescopes times the number of orders in the frame—1080. We define a distinct IP(x) for each of these chunks because the length of each chunk acts as a characteristic length scale for which the intrinsic instrumental profile changes. For this reason, we apply Equation 4.3 only over 128 pixels in the dispersion direction. Thus in practice, our forward modeling procedure is repeated for each chunk.

To characterize the fixed IP, we first split a chunk (of two-dimensional daytime sky spectra) into 128 columns, or "crosscuts." As shown at the top of Figure 2.5, the traces are not perfectly horizontal. We therefore find the centroid of each crosscut and align the crosscuts' centroids so that the chunk is essentially as horizontal as the bottom of Figure 2.5. Ultimately, we want to normalize these crosscuts such that they collectively constrain the shape of our true instrumental profile. To align and normalize them, we start by assuming each crosscut can be modeled as a Gaussian,

$$G(x) = A \exp\left[-\left(\frac{x - x_0}{\sigma} \right)^2 \right] + b, \qquad (2.4)$$
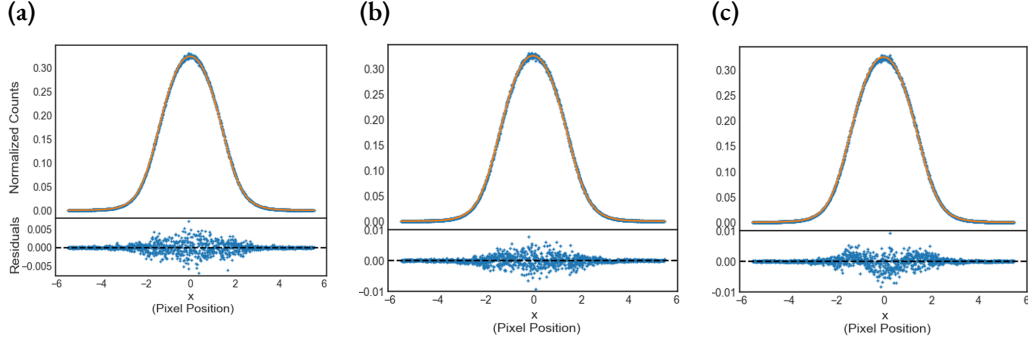
Figure 2.6: Orange lines represent the fixed IP we constructed from daytime sky spectra obtained on 2018 June 19. Blue points represent the normalized crosscuts from data obtained during one daytime sky exposure. The bottom plots show the residuals between the normalized crosscuts and the fixed IP. **(a)** The normalized crosscuts used to determine the fixed IP are introduced here. **(b)** The fixed IP is used to model data obtained on 2017 October 2. The same chunk from (a) is used here. **(c)** The fixed IP is used to model data obtained on 2017 April 3. The same chunk from (a) and (b) is used here.

where A is the amplitude, x is the pixel position in the cross-dispersion direction, x_0 is the centroid, σ is the width, and b is the background of the raw spectra. We use a least-squares optimizer that follows the Levenberg-Marquardt algorithm to find the best fit parameters. We then subtract b from the crosscut data and integrate over this background-subtracted crosscut. After dividing the background-subtracted crosscut by this integral we can obtain the normalized background-subtracted crosscut. In other words, $D_{\text{norm}}(x) = (D_{\text{raw}}(x) - b)/N$, where D_{norm} is the normalized background-subtracted crosscut, D_{raw} is the original crosscut, and N is the normalization factor calculated by the aforementioned integration.

Once $D_{\text{norm}}(x)$ is found for each of the 128 crosscuts, we fit a spline function of the third degree to all of them simultaneously. This cubic spline has breakpoints that are each separated by 6/10 of a pixel from each other. The spline acts as our preliminary fixed IP: $\text{IP}_f(x) = \text{spline}(D_{\text{norm}}(x))$. To find the optimal fixed IP, we perform an iterative process of modeling the $D_{\text{raw}}(x)$ and subsequently evaluating a new $D_{\text{norm}}(x)$ and $\text{IP}_f(x)$.

Instead of a Gaussian, we use the previous spline fit model during the iterative process:

$$M(x) = N \times \text{IP}_f(x - \Delta x) + b, \tag{2.5}$$

where $M(x)$ is the model for one crosscut and Δx is a translational shift parameter. Now, the least-squares optimizer has only three parameters to evaluate: Δx, N, and b. For the iterative process, we repeat the following procedure: find $D_{norm}(x)$ of each crosscut, define the $IP_f(x)$ for the chunk, optimize the 3 parameters of $M(x)$ for each crosscut, calculate the reduced χ^2 of all the crosscuts' data and $M(x)$ models collectively, and lastly evaluate the difference between the previous iteration's reduced χ^2 and the current iteration's reduced χ^2. The most important distinction between iterations is the differing fixed IPs; when the χ^2 gets lower, we conclude that the current iteration's $IP_f(x)$ is better at modeling the spectrograph's instrumental profile than the previous iteration's $IP_f(x)$. As the $IP_f(x)$ gets better with each iteration, the difference in reduced χ^2 values lessens. Once this difference is less than 10^{-4}, any changes made to the $IP_f(x)$ in the subsequent iterations are insignificant. The final iteration's $IP_f(x)$ then becomes our nominal fixed IP.

Figure 2.6a is an example of the final fixed IP. The blue data points represent the $D_{\mathrm{norm}}(x)$ for all crosscuts of the final iteration. The orange line is the final $IP_f(x)$. In this case, the data come from one chunk in one daytime sky exposure taken on 2018 June 19. The bottom plot illustrates the residuals, $D_{\mathrm{norm}}(x) - IP_f(x)$. The residuals are greatest near the center, where the shot noise is greatest, but they show no systematic structure. This suggests a good fit to the data.

TABLE 2.1
STARS OF INTEREST

HD	R.A. (J2000)	Decl. (J2000)	V	SpType
122064	13 57 32.059	+61 29 34.30	6.52	K4V
217014	22 57 27.980	+20 46 07.80	5.46	G5V

To test the longevity of our instrumental profile's stability for as long as possible, we construct the fixed IP with data taken at the time when we began this stability test and we used this fixed IP on spectra taken days, months, and a full year prior to the commencement of this test. We commenced this test after the end of our first full-season observing campaign (see §2.1). We then tested the fixed

IP on spectra taken as far back in time as we saw fit for this test. We fit the same fixed IP to daytime sky spectra taken on 2017 October 2—about nine months away from the construction of the fixed IP. The result is presented in Figure 2.6b and it has the same general pattern of noise in its residuals as Figure 2.6a. This implies that the instrumental profile has not changed within that time period. Note that for Figure 2.6b the 2018 fixed IP was used to model the 2017 spectra (via Eq. 2.5) and subsequently normalize its crosscuts.

To extend the timeline of this test further, we tried to use daytime sky spectra taken at the very beginning of that first observing campaign (2017 September 14). Unfortunately, our daytime sky spectra taken within those first two weeks, between September 14 and October 2 in 2017, were of poor quality and had a relatively low S/N until we resolved the issue. Therefore, we tried to use daytime sky spectra taken before the 2017 monsoon season and thus before our first full-season observing campaign. Fortunately for this test, we took many daytime sky spectra back in 2017 March and April. We therefore extend the timeline of this test to 2017 April.

Figure 2.6c shows how our 2018 fixed IP is used to model data taken on 2017 April 3. The residuals here show strong systematic structure when compared to Figures 2.6a and 2.6b. From these three examples, it is clear that our spectrograph's instrumental profile was stable from 2017 October 2 to 2018 June 19 but not from 2017 April 3 to October 2.

The spectrograph's instrumental profile evolved significantly within the window of six months between 2017 April 3 and October 2. As explained in §2.3 and shown in Figure 2.3a, during this time, the pressure rose dramatically for an extended period of time during the 2017 monsoon season after a brief power outage. This event permanently altered the spectrograph in such a way that the environment could not naturally return to its original instrumental profile when the pressure returned to its original operating specification. This means that the instrumental profile might have been stable for longer than nine months if the power outage and subsequent pressure instability did not occur. When characterizing the instrumental profile with a fixed IP, a new fixed IP must be used whenever an event such as this occurs. If this is not done, a situation like that of Figure 2.6c is likely to occur.
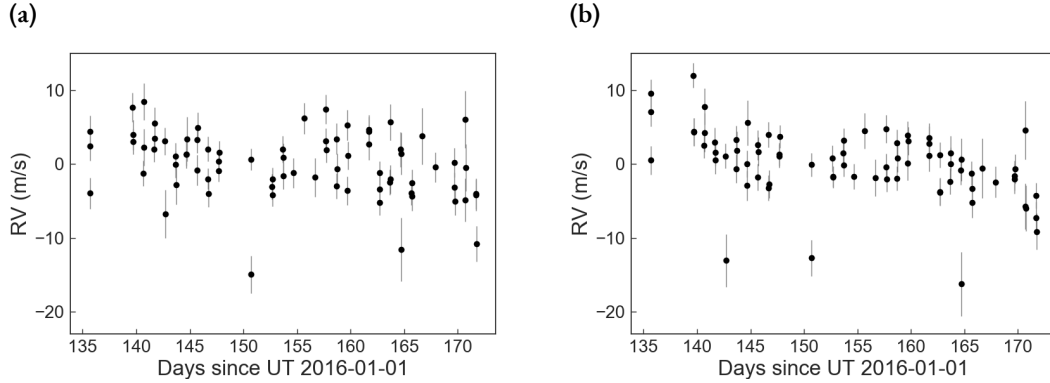
Figure 2.7: MINERVA radial velocities of HD 122064. **(a)** The fixed IP is used in our forward modeling procedure. **(b)** Here, the sum-of-Gaussians IP is used.

2.6.6 GAUSS-HERMITE IP

We explored the possibility of modeling a fixed component of the IP with a time-varying component to account for changes in the IP due to perturbations like that which is seen in Figure 2.6c and explained in Figure 2.3. We can formulate such an IP as

$$
\mathrm{IP}_{GH}(x) = \sum_n A_n \left(\frac{2}{\pi \sigma^2} \right)^{1/4} \frac{1}{\sqrt{n! 2^n}} H_n \left(\frac{x\sqrt{2}}{\sigma} \right) e^{-\left(\frac{x}{\sigma} \right)^2}
$$
$$
+ \ \mathrm{IP}_f(x).
$$

(2.6)

This function includes the sum of the products between Gaussians of amplitude A_n and Hermite polynomials H_n. The systematic structure seen in Figure 2.6c suggests that we may be able to model the time variable component of the IP with fewer free parameters than a purely time-variable IP, and thus preserve the signal in the spectrum to constrain the Doppler signal we care about rather than the instrumental profile. Unfortunately, the number of additional parameters required to accurately model the time-variable component was comparable to purely time-variable IP described in the following section, and therefore offers no advantage. Additionally, the GH parameterization of the IP is not as well behaved as the sum of Gaussians in our forward modeling procedure.

34

TABLE 2.2
HD 122064 RVs and RV Errors (m s^{-1})

| Date - 2,457,500 | IP$_f$ | | IP$_G$ | |
(BJD$_{\text{TDB}}$)	RV	Error	RV	Error
24.672037	-3.95	2.09	0.51	1.92
24.693414	2.47	2.03	7.07	1.99
24.714667	4.41	2.12	9.56	1.90
28.674272	7.66	1.97	12.03	1.70
...	...	...	...	...

NOTE.—RVs for HD 122064 displayed in Figure 2.7. The mean error is 2.1 m/s for each data set: the data derived from the fixed IP and data from the sum-of-Gaussians IP. A portion is shown here for guidance regarding its form and content.

2.6.7   Sum-of-Gaussians IP

Our sum-of-Gaussians IP,

$$\text{IP}_G(x) = \sum_n A_n \exp\left[-\left(\frac{x - x_{0,n}}{\sigma_n} \right)^2 \right], \tag{2.7}$$

is a time-dependent IP that is described in detail by Valenti et al. (1995). Notice here that we do not include the fixed IP. Also note that A_0 is fixed to 1 so that there is one large central Gaussian while all other Gaussian components act as small satellite Gaussians. To test this IP$_G$ against the fixed IP, we calculated RVs for an RV standard star and a planet-hosting star after forward modeling the data with each of the IPs, as described later in §2.7.

2.7   RV Performance

The radial velocity we measure is the reflex motion of the star induced by the gravitational pull of its planetary companion. This motion is accounted for in Kepler's laws. Kepler's laws suggest that the

(a)

(b)
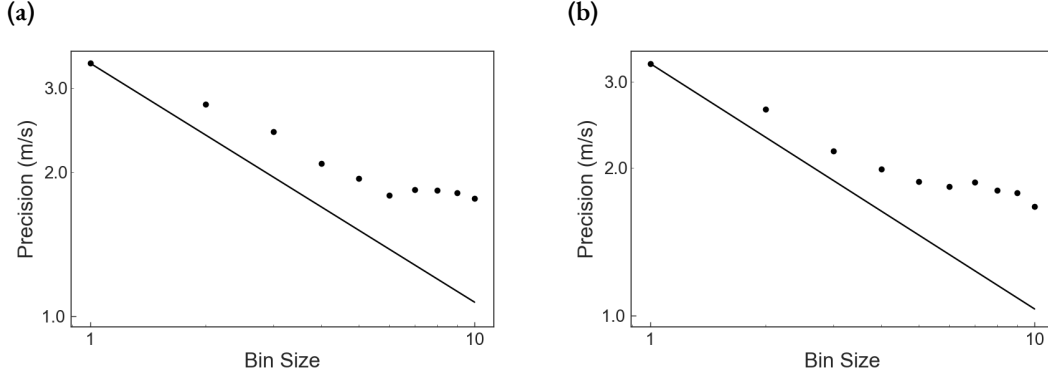
Figure 2.8: The solid line represents the precision if the binned data set only consisted of white noise. The points represent our precision at a given binning. Beyond a binning of roughly six, the precision significantly deviates from the solid line, the precision barely improves, and systematic errors dominate the data. This is the case for both the fixed IP and sum-of-Gaussians approach. **(a)** Allan variance for data in Figure 2.7a produced with the fixed IP. When binning by six, we see a precision of 1.78 m s^{-1}. **(b)** Allan variance for data in Figure 2.7b produced with the sum-of-Gaussians IP. When binning by six, we see a precision of 1.87 m s^{-1}.

lower limit of the planetary mass can be described as

$$M_p \sin i \approx K\sqrt{1 - e^2}\left(\frac{PM_*^2}{2\pi G}\right)^{1/3} \tag{2.8}$$

(see parameter symbols with Table 2.9 descriptions). To model the stellar system, we use EXO-FASTv2 (Eastman et al., 2013; Eastman, 2017).

Before the minimum mass is determined, the RV semi-amplitude must be extracted from the Doppler-shifted spectra via a forward modeling procedure. The results of the instrumental profile work discussed in §2.6.5 provided fruitful information that paved the way for the successful extraction of MINERVA's first radial velocity results.

We present RV measurements of two target stars to demonstrate MINERVA's precision. These stars are HD 122064 and HD 217014 (51 Peg), which have their coordinates, V magnitude, and spectral type reported in Table 2.1. HD 122064 is chromospherically inactive, has no known companions, and serves as a convenient RV standard star. For the hot Jupiter 51 Peg b, we compare the planetary properties derived from MINERVA data with results from the literature.

2.7.1 HD 122064

With one telescope, we acquired the radial velocities of HD 122064 during the months of 2016 May and June. As a test, we used both the fixed IP and the sum-of-Gaussians IP in our forward modeling to generate two distinct RV data sets which derive from the same spectra.

For the purposes of the instrumental profile's stability test, we only used one daytime sky exposure to construct the fixed IP. Whenever we perform our forward modeling procedure with the fixed IP, we make the fixed IP more robust by using multiple daytime sky exposures. We perform the same procedure as described in §2.6.5, except the number of crosscuts that we simultaneously fit a cubic spline function to is equal to 128 times the number of daytime sky exposures we use. Each set of 128 crosscuts comes from the same chunk of distinct daytime sky exposures. For the May/June data set, we use ∼5 daytime sky exposures to construct a fixed IP for each chunk and these exposures are somewhat evenly distributed throughout the 1.5 months timescale of the data set. This fixed IP is used to generate the RVs in Figure 2.7a while the sum-of-Gaussians IP is used to produce the RVs of Figure 2.7b.

After the RVs are extracted, we compute the Allan variance to determine the level of precision MINERVA can achieve. In Figure 2.8, the line represents the precision if the binned data only contained white noise. We use an error-weighted, overlapping Allan variance to determine the limit for which we can bin down the given data set before it is dominated by systematic errors (Allan, 1966; Malkin, 2011).

We have seventy-five radial velocity measurements tabulated in Table 2.2 and shown in Figures 2.7a and 2.7b. Figures 2.8a and 2.8b suggest that a bin size of six roughly marks the limit for which the respective binned data sets begin to deviate from white noise. At this binning, we are sensitive to variations below the 2 m s^{-1} level for our measurements of this RV standard star. The precision achieved is 1.8 m s^{-1} for the fixed IP approach and 1.9 m s^{-1} for the sum-of-Gaussians approach. This could potentially change depending on the standard star or the amount of data we have for a given star. To confirm this, we plan on performing the same test for observations of other RV standard stars. Regardless however, these RVs evaluated through our Doppler pipeline suggest

that our fixed IP is doing just as well as our sum-of-Gaussians IP.

2.7.2   HD 217014

MINERVA observations of 51 Peg were taken with one telescope in 2017 October. Again, we use the fixed IP and sum-of-Gaussians IP to extract the radial velocities. It is wise to see if our radial velocities can confirm the existence and characteristics of exoplanet systems. 51 Peg b is the first of such exoplanets to be tested. We use EXOFASTv2 to constrain the properties of this exoplanet system. Our stellar parameters are informed by the broad band photometry summarized in Table 2.3. The RVs and resultant 51 Peg b properties derived with both IPs are so similar that we only show the results produced with the fixed IP. The unbinned RVs and the EXOFASTv2-generated orbital solution are illustrated in Figure 2.9a, tabulated in Table 2.4, and summarized in Table 2.9. Figure 2.9b shows the same but with the time series folded to the phase of the planet's orbital period.
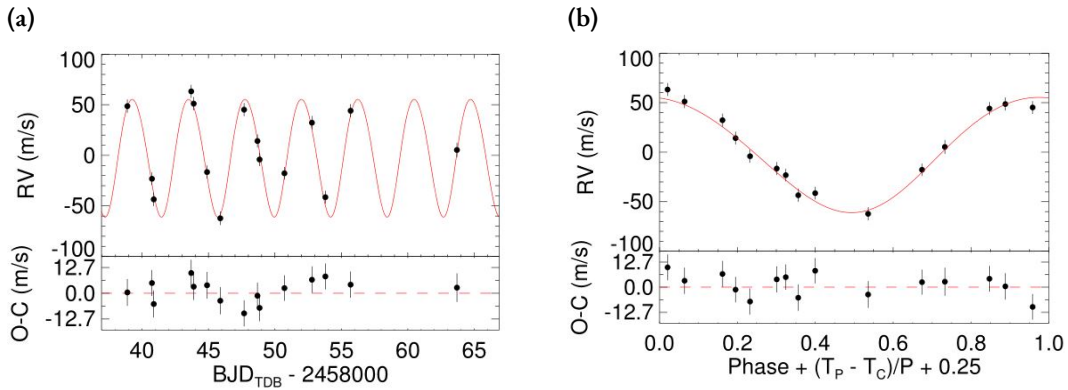
Figure 2.9: Radial velocities of 51 Peg obtained with MINERVA. The residuals are plotted below. The error bars listed in Table 2.4 are inflated here via the fitted jitter. The solid line is the best-fit orbital solution derived from EXOFASTv2. The data span across 2017 October. **(a)** Radial velocity time series for 51 Peg. Note that BJD_{TDB} means Barycentric Julian Date in Barycentric Dynamical Time (for elaboration see Eastman et al., 2010). **(b)** The same radial velocities are phase-folded to the planet's orbital period.
(A color version of this figure is available in the online journal.)

The median and 68% confidence intervals determined using EXOFASTv2 with the MINERVA data for all parameters of the 51 Peg system are listed in Table 2.9. We only employ constraints on three of the stellar parameters. We impose a prior on the stellar metallicity ([Fe/H]) of 0.20 ± 0.07 dex from spectroscopy described in Fuhrmann et al. (1997). We set the V-band extinction's (A_V)

upper limit to 0.11811 magnitudes, using the dust maps from Schlafly & Finkbeiner (2011). Lastly, we impose a Gaussian prior on the parallax (π) of 64.65 ± 0.12 mas from Gaia Collaboration et al. (2016, 2018). These priors, coupled with a MIST stellar evolution model (Choi et al., 2016; Dotter, 2016) and an SED model, constrain the properties of the host star.

TABLE 2.3
51 Peg Magnitudes

Band	Mag.	Used Mag. Error	Catalog's Mag. Error
Tycho-2 Catalog		(Høg et al., 2000)	
BT	6.249	0.020	0.014
VT	5.526	0.020	0.009
2MASS Catalog		(Cutri et al., 2003)	
J2M	4.655	0.300	0.300
H2M	4.234	0.270	0.270
K2M	3.911	0.020	0.020
WISE Catalog		(Wright et al., 2010)	
WISE1	3.909	0.387	0.387
WISE2	3.624	0.246	0.246
WISE3	3.929	0.030	0.016
WISE4	3.904	0.100	0.024

We compare our results with the values in Butler et al. (2006) (hereafter referred to as Bu06). They cite the SPOCS catalog (Valenti & Fischer, 2005) as the source for most of their stellar parameters. The Bu06 distance d to the star and its uncertainty are from the *Hipparcos*[§] catalog. Valenti & Fischer (2005) suggest that the typical uncertainties for their stellar parameters amongst their catalog of stars are 0.06 dex for $\log g$, 44 K for T_{eff}, and 0.03 dex for [Fe/H]. Bu06 assumes a 10% uncertainty for the stellar mass M_*. Bu06 does not report a value for stellar radius R_*. We therefore calculate this using their stated $\log g$ and M_* values. The uncertainty in the stellar radius is found using propagation of error between those two parameters.

The reference planetary and telescope parameters shown in Table 2.9 were derived solely from Bu06. Their observations were taken at Lick Observatory using the Hamilton spectrograph (Vogt, 1987), the 3.9 m Anglo-Australian Telescope using UCLES (Diego et al., 1990), and the Keck Observatory using HIRES (Vogt et al., 1994). Their quoted RV jitter σ_J, however, does not come from

---

[§]Vizier Online Data Catalog, I/239 (ESA 1997)

their observations. Their jitter comes from the model developed by Wright (2005), which was informed by a sample of 531 stars observed at Keck that had known activity levels, colors, and parallaxes. In general, the jitter depends on the spectral type of the star and the instrument observing it. The model by Wright (2005) uses a stellar activity indicator, $B - V$ color, and difference in magnitude above the main sequence to approximate the stellar jitter.

TABLE 2.4
RV RESULTS FOR 51 PEG

Date - 2,458,000 (BJD$_{\text{TDB}}$)	RV (m s^{-1})	Error (m s^{-1})	Residuals (m s^{-1})
38.897636	42.28	3.11	0.41
40.748225	-29.54	2.60	5.05
40.883873	-49.87	3.19	-5.30
43.703150	56.90	2.81	9.99
43.888337	44.76	3.13	3.24
44.892530	-22.88	2.99	3.94
45.888237	-68.62	3.27	-3.70
47.681088	38.81	2.72	-9.92
48.686860	7.81	2.70	-1.24
48.844736	-10.45	3.04	-7.23
50.718624	-24.11	2.30	2.54
52.787278	25.94	3.05	6.67
53.797358	-47.75	2.59	8.28
55.696227	37.76	2.81	4.24
63.696364	-1.04	3.99	2.76

NOTE.—The mean formal error derived from the third column is 3.0 m s^{-1}. The fourth column represents the residuals between the RV data (of the second column) and the best-fit orbital solution from EXOFASTv2. The RMS of the residuals is 5.6 m s^{-1}, and the systematic error floor, achieved when binning by 2, is 4.2 m s^{-1}.

Values not reported by Bu06 are marked with ellipses (...) in Table 2.9. For the parameters that have a value and errors reported by Bu06, we state the discrepancy between our values and theirs in

terms of 1σ uncertainty. We define this discrepancy as

$$\Delta\sigma = \frac{N_1 - N_2}{\sqrt{(\sigma_{1,L})^2 + (\sigma_{2,U})^2}}, \text{ when } N_1 > N_2, \tag{2.9}$$

in which $\sigma_{1,L}$ is the lower error bar for N_1 and $\sigma_{2,U}$ is the upper error bar for N_2. Ideally, the discrepancy should be less than 1σ. Seeing as the discrepancies evaluated for the tabulated parameters—most importantly the planetary parameters—are $\lesssim 1.0\sigma$, we find good agreement with results quoted in literature.
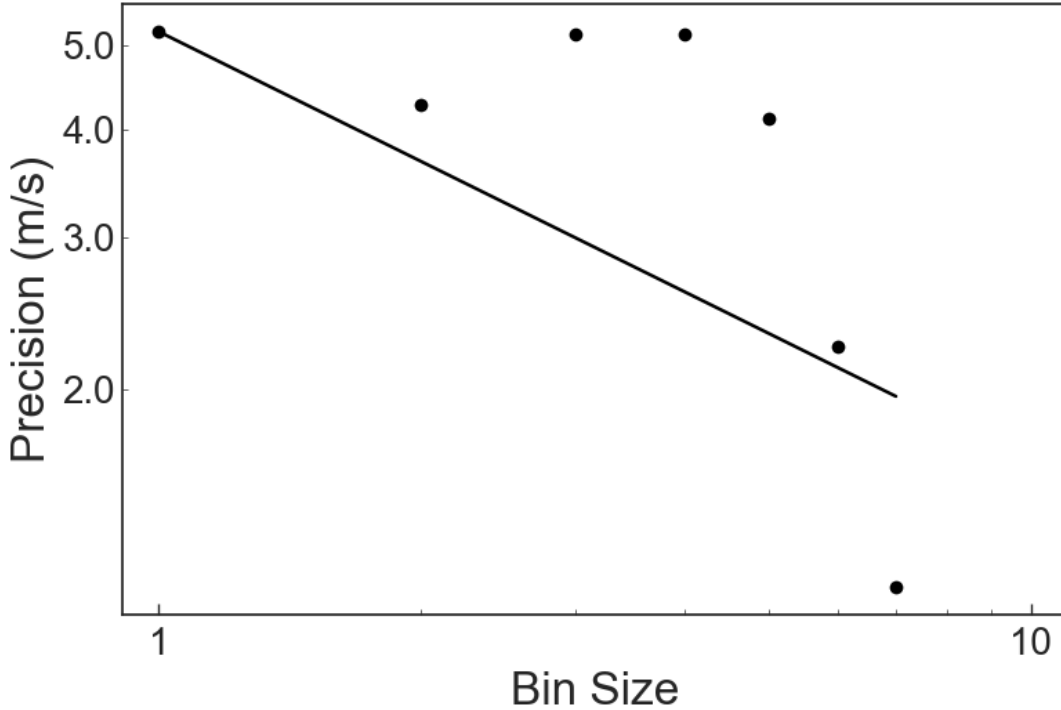
Figure 2.10: Allan variance from the 51 Peg model residuals listed in Table 2.4. The precision for the RV standard star (HD 122064) is notably better than the precision exhibited here for 51 Peg. The additional RV scatter is most likely due to the greater stellar jitter and substantially smaller sample size of this data set.

We also analyze the residuals of the fit to 51 Peg b to determine our precision. An Allan variance plot of the residuals is shown in Figure 2.10, demonstrating our per point scatter (5.6 m s^{-1}) and systematic floor (4.2 m s^{-1}) when two observations are binned is considerably worse than achieved for HD 122064, most likely due to stellar jitter of the more active host star. We note that fitting for the period and eccentricity may absorb some of the excess scatter and make our precision appear

better than it is. To address this, we also ran a fit fixing the period to the B06 value (4.230785 days) and fixing the eccentricity to zero, but found an insignificant increase in the per-point residual RMS (5.6 to 6.0 m s^{-1}) and an insignificant decrease in the binned-by-2 residual RMS (4.3 to 4.2 m s^{-1}). Therefore, we conclude that fitting the period and eccentricity does not have a major impact on our inferred precision.

2.8   FUTURE WORK

While we are about a factor of 2 of our original goal and already operating with an unmatched combination of cadence and precision that enables us to detect new planets and provide valuable insight into stellar jitter, there are several areas for improvement that may help us achieve our original goal of 80 cm s^{-1}.

The relatively long exposures we typically take increases the uncertainty in the flux-weighted midpoint time and therefore introduces additional error in the corresponding barycentric correction (Wright & Eastman, 2014). Either shortening our exposures or improving the determination of the flux-weighted midpoint may improve our ultimate RV precision.

The stability of our spectrograph demonstrated here allows us several avenues to improve our Doppler pipeline. The templates we use, derived from Keck/HIRES observations, is likely to contain systematic differences due to the instrument and atmospheric conditions (e.g., increased water column) from our instrument, and may be dominating our RV error. We will investigate generating our own templates, but we will also investigate fitting for the template from dozens of spectra, known as the "grand solution" (Gao et al., 2016; Czekala, 2017). Further, modeling many spectra at once with the same instrumental profile and/or fitting for the iodine cell removes many sources of potential systematic error and unnecessary nuisance parameters that may be covariant with the radial velocity.

While we have octagonal fibers coupled to a circular fiber for optimal near-field scrambling, we have opted not to introduce a double scrambler to improve our far field scrambling, which typically reduces the throughput by 10-20% (Halverson et al., 2015). We may revisit this trade-off in the

43

future, as well as explore the possibility of introducing an agitator to improve modal noise. We are also actively exploring the improvement achievable by using spectro-perfectionism to improve the extraction of our 1D spectra using a 2D instrumental profile (Bolton & Schlegel, 2010).

Finally, having four simultaneous spectra gives MINERVA a unique insight into telescope and detector level systematics which we have yet to fully capitalize on. In particular, we will explore the possibility of adapting the "vanking" stage of the Doppler pipeline, which is a sophisticated outlier rejection algorithm, to incorporate the knowledge that the four simultaneous spectra should produce identical radial velocities.

2.9 CONCLUSION

Since the commissioning of MINERVA, we have substantially modified our telescope control software and our Doppler pipeline. The MINERVA mission's secondary goal is accomplished much more efficiently with the control software changes. This work marks our first achievement toward our primary science goal of obtaining precise RVs. We have confirmed which of the IPs we had at our disposal would yield reliable results from our pipeline. These are the aforementioned time-invariant cubic spline function (the fixed IP) and the sum-of-Gaussians function. While testing the fixed IP, we have also confirmed that our spectrograph's intrinsic instrumental profile remains stable for months. When there is significant fluctuation in the intrinsic instrumental profile, it is likely due to disturbances to the instrument, as opposed to any natural and gradual perturbations within the instrument. The agreement between both IPs implies that using an instrumental profile from the cross dispersion direction, and therefore has systematic errors, is sufficient if the instrumental profile is stable. Consequently, we precisely characterized our spectrograph's instrumental profile from the cross-dispersion direction of the echellogram.

TABLE 2.4

PROPERTIES OF 51 PEG

STELLAR PARAMETERS:

Parameter	Description	EXOFASTv2	Reference (Bu06)	$\Delta\sigma$
M_*	Mass ($M_\odot$)	$1.095^{+0.066}_{-0.07}$	1.09 ± 0.109	0.039
R_*	Radius ($R_\odot$)	$1.139^{+0.03}_{-0.03}$	1.03 ± 0.07	1.431
L_*	Luminosity ($L_\odot$)	$1.39^{+0.056}_{-0.053}$	...	...
ρ_*	Density (cgs)	$1.05^{+0.12}_{-0.11}$	...	...
$\log g$	Surface Gravity (cm s^{-2})	$4.365^{+0.036}_{-0.041}$	4.449 ± 0.06	1.2
T_{eff}	Effective Temperature (K)	5875^{+73}_{-76}	5787 ± 44	1.002
[Fe/H]	Metallicity	$0.201^{+0.07}_{-0.069}$	0.2 ± 0.03	0.013
[Fe/H]$_0$	Initial Metallicity	$0.204^{+0.064}_{-0.065}$	...	...
Age	Age (Gyr)	$4.0^{+3.4}_{-2.5}$	...	...

TABLE 2.4 — CONTINUED

Parameter	Description	EXOFASTv2	Reference (Bu06)	$\Delta\sigma$
EEP	Equal Evolutionary Point	367^{+39}_{-37}	...	...
A_V	V-band extinction	$0.051^{+0.045}_{-0.036}$	...	...
σ_{SED}	SED photometry error scaling	$3.01^{+1.1}_{-0.7}$	...	...
d	Distance (pc)	$15.468^{+0.03}_{-0.029}$	15.36 ± 0.18	0.592
π	Parallax (mas)	$64.65^{+0.12}_{-0.12}$	...	...
PLANETARY PARAMETERS:				
P	Period (days)	$4.236^{+0.028}_{-0.025}$	4.230785 ± 0.000036	0.209
R_P	Radius (R_J)	$1.242^{+0.093}_{-0.094}$	...	...
T_C	Time of Conjunction (BJD$_{\text{TDB}}$)	$2458048.885^{+0.081}_{-0.062}$	...	...
T_0	Optimal Time of Conjunction (BJD$_{\text{TDB}}$)	$2458044.653^{+0.074}_{-0.068}$	...	...
a	Semi-major Axis (AU)	$0.0528^{+0.0011}_{-0.0012}$	0.0527 ± 0.003	0.031
i	Inclination (Degrees)	61^{+20}_{-27}	...	...

Table 2.4 — *Continued*

Parameter	Description	EXOFASTv2	Reference (Bu06)	$\Delta\sigma$
e	Eccentricity	$0.051^{+0.062}_{-0.036}$	0.013 ± 0.012^a	1.001
ω_*	Argument of Periastron (Degrees)	-73^{+200}_{-79}	58^a	...
T_{eq}	Equilibrium Temperature (K)	1315^{+18}_{-17}	...	...
M_P	Mass (M_J)	$0.56^{+0.3}_{-0.075}$	...	...
K	RV semi-amplitude (m/s)	$57.6^{+3.6}_{-3.7}$	55.94 ± 0.69	0.441
$\log K$	Log of RV semi-amplitude	$1.76^{+0.026}_{-0.029}$	...	...
R_P/R_*	Radius of planet in stellar radii	$0.112^{+0.0091}_{-0.0089}$	...	...
a/R_*	Semi-major axis in stellar radii	$9.98^{+0.35}_{-0.38}$	...	...
ρ_P	Density (cgs)	$0.38^{+0.25}_{-0.1}$	...	...
$\log g_P$	Surface Gravity	$2.97^{+0.2}_{-0.11}$	...	...
Θ	Safronov Number	$0.0439^{+0.025}_{-0.007}$	...	...
$\langle F \rangle$	Incident Flux (10^9 erg s^{-1} cm^2)	$0.675^{+0.038}_{-0.035}$	...	...
T_P	Time of Periastron (BJD$_{\text{TDB}}$)	$2458050.24^{+0.98}_{-1.0}$	...	...

TABLE 2.4 — CONTINUED

Parameter	Description	EXOFASTv2	Reference (Bu06)	$\Delta\sigma$
T_S	Time of Eclipse (BJD$_{\text{TDB}}$)	$2458050.941^{+0.073}_{-0.087}$	...	...
T_A	Time of Ascending Node (BJD$_{\text{TDB}}$)	$2458047.78^{+0.065}_{-0.079}$	...	...
T_D	Time of Descending Node (BJD$_{\text{TDB}}$)	$2458049.93^{+0.07}_{-0.063}$	...	...
$e\cos\omega_*$	....	$-0.018^{+0.032}_{-0.063}$	...	...
$e\sin\omega_*$	....	$-0.008^{+0.032}_{-0.052}$	...	...
$M_P\sin i$	Minimum mass (M_J)	$0.484^{+0.036}_{-0.037}$	0.472 ± 0.039	0.223
M_P/M_*	Mass ratio	$0.000487^{+0.00028}_{-0.000063}$	...	...
d/R_*	Separation at mid transit	$10.07^{+0.59}_{-0.55}$	...	...
P_T	A priori non-grazing transit prob	$0.0881^{+0.0054}_{-0.0051}$	...	...
$P_{T,G}$	A priori transit prob	$0.1104^{+0.0063}_{-0.0061}$	...	...
P_S	A priori non-grazing eclipse prob	$0.0905^{+0.0065}_{-0.005}$	...	...
$P_{S,G}$	A priori eclipse prob	$0.1133^{+0.0076}_{-0.0057}$	...	...
RMS	Root Mean Square of residuals (m/s)	5.6	7.0	...

TABLE 2.4 — *CONTINUED*

Parameter	Description	EXOFASTv2	Reference (Bu06)	$\Delta\sigma$
TELESCOPE PARAMETERS:				
$\gamma_{\rm rel}$	Relative RV Offset (m/s)	$-5.0^{+2.5}_{-2.5}$	...	...
σ_J	RV Jitter (m/s)	$7.7^{+2.8b}_{-1.9}$	3.7^b	...
σ_J^2	RV Jitter Variance	59^{+51}_{-26}	...	...
$N_{\rm obs}$	Number of observations	15	256	...

NOTE.

[a] The uncertainties reported by Bu06 for e and ω_* are non-Gaussian because the uncertainty of e is comparable to e, i.e. $\sigma_e \gtrsim e/2$.

[b] Our RV jitter is informed by the aforementioned radial velocities while the Bu06 value is informed merely by other stellar parameters.

3

Constraining the CME Core Heating and Energy Budget with SOHO/UVCS

This thesis chapter originally appeared in the literature as Wilson, M. L., Raymond, J. C., Lepri, S. T., et al. 2022, ApJ, 927, 27

In 2021, we acknowledge the 50th anniversary of coronal mass ejection (CME) observations along with the advent of a privatized billionaire space race. A decade into the very first space race, observations of bright plasma from a CME were recorded for the first time (Hansen et al., 1971;

Tousey et al., 1973; Gosling et al., 1974). Now, CMEs are understood to be magnetized plasma clouds originating from long filament or prominence loops of relatively cool plasma. Stored magnetic energy is abruptly released with the cool plasma, which subsequently expands while travelling through the corona and interplanetary medium. The physical mechanisms that launch and continuously drive the behavior seen in CMEs are still ambiguous. This ambiguity results in a broad range of physical interpretations being considered to explain the initiation, the morphology, the composition, and the total energy budget of CMEs.

Many of the observationally-supported interpretations suggest CMEs consist of a bright outer shell that leads a faint flux rope which surrounds a dense core of plasma (Illing & Hundhausen, 1985). At supersonic speeds, the leading edge is preceded by a shock front of gas that often correlates with solar energetic particles (SEPs) that can disrupt satellite communications (e.g., Kahler, 1994; Laming et al., 2013). At any speed, the leading edge is the simplest feature to track in white light images as the CME propagates through the corona. It contains bright coronal gas that is initially compressed by the eruption (e.g., Ma et al., 2011; Howard & Vourlidas, 2018). The flux rope is often referred to as the void because of how it appears in images and spectra due to the flux rope's dim brightness. Instead, measurements of its ionization states are gathered *in situ* near 1 AU for interplanetary coronal mass ejections (ICMEs) (e.g., Lepri et al., 2001; Rivera et al., 2019b). The dense core of the CME contains a large mass of plasma spanning a wide range of ionization states. This plasma originates from a (filament or) prominence loop that can extend above a current sheet as the prominence material erupts from the solar surface (e.g., Liewer et al., 2009; Reeves et al., 2015). Overall, these observed features form the canonical three-part CME that consists of a leading edge, a flux rope, and a core. Upon eruption, the energy budget of this CME might be influenced by an accompanying solar flare.

For hundreds of simultaneous flare-CME events, many terms in the energy budget are within the range of 10^{29}—10^{32} erg (e.g., Aschwanden et al., 2014; Aschwanden, 2017; Emslie et al., 2005). When there is no accompanying flare, the energy budget of the CME is often found for only one or two components of the three-part CME. Due to their frequently imaged bright features, the core and leading edge are the two most convenient components of the CME to study when determining

the energy budget; although, the magnetic energy requires measurements from the flux rope.

Compared to the rest of the total energy budget, the magnetic energy of a CME is difficult to measure. Serendipitous measurements of the magnetic energy are usually gathered *in situ* near 1 AU if an ICME bombards a spacecraft (e.g., Davies et al., 2020; Scolini et al., 2020), while targeted measurements are typically acquired through remote observations of pre-CME prominences and filaments on the solar disk (e.g., Leroy et al., 1983; Solanki et al., 2003). Upon eruption, most of the CME's magnetic energy is concentrated in the flux rope. It is difficult to track this magnetic energy after the eruption due to the faint emission within this component of the CME. Attempts have been made to bridge the gap between the measurements of the CME magnetic field at 1 $R_\odot$ (remotely) and 1 AU (*in situ*). Magnetohydrodynamic (MHD) models have been used to gain insight on the morphology of the magnetic field structure by extrapolating from solar disk measurements, extrapolating from *in situ* measurements, or interpolating between both measurements (e.g., Usmanov & Dryer, 1995; Feng et al., 2010). However, the mechanisms that transform the complex, coronal flux rope into a relaxed, interplanetary plasma cloud are still largely unconfirmed. This creates much uncertainty for magnetic energy estimates of CMEs seen traveling through the corona, frequently via white light images.

It is much more feasible to measure and continuously track the kinetic and potential energy components of the CME energy budget. Both forms of energy require a value for the CME's mass, which can be estimated directly from white light coronagraph images. The images show features along the plane of sky (POS) and capture the light scattered by free electrons; and, the information inferred from the features is averaged along the line-of-sight (LOS) within the optically thin coronal medium. Such information can be misinterpreted due to projection effects. Frequently, geometric assumptions are made to mitigate misunderstandings caused by projection effects when determining the mass or three-dimensional structure of CMEs (e.g., Ciaravella et al., 2003; Emslie et al., 2004; Vourlidas et al., 2010). For the kinetic and potential energy, the uncertainty due to errors in the mass estimate can be avoided if only the specific energy (i.e., quantities of energy per mass) is used to compare and contrast the energy budgets of various CMEs, which may have masses that are evaluated with distinct techniques and sources of uncertainty.

The heating energy is another component of the CME energy budget that is often plagued by uncertainties. This is because the physical mechanisms responsible for continuously generating thermal energy are not understood. Processes that cool the plasma or redistribute its thermal energy can occur while the plasma is being heating even though observations may sometimes indicate minor changes in the plasma temperature. Evidence for the extended, post-eruption heating has been found through observations of erupting prominence material observed as absorption features that are later seen as emission features, presumably due to its temperature increasing (Filippov & Koutchmy, 2002; Lee et al., 2017). Additionally, *in situ* measurements at 1 AU have indicated the need for CME heating until the ionization states are frozen-in (Rakowski et al., 2007), i.e. until the plasma density is low enough or velocity is fast enough for the local environment's ionization and recombination processes to no longer alter the CME's ionization states. Quantifying the energy of the heating process may provide clues for its underlying physical mechanisms. Several studies have quantitatively assessed the cumulative heating energy component of the energy budget and found it to be comparable to the kinetic energy (e.g., Akmal et al., 2001; Murphy et al., 2011). It is clear that the heating is an important process that can improve our understanding of the CME's evolution during and after the initial eruption.

In this paper, we provide constraints on the heating energy of localized plasma within a CME by using fortuitous spectroscopic measurements of a CME crossing the (single) slit of a coronagraph spectrometer at multiple heights in the corona. Our work with this unique dataset is supported by measurements from solar disk photometry and white light coronagraph images of the CME. This paper is organized as follows.

In Section 3.1, we describe the data acquired from three instruments of the *Solar and Heliospheric Observatory* (*SOHO*). We have photometry from the Extreme ultraviolet Imaging Telescope (EIT), white light images from the Large Angle Spectroscopic Coronagraph (LASCO), and spectra from the Ultraviolet Coronagraph Spectrometer (UVCS) to study the CME that erupted in 1999 on May 17. In Section 3.2, we interpret the features seen within the data to distinguish between a variety of structures within the CME core. In Section 3.3, we discuss how plasma diagnostics inferred from the spectra constrain the plasma parameters. The constraints provide upper and lower

limits on the physical properties that we find from our 1D numerical models and non-equilibrium ionization (NEI) calculations, which we explain in Section 3.4. The constrained 1D models are compared to the 3D MHD model of a slow CME. This CME's evolution is simulated by the Magnetohydrodynamic Algorithm outside a Sphere (MAS) code and we discuss this in Section 3.5. Our energy budget results and heating rates for the observed CME are given in Section 3.6. We demonstrate our methodology through the detailed analysis presented for one heating parameterization. The analyses for our other parameterizations are given in the Appendices. Lastly, in Section 3.7 we summarize our work and give closing remarks about the current dearth of coronagraph spectrometers, which is an issue that will be resolved by the UVSC Pathfinder and LOCKYER missions.

3.1 Observations of the CME

We study observations taken of a CME that occurred on 17 May 1999. Three instruments on board the *SOHO* spacecraft clearly captured the CME: EIT between 00:48 and 03:12 UTC, LASCO C2 camera between 00:49 and 5:25 UTC, and UVCS between 03:08 and 04:38 UTC. We used EIT and LASCO to confirm the CME detection and obtain rough estimates of the CME's velocity. We use spectra from UVCS to analyze the evolution of its physical properties.

3.1.1 EIT Photometry

The EIT (Delaboudinière et al., 1995) observations show filamentary structures erupting near the northwest limb of the Sun. This is most evident in the 195 Å bandpass with images taken at a 12 minute cadence and an exposure time of 4.5 seconds. These structures can be seen in the difference image given in Figure 3.1. Multiple filamentary structures are near the position angle (PA) of 315° (counter-clockwise from north pole). They elongate and travel radially outward between times 00:48 and 3:00 UTC. It is not clear where the launch site was on the Sun given that only one image of these structures was captured by the 304 Å bandpass. Taken at 1:18 UTC with an exposure time of 32 seconds, the 304 Å image shows many towering prominence loops that extend downward to footpoints that do not reside in the foreground. These observations suggest that, before

00:48 UTC, the CME either has yet to launch or is traveling behind the solar disk; and, beyond 3:00 UTC, the CME material has traveled beyond the field of view or is no longer emitting radiation within the bandpass. Images in the 171 Å and 284 Å bandpasses were taken at times outside of this time window and therefore did not provide relevant information. Based on the time window, the structures imaged by EIT begin to erupt at least two hours before the UVCS observations capture the CME at a heliocentric distance of 1.4 $R_\odot$ along SOHO's POS. Assuming the EIT structures continued to travel radially outward at a constant speed, the observation times suggest a speed of $\sim$80 km s^{-1} along the POS for CME material traveling from the limb to a heliocentric distance of 1.4 $R_\odot$. However, we later discuss the importance of confirming observations of the same, specific structures at multiple heights when attempting to deduce the velocity of CME material.

3.1.2 LASCO Photometry

White light photometry of LASCO (Brueckner et al., 1995) can be obtained from any of its three cameras: C1, C2, and C3. The C1 camera however was no longer operational after 1998; therefore, data on the 1999 CME is available only from the C2 and C3 camera. They provide a combined field of view covering 2.5 to 30 $R_\odot$. Among the LASCO images that capture the CME, we primarily consider the images that occur near the UVCS observation times. This is limited to the C2 images taken from 2:49 to 4:49 UTC each with an exposure time of 25 seconds. An example of when UVCS observations coincide with LASCO is given in Figure 3.2. At distinct times, the single slit aperture of the UVCS instrument monitors the corona at distinct heliocentric distances (d_H). In our example, we overlay the slit (illustrated as a blue line) onto a difference image of LASCO white light photometry only if the UVCS slit-image is taken at a time within $\pm$20 minutes of a single LASCO C2 image. Within this time interval, Figure 3.2 shows the UVCS slit's center at 1.7, 1.9, 2.1, and 2.6 $R_\odot$ at different times. The UVCS observations that have an assigned identification (ID) ranging from 6 to 17 have (blue) slits that are overlaid onto the difference image. These UVCS observation IDs and times are given in Table 3.1.

The positions of the slit during this CME event suggest that UVCS primarily observed the bright, dense core of the CME. Throughout all of the observations listed in Table 3.1, neither the
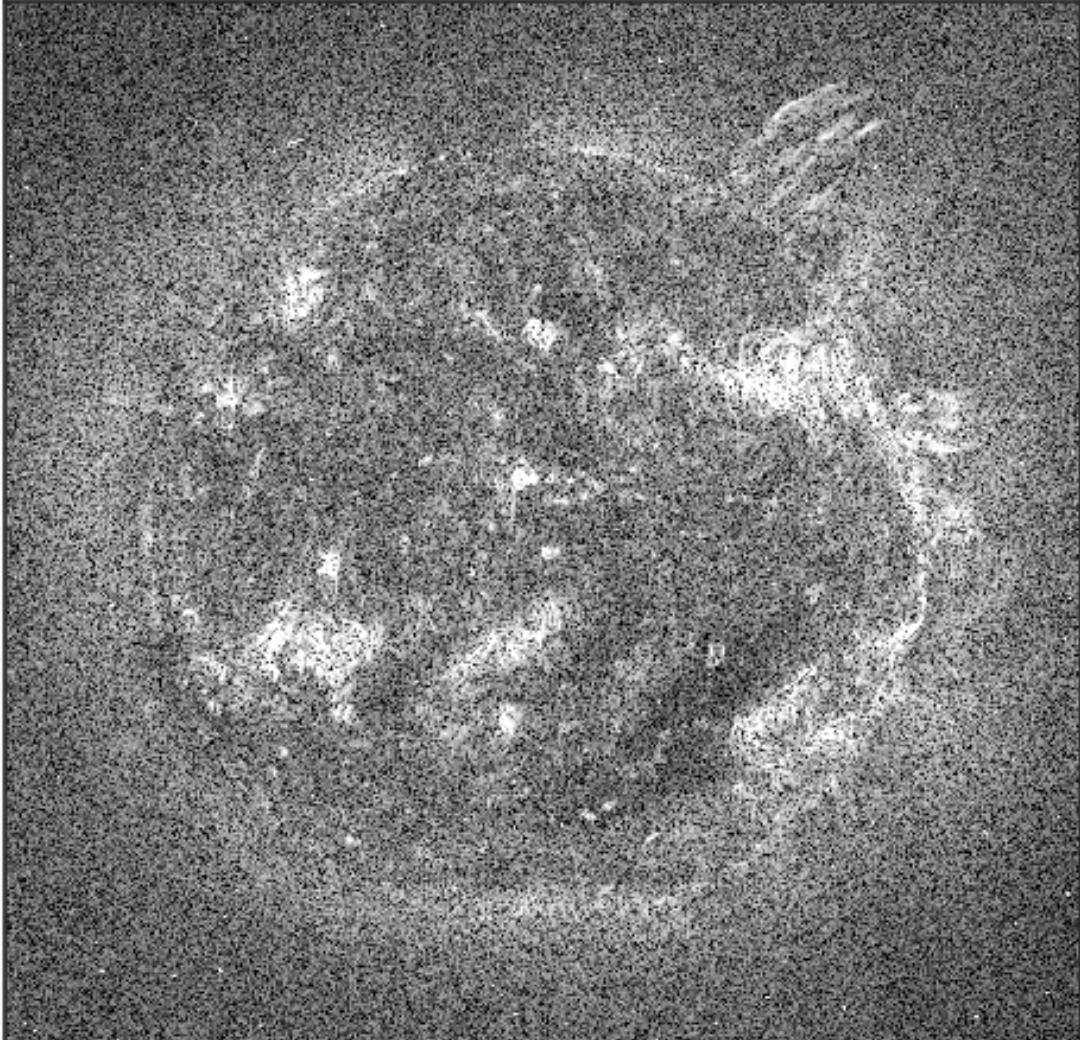
Figure 3.1: EIT difference image from observations taken at 02:24 and 02:36 UTC in the 195 Å bandpass. In the top right, plumes of elongated CME material continuously and slowly erupt off the limb between 00:48 and 03:12 UTC.

CME's current sheet, the faint void, nor the leading edge are discernable within the UVCS data. According to the CDAW CME Catalog (Gopalswamy et al., 2009), the leading edge seen in LASCO's C2 and C3 images travels at 500 km s^{-1} beyond 3 $R_\odot$ with a 5 m s^{-2} acceleration on average along the POS. The core of the CME is seen in the same white light photometry and contains amorphous features that significantly alter in appearance from one image to another. This makes it difficult to determine the core's speed when using only white light imagery. Based on the C2 images we use, this problem is exacerbated with core material at lower heights in the corona. As the material expands and travels higher in the corona, some features of the CME core are more clear in their

discernible shape in one image than another image, and they also become fainter. Consequently, we depend on the UVCS information for velocity estimates of features seen within the CME core. However, the leading edge velocity from LASCO does serve as an upper limit for the core's velocity along the POS.
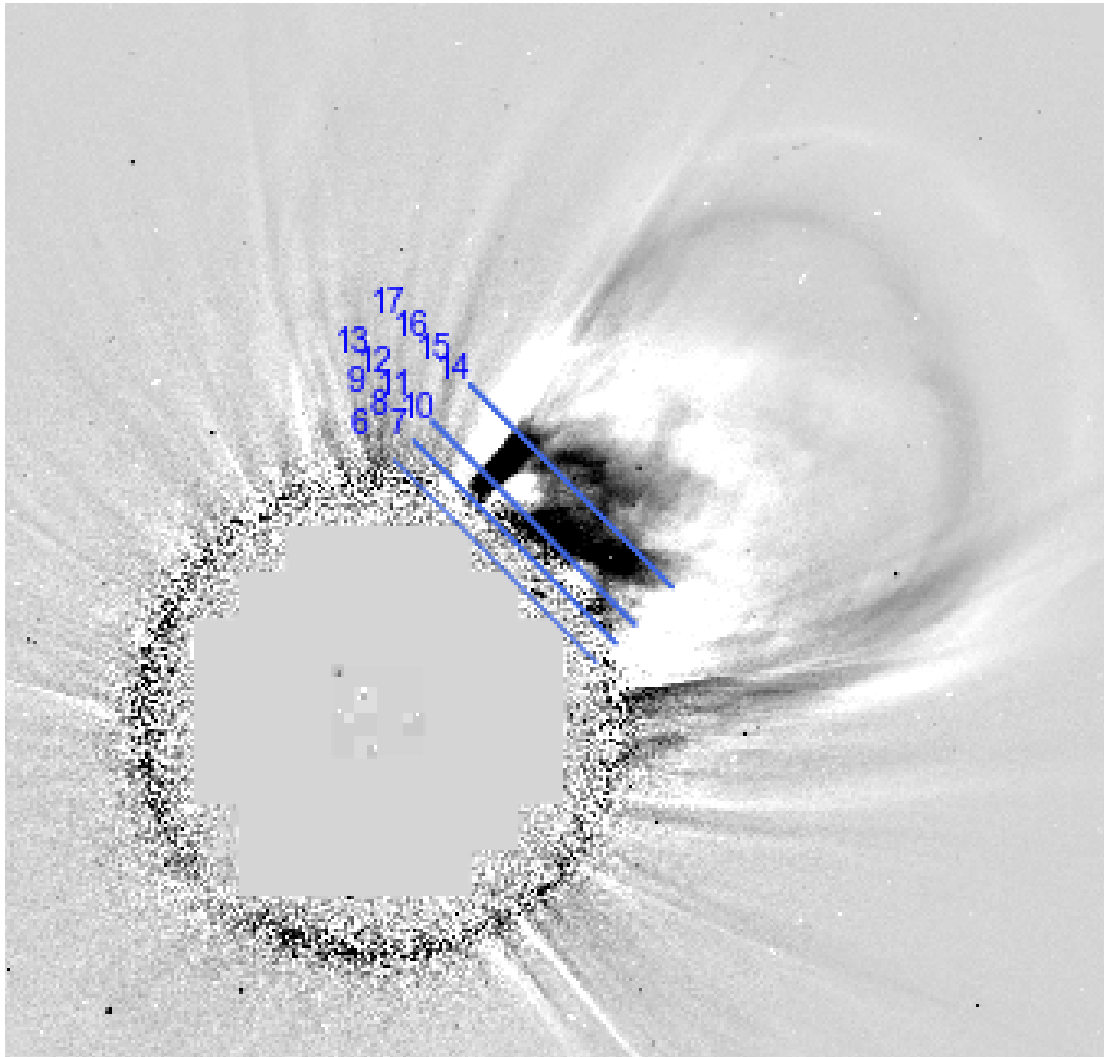
Figure 3.2: LASCO difference image from observations taken at 03:25 and 03:49 UTC show the CME's amorphous core and shell-like leading edge. The blue lines represent the UVCS slit aperture at times corresponding to the observations IDs (cf. Table 3.1).

3.1.3 UVCS Observations of CME Core

Effective ultraviolet coronograph spectrometers attempt to minimize the contamination of bright solar disk emission while maximizing the signal of relatively weak coronal emission lines. Many spectrometers constructed for this purpose are modeled after the design originally introduced by Kohl et al. (1978). As one of such instruments, UVCS was designed to detect coronal emission covering the 940–1360 Å wavelength range as a means for studying the physical conditions of coronal plasma from $d_H \approx 1.5\, R_\odot$ out to $d_H \approx 10\, R_\odot$ away from the center of the solar disk in the plane of sky (Kohl et al., 1995, 2006; Gardner et al., 1996, 2000, 2002). UVCS consists of two spectrometers (Pernechele et al., 1997): the Lyman-α channel can cover the 1145–1285 Å range but is optimized for the H I Lyman-α line at 1216 Å while the O VI channel can cover the 940–1125 Å range but is optimized for the O VI 1032 and 1038 Å doublet lines. In this work, we only use data from the O VI channel. We analyze data from both the "primary" light path and the "redundant" light path, albeit both paths lead to the O VI detector. The redundant mirror provides the spectral coverage needed to monitor H I Lyman-α emission without using the Lyman-α channel.

On 17 May 1999, UVCS was staring near the northwest limb of the Sun at a position angle of $315°$ with the slit positioned at heliocentric distances ranging from 1.42 to 3.10 $R_\odot$. The core of a CME passes through the field of view and there are 26 images taken with exposure times of either 180 seconds or 200 seconds. This is tabulated in Table 3.1 and all of these images capture features of the CME core at the same position angle. There are no observations that occur immediately before or immediately after the CME event at this position angle. The spatial binning along the slit is 3 pixels (21").

Due to the limitations of telemetry, three distinct panels within the O VI channel's spectral coverage were stored. As shown in the example of Figure 3.3, the three panels were stored with a binning of 3, 2, and 2 pixels in the dispersion direction which corresponds to -0.298, -0.199, and -0.199 Å respectively for the primary light path and 0.274, 0.183, and 0.183 respectively for the redundant light path. The negative dispersion indicates that the wavelengths will increase in the opposite direction (as seen in Figure 3.3). The three panels have wavelength ranges respectively cor-

responding to 1023–1043, 979–993, and 975–978 Å for the primary path. For the redundant path, the wavelength ranges are 1163–1182, 1209–1222, 1223–1226 Å respectively. See Table 3.2 for the most prominent spectral lines identified along with their peak ion formation temperature under ionization equilibrium. The wavelength calibration, flux calibration, and corrections in detector distortions and flat fielding are processed via the UVCS Data Analysis Software version 5.1 (DAS51).
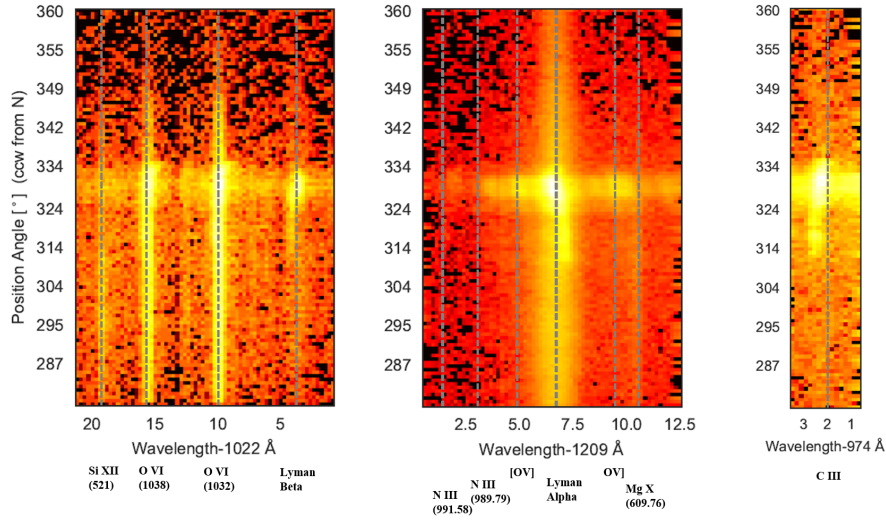
Figure 3.3: UVCS data taken when slit aperture is positioned to $d_H = 1.4\,R_\odot$ at 03:08 UTC. From top to bottom, the spectral lines in this example show the background corona, a very bright clump of CME core material, and diffuse CME core material.

3.2 DATA ANALYSIS

As shown in Figure 3.3, the three UVCS panels have information from the ultraviolet spectral lines listed in Table 3.2. In the leftmost panel, the spectral lines of interest come from the primary optical path. The Si XII line at 521 Å is present in its second spectral order at 1042 Å. Between the O VI doublet lines (1032 Å and 1038 Å) is a H I Lyman-α instrumental ghost due to imperfect spacing of grating grooves. In the middle panel, the spectral lines come from the primary and redundant optical paths. The two N III lines are from the primary path and the rest are from the redundant path. Similar to the Si XII line, the Mg X line at 610 Å is detected in its second spectral order at 1220 Å. The rightmost panel only contains the C III emission at 977 Å coming from the primary path.
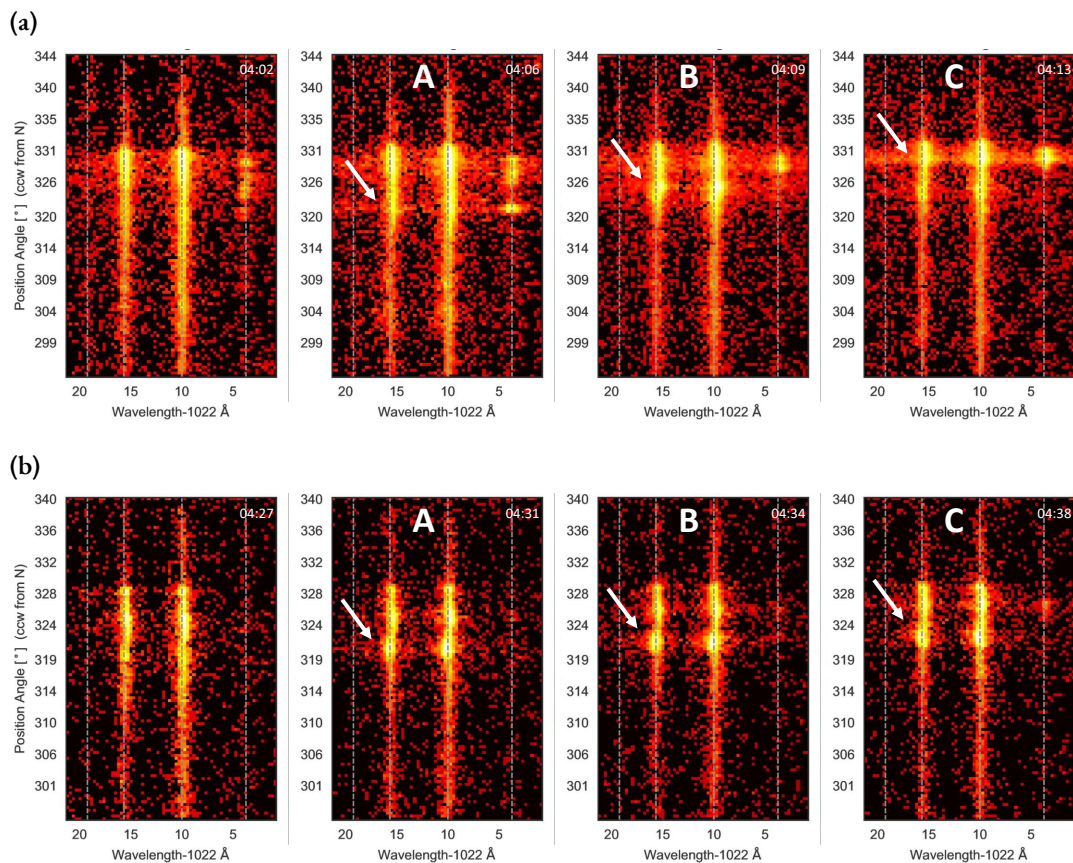
Figure 3.4: For four exposures, the UVCS panel showing the O VI doublet lines is presented. **(a)** This row corresponds to the last four exposures with the slit at $d_H = 2.6\,R_\odot$. **(b)** This row corresponds to the last four exposures with the slit at $d_H = 3.1\,R_\odot$.

At various position angles along the slit, material from the CME or background corona can be Doppler shifted away from the gray dashed line in Figure 3.3. For example, in most of the spectral lines, there is an abnormally bright bulge at PA = 330°. This CME material extends to lower position angles along the slit. Near PA = 315°, the material is clearly redshifted.

From one image to another, there are only slight changes to the position angles and Doppler shifts of the CME material. Per spectral line, prominent features within the CME material can be tracked from one height to another by monitoring the consistency of the structure's position angle, Doppler shift, brightness relative to other spectral lines, and spatial size (along the slit). As the CME evolves, these characteristics should change; but, we expect only minor changes over the time intervals required for UVCS observations to shift from height to another. These shifts often occur at intervals of about ten minutes (cf. Table 3.1).

Tracking specific structures seen along the slit from one height to another becomes difficult if a structure becomes too faint or becomes visually mingled with another structure. Tracking can also be difficult if a structure observed at one height has similar characteristics as a different structure observed at a higher height. If one confuses distinct structures as the same structure, this will lead directly to a miscalculation of the velocity. An example of this occurs when distinct parts of the same elongated, filamentary structure are observed at distinct heights along the POS.

Tracking specific structures should not depend solely on observations of plasma that share similar characteristics at multiple heights. For the sake of accurately assessing the evolution of the specific clump of plasma, it is necessary to consider the reasons why the clump might be bright in one image and faint in the next image or be found at a different PA or different Doppler shift in subsequent images. In such scenarios, the continuity of information between images for a single clump of plasma becomes ambiguous. Therefore, we use three approaches to confirm that the single-slit UVCS has observed the same structure over multiple images at distinct coronal heights: we consider the spatial position, the brightness, and the velocity of clumps at each height.

3.2.1 CONFIRMATION FROM SPATIAL POSITION

The automated programming for UVCS operations was set to take 2, 2, 3, 3, 4, 5, and 7 exposures when observing heights 1.4, 1.5, 1.7, 1.9, 2.1, 2.6, and 3.1 $R_\odot$ respectively. The most images come from heights 2.6 and 3.1 $R_\odot$ and thus those images would provide the best chance at discerning the same material at multiple heights. The last four images taken at 2.6 $R_\odot$ are shown in Figure 3.4a and the last four images taken at 3.1 $R_\odot$ are shown in Figure 3.4b. Each image only shows the panel of the detector that contains the O VI doublet lines, and the visual contrast of each image is arbitrarily set to best emphasize the O VI features. Therefore, some H I Lyman-β features are present but difficult to see; and, the brightness of one image should not be compared to that of another.

At 2.6 $R_\odot$ (cf. Figure 3.4a), the first image contains a bright clump of CME core material at $330°$ in the O VI lines. This material extends to lower positions on the slit. The Lyman-β emission shows distinct clumps of H I material near the same position angle of $330°$. In the second image (*A*), the brightest clump of O VI material is slightly higher than before. There is now a clump at the lower

position of 322°, which has a slightly wider spectral width than the material at the same position angle in the previous image taken ∼3 minutes prior. The white arrow points at this new clump for the 1038 Å line, although the same phenomenon occurs at 1032 and 1026 Å and in other UVCS panels at 1216 and 977 Å that are not shown. The third image (*B*) shows the highest clump at a slightly higher position angle than 3 minutes prior, and the white arrow is higher to show that the lower clump's position is higher as well. Now, the H I emission at 1026 Å (and at 1216 Å) is relatively faint at that lower position but still has a clump of H I material that remains bright at the higher position. In the fourth and final image (*C*), the white arrow is nearly overlapping with the highest clump to indicate that much of the lower material seen 3 minutes prior is now predominantly at this high position, although some of this clump's material is still seen at the lower position. Therefore, between the four images taken at intervals of ∼3 minutes, there is a clump of plasma that seems to appear at image *A* and seems to be one portion of a filamentary structure that is seen again in image *B* and again in image *C*. The long filamentary structure, which is travelling outward at a near radial direction along the POS, must be oriented at a small angle from the slit. This would cause the same strand of material to be imaged at gradually higher (or gradually lower) position angles as it passes by. This is occurring while another bright strand of material is consistently seen in all four images in almost all spectral lines near PA = 331°. Although not shown, these phenomena amongst the four images are evident in the C III emission as well.

At 3.1 $R_\odot$ (cf. Figure 3.4b), similar phenomena occur. A bright bulge appears in image *A* (indicated by the white arrow) and its neighboring or connecting material (also indicated by the white arrow) seems to appear at slightly higher positions in image *B* and image *C*. This qualitative assessment of the clumps' positions is evidence to support the hypothesis that the clumps of plasma observed in the last three exposures with the slit at 2.6 $R_\odot$ are the same clumps of plasma observed in the last three exposures with the slit at 3.1 $R_\odot$. Although this is clear for the clumps marked by the white arrows, it is likely true also for the consistently bright clumps at the higher position along the slit. Clumps at the higher position angle seem to keep a similar size (along the slit) throughout images *A*, *B*, and *C* at 2.6 $R_\odot$; and at 3.1 $R_\odot$, the clumps at the higher position angle also exhibit a consistent size throughout images *A*, *B*, and *C*. Thus, the pattern of behavior seen at the higher

position angle remains the same between 2.6 and 3.1 $R_\odot$. For clumps at both position angles, the two O VI emission lines provide the best evidence to qualitatively confirm the hypothesis, but other spectral lines have their own features that follow similar patterns which support the hypothesis as well.

For the clumps observed at heights below 2.6 $R_\odot$, such patterns of behavior are not clearly seen. At each height below 2.6 $R_\odot$, only two, three, or four images were taken and no distinguishable feature seemed to "appear" at multiple heights (like the lowest clump at 2.6 $R_\odot$ that appears in image A and later appears at 3.1 $R_\odot$ again in image A). Ultimately, the spatial characteristics of the clumps observed below 2.6 $R_\odot$ do not confirm a multi-height detection.

3.2.2 Confirmation from Brightness

A more quantitative confirmation comes from the clumps' brightness at each height and is summarized in Figure 3.5. We record the total intensity for each spectral line after subtracting out the background corona. None of the UVCS exposures occur immediately before or after the CME event. Therefore, we use the relatively faint regions near the top and bottom of the detector (e.g., PA $\sim 340°$ or $300°$ for data in Figure 3.4) to determine the average background coronal flux for each spectral line and subtract it from the regions of CME material. The light curve shows the total intensity amongst all clumps within a given spectral line. Although we can clearly distinguish one clump from another along the slit aperture, the changes in position angle and brightness introduce uncertainties in defining a consistent size for each individual clump. This is exacerbated as multiple clumps become very close to one another along the slit aperture in a given image. Therefore, we maintain consistency by tracking the total brightness of all of the CME material along a given spectral line as one composite clump, instead of tracking the brightness of each individual clump.

Figure 3.5 shows light curves for the O VI 1032 Å emission (in units of 10^{10} photons steradian^{-1} cm^{-2} s^{-1}) and the H I 1216 Å emission (in units of 10^{12} photons steradian^{-1} cm^{-2} s^{-1}) for slit positions of 2.6 and 3.1 $R_\odot$. The vertical dashed line visually separates the data taken at 2.6 $R_\odot$ from the data taken at 3.1 $R_\odot$. The intensities at 3.1 $R_\odot$ are arbitrarily amplified by a factor four for 1032 Å and thirty for 1216 Å in order to visually place the light curves on the same scale.

As previously mentioned, the most images per height are taken at 2.6 and 3.1 $R_\odot$, which give enough information to make useful height-to-height comparisons. In the light curves for 1032 Å, the final three images (*A*, *B*, and *C*) at both heights yield a pattern where the composite clump intensity is brightest for image *B*, second-brightest for image *C*, and third-brightest for image *A*. This suggests that the composite clumps observed at 2.6 $R_\odot$ are the same as the composite clumps observed at 3.1 $R_\odot$. The same can be said about the light curves for 1216 Å, which have their own pattern of monotonically increasing over time. Although this height-to-height similarity may also be true for the images taken prior to seeing composite clump *A*, we focus on the last three images since they provide the best signal to noise ratio.

We find these two forms of confirmation despite the composite clumps' decrease in brightness as they travel from 2.6 to 3.1 $R_\odot$. The O VI emission at 1032 Å drops by a factor four and the H I emission at 1216 Å drops by a factor of thirty. The difference in factors might be attributed to the H I being in a cooler region of the CME core that is separate along the LOS from the O VI. The general decrease in brightness can occur for many different reasons. Some of the decrease may come from a change in density and temperature as the material expands between 2.6 and 3.1 $R_\odot$. The decrease in brightness for distinct spectral lines can be due to changes in ionization states within the emitting plasma. Ultimately, the degeneracy amongst parameters that affect the CME's brightness obscures the specific underlying mechanisms that are responsible for the specific decreases in brightness observed by UVCS.

3.2.3 Multi-height velocity

Since composite clumps *A*, *B*, and *C* seem to appear in the UVCS observations at both 2.6 and 3.1 $R_\odot$, we can estimate their total velocities. We determine the POS velocity by accounting for the two distinct times each clump is observed at two distinct heights (and position angles) in the corona. At both heights, we find the intensity-weighted centroid of each composite clump for each spectral line. Using the centroid positions and observation times, we estimate an average velocity in the POS for the composite clump between 2.6 and 3.1 $R_\odot$. The centroid positions indicate a direction for the POS velocity vector that is almost radially outward. This is due to the composite clumps

being found at nearly the same position angles at 2.6 $R_\odot$ (with centroid PA $\sim 327°$) and 3.1 $R_\odot$ (with centroid PA $\sim 324°$). When all of these factors are considered, each composite clump within its respective spectral line yields a multi-height, average velocity in the POS equal to $\sim$250 km s^{-1}.

To give an example, we determine a centroid position for each spectral line in which composite clump B is found. For this clump, the average of the centroid PAs is $327.4°$ when the slit's center is at 2.6 $R_\odot$ and $323.7°$ when the slit's center is at 3.1 $R_\odot$. The distance between the centroids is 0.55 $R_\odot$ with a difference of 25 minutes in observation times. This corresponds to a speed of 255.1 km s^{-1} along the POS. This is applied to the clump's LOS velocity at 2.6 $R_\odot$ and its LOS velocity at 3.1 $R_\odot$. As a source of uncertainty, the estimated difference in times of observing clump B may be erroneous due to the 3-minute exposures. Considering this, an observation time difference of 28 minutes makes the POS velocity 227.8 km s^{-1} and a difference of 22 minutes yields 289.9 km s^{-1}, which suggests a $\sim$30 km s^{-1} uncertainty about the POS estimate of 255.1 km s^{-1}.

We determine the instantaneous LOS velocity component from Doppler shifts of each spectral line. As an example, the spectral lines emitted by clump B exhibit Doppler shifts that average to 54.3 km s^{-1} as a blueshift at 2.6 $R_\odot$ and 56.1 km s^{-1} as a redshift at 3.1 $R_\odot$. The transition from blueshift to redshift could be evidence of helical motion; but, there are not enough observations of clump B (at multiple heights) to confirm periodicity in its Doppler shifts and thus helicity in its motion.

For our final velocities, if a composite clump has a POS estimate of 250 km s^{-1} and a LOS estimate (for a given ion and spectral line) of 50 km s^{-1}, this altogether yields a total velocity magnitude of 255 km s^{-1} with a direction oriented $11°$ out of the POS. To account for unknown sources of error, we conservatively adopt an upper limit of 300 km s^{-1} and a lower limit of 200 km s^{-1} for each composite clump. This multi-height, average velocity is used in §3.3.2 to obtain the aforementioned velocity-based confirmation of composite clumps A, B, and C.

We do not attempt the velocity-based confirmation for composite clumps found at heights below 2.6 $R_\odot$ (i.e., $d_H =$1.4, 1.5, 1.7, 1.9, and 2.1). Considering their positions along the slit (as in §3.2.1) and their light curves (as in §3.2.2), there are not enough images taken at these heights to confirm that a clump captured at one height was also captured at another height. Without either of these

forms of confirmation, two distinct heights and observation times cannot be used to determine the multi-height velocity estimate of any of these clumps. Therefore, we exclude these clumps from the velocity-based confirmation test in §3.3.2. The lack of various forms of confirmation implies that each of these clumps were likely observed at only a single height, which is typical for observations by single-slit coronagraph spectrometers. Therefore, we do not use these clumps when constraining the CME core's physical properties as a function of height.
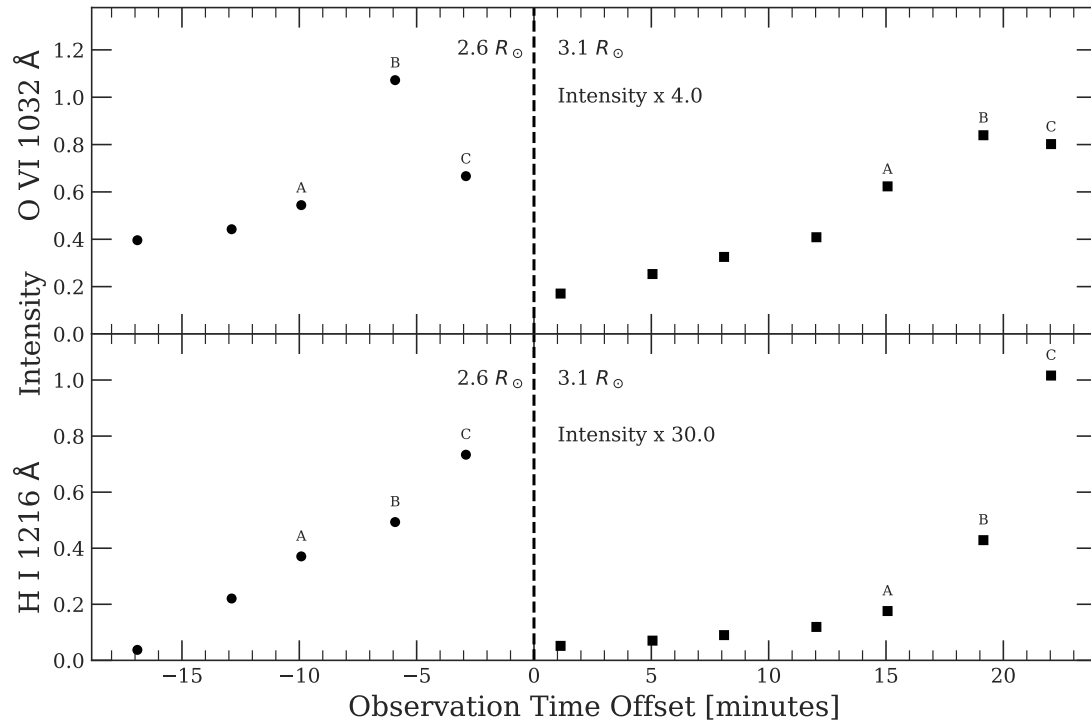
Figure 3.5: Light curve for composite clumps seen when the slit is positioned at 2.6 $R_\odot$ (left of vertical dashed line) and at 3.1 $R_\odot$ (right of vertical dashed line). Top: O VI 1032 Å light curves are shown. Bottom: H I 1216 Å light curves are shown. See text in §3.2.2 for further details.
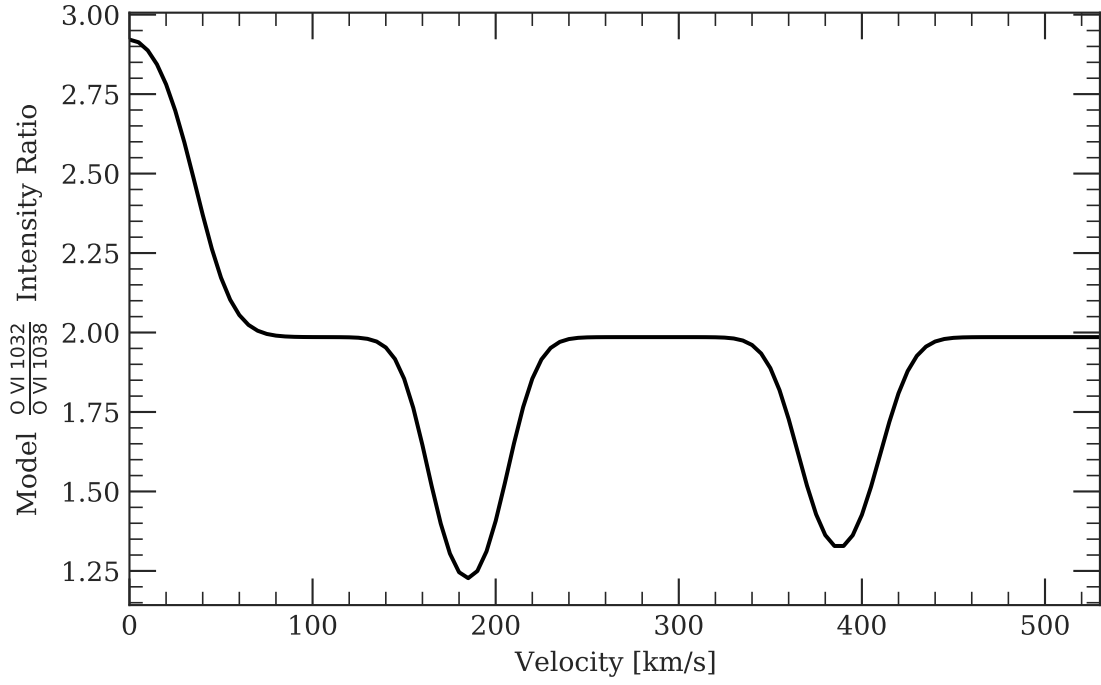
Figure 3.6: Model intensity ratios, I_{1032}/I_{1038}, when the scattering plasma is at a heliocentric distance $r = 3.0\ R_\odot$ under a temperature of 10^5 K and a density of 10^6 cm^{-3} while travelling radially outward from the solar surface.
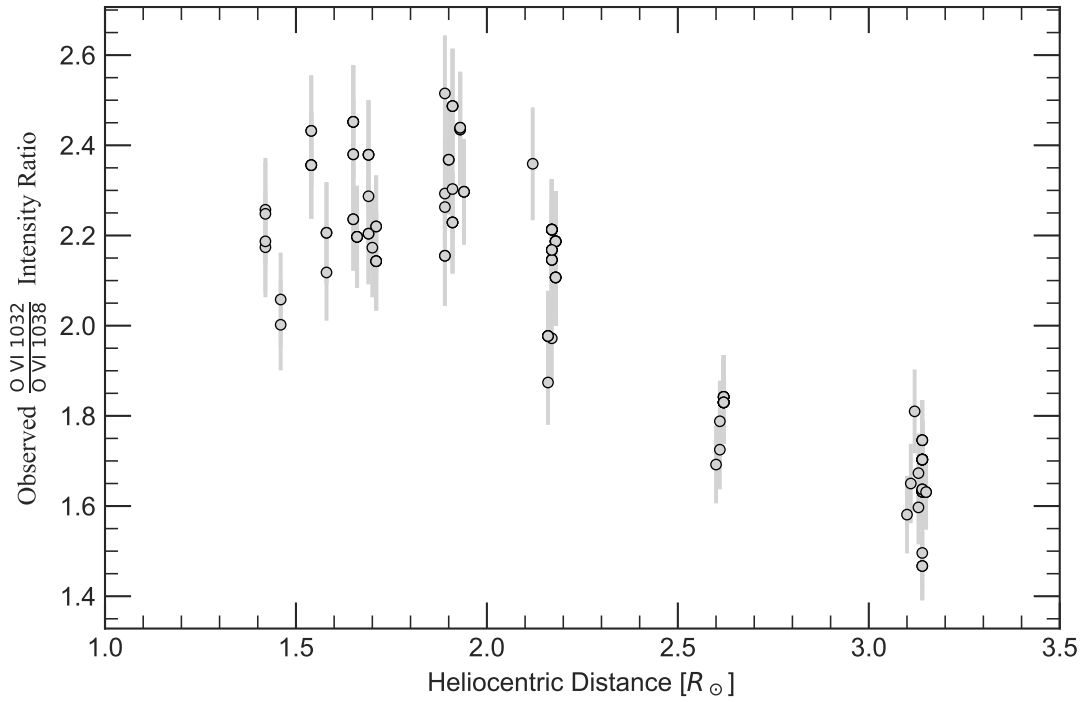
Figure 3.7: Intensity ratios of individual clumps observed in the O VI doublet lines.

TABLE 3.1: UVCS Observations

ID	Time (UTC)	$d_H\,(R_\odot)$	$\Delta t\,(s)$
0	03:07:50	1.4	200
1	03:11:14	1.4	200
2	03:15:13	1.5	200
3	03:18:39	1.5	200
4	03:22:36	1.7	180
5	03:26:04	1.7	180
6	03:29:33	1.7	180
7	03:33:34	1.9	180
8	03:37:04	1.9	180
9	03:40:33	1.9	180
10	03:44:32	2.1	180
11	03:48:03	2.1	180
12	03:51:32	2.1	180
13	03:55:02	2.1	180
14	03:58:47	2.6	180
15	04:02:18	2.6	180
16	04:05:46	2.6	180
17	04:09:16	2.6	180
18	04:12:47	2.6	180
19	04:16:49	3.1	200
20	04:20:14	3.1	180
21	04:23:47	3.1	200
22	04:27:13	3.1	180
23	04:30:45	3.1	200
24	04:34:10	3.1	180
25	04:37:43	3.1	180

Notes. The POS heliocentric distance, d_H, corresponds to the slit's central pixel.

TABLE 3.2: Prominent lines detected by UVCS during CME

Wavelength (Å)	Ion	Transition			$\log T_m$
1215.67	H I		Lyman-α		4.5
1025.72	H I		Lyman-β		4.5
977.02	C III	$2s^2\ {}^1S_0$	-	$2s2p\ {}^1P_1$	4.8
989.79, 991.58	N III	$2s^22p\ {}^2P_{1/2,3/2}$	-	$2s2p^2\ {}^2D_{3/2,5/2}$	4.9
1213.85	[O V]	$2s^2\ {}^1S_0$	-	$2s2p\ {}^3P_2$	5.4
1218.39	O V]	$2s^2\ {}^1S_0$	-	$2s2p\ {}^3P_1$	5.4
1031.91, 1037.61	O VI	$2s\ {}^2S_{1/2}$	-	$2p\ {}^2P_{3/2,1/2}$	5.5
609.76, 624.93	Mg X	$2s\ {}^2S_{1/2}$	-	$2p\ {}^2P_{3/2,1/2}$	6.1
499.37, 520.66	Si XII	$2s\ {}^2S_{1/2}$	-	$2p\ {}^2P_{3/2,1/2}$	6.4

Notes. The Mg X and Si XII spectral lines are seen in their second spectral order.

TABLE 3.3: UVCS composite clump intensity ratios

Ratio	A_1	A_2	B_1	B_2	C_1	C_2
$\frac{\text{O VI } 1032}{\text{O VI } 1038}$	1.788 ± 0.090	1.746 ± 0.089	1.842 ± 0.093	1.703 ± 0.086	1.830 ± 0.092	1.632 ± 0.083
$\frac{\text{H I } 1216}{\text{H I } 1026}$	293.581 ± 73.448	94.205 ± 23.725	297.988 ± 74.542	171.086 ± 43.043	355.283 ± 88.858	298.477 ± 74.985
$\frac{\text{O VI } 1026}{\text{H I } 1216}$	68.151 ± 20.448	3.761 ± 1.129	46.008 ± 13.803	6.811 ± 2.044	110.060 ± 33.021	16.890 ± 5.068
$\frac{\text{O VI } 1032}{\text{H I } 1026}$	0.232 ± 0.046	0.040 ± 0.008	0.154 ± 0.031	0.040 ± 0.008	0.310 ± 0.062	0.057 ± 0.011
$\frac{\text{O VI } 1032}{\text{O V } 1218}$	1.249 ± 0.375	0.245 ± 0.074	0.990 ± 0.297	0.276 ± 0.083	1.728 ± 0.519	0.409 ± 0.123
$\frac{\text{C III } 977}{\text{O VI } 1032}$	1.196 ± 0.359	0.093 ± 0.028	0.919 ± 0.276	0.144 ± 0.043	0.994 ± 0.298	0.179 ± 0.054

Notes. The relevant intensity ratios for three composite clumps (A, B, and C) are given. Each clump of CME material is labeled with a _1_ to represent its observation at the first coronal height, 2.6 $R_\odot$, and a _2_ to represent the second coronal height, 3.1 $R_\odot$. As elaborated in the text of §3.3.3, the intensity ratio uncertainties we adopt are based on both the calibration of UVCS data and the uncertainties within atomic models that describe each transition line.

3.3 Plasma Diagnostics

We can deduce the physical properties of the observed plasma by decomposing the components of the UV radiation observed. We use atomic models to determine the contribution from collisional excitation or radiative excitation of the emitting ions. Assuming the *coronal model approximation*, ions are excited from their ground state primarily by free electron collisions or photo-absorption and subsequently are de-excited primarily through spontaneous radiative decay. For excited ions in metastable states, the radiative decay rate is much slower and the collisional de-excitation rate is no longer negligible. Akmal et al. (2001) exploited this fact with the [O V] 1214 Å and O V] 1218 Å lines (cf. Table 3.2). Because of the collisional de-excitation, the intensity ratio of the O V lines became a useful density diagnostic for their CME analysis. The intensity ratio between the N III 990 and 992 Å lines can serve as a density diagnostic as well.

Unfortunately, for three of these lines, clumps A, B, and C are too faint to clearly distinguish them from the grating-scattered light from bright Lyman-α emission and the background corona. For the last three exposures taken at both 2.6 and 3.1 $R_\odot$, only the O V] 1218 Å line is bright enough. Therefore we do not make use of the other three lines in our plasma diagnostics. Also, the three clumps are not seen in the second-order Mg X and Si XII lines. We therefore discard these spectral lines from our analysis as well.

3.3.1 Two Components of Emissivity

The O VI doublet can serve as both a velocity and density diagnostic if we consider the aforementioned two processes of plasma excitation in the corona. For emission at wavelength λ, the two processes are responsible for the two components of emissivity. This yields a total local intensity I_λ, in units of photons cm^{-2} s^{-1} steradian^{-1}, that can be summarized as the following:

$$
\begin{aligned}
I_\lambda &= \frac{1}{4\pi} \int_{\mathrm{LOS}} (\varepsilon_{c,\lambda} + \varepsilon_{r,\lambda}) ds, \\
\varepsilon_{c,\lambda} &= n_{Z,z} \cdot n_e q_{ex,\lambda}(Z, z, T), \\
\varepsilon_{r,\lambda} &= n_{Z,z} \cdot I_\odot(\lambda_i + \delta\lambda_i)\sigma_\lambda \mathcal{W}(r).
\end{aligned}
\tag{3.1}
$$

The collisional excitation component $\varepsilon_{c,\lambda}$ includes collisional excitation rate coefficient $q_{ex,\lambda}$ in units of photons cm^3 s^{-1}. The radiative excitation component $\varepsilon_{r,\lambda}$ includes the dilution factor $\mathcal{W}(r)$ which is the solid angle, $2\pi\left(1 - \sqrt{1 - (R_\odot/r)^2}\right)$, subtended by the solar disk with respect to the scattering plasma that is at a heliocentric distance r away: a distance that is not confined to the POS like d_H. The effective cross section for scattering radiation of a given wavelength is σ_λ and the $I_\odot$ is the intensity from the solar disk radiation that is to be scattered. The incident radiation from the disk emits at λ_i and is Doppler shifted by $\delta\lambda_i$ with respect to the velocity of the plasma. The free electron density n_e only directly affects the collisional excitations. The ion density $n_{Z,z}$ directly affects the ion's collisional and radiative excitations. It can be characterized as $n_{Z,z} = n_H A_Z f_z$, where the number density of ion z of element Z is the product of the hydrogen density (n_H), the Z element's abundance (A_Z) relative to hydrogen, and the fraction (f_z) of all ions z of element Z. Values for $q_{ex,\lambda}$ are given by the CHIANTI atomic database (Dere et al., 1997, 2019). Values for σ_λ are based on oscillator strengths from CHIANTI, and values for $I_\odot$ are based on observations from Vernazza & Reeves (1978) taken near solar minimum. We multiply their $I_\odot(\lambda_i = \text{H I } 1216)$ values by a factor of 1.37 and all other solar disk emission lines by 1.5 to account for the solar maximum activity in 1999 according to measurements from the *UARS*/SOLSTICE instrument (Rottman et al., 2001).

The ratio of the O VI doublet lines, I_{1032}/I_{1038}, can be a useful diagnostic when their collisional and radiative components are considered. The ratio of their collisional components is $\varepsilon_{c,1032}/\varepsilon_{c,1038} = 2$ due to the collision strengths of their atomic transitions. Consequently, the ratio of total intensities becomes $R = I_{1032}/I_{1038} = 2.0$ when the collisional components dominate. When both radiative components dominate, the ratio becomes $R > 2$ and indicates a slow velocity (i.e., small $\delta\lambda_i$) for the scattering plasma (cf. Figure 3.6). However, at speeds greater than 100 km s^{-1} the ratio of total intensities becomes $R \leq 2.0$. Figure 3.6 shows an example of how these characteristics of the O VI ratio can serve as a useful velocity diagnostic for the CME that we study. Pumping of the 1038 Å line's radiative component brings the ratio to $R < 2.0$. This radiative pumping happens in Figure 3.6 due to the Doppler-shifted solar disk emission from C II: 1036.34 Å or 1037.02 Å following the transition $2s^2 2p\ ^2P_{1/2 \text{ or } 3/2} - 2s2p^2\ ^2S_{1/2}$. This is applicable for plasma traveling near 400 or

200 km s^{-1} respectively.

Due to thermal broadening of the absorption line profiles, the range of $R < 2$ velocities and $R > 2$ velocities can broaden under hotter conditions. These ranges are also affected by our assumption of 25 km s^{-1} for any nonthermal broadening. As long as the CME's velocity is roughly estimated and the observed ratio R deviates from 2.0, the O VI doublet lines can provide tighter constraints on the range of original velocity estimates. While the O VI doublet is radiatively pumped by Doppler-shifted emission, we can take the ratio between a line's collisional component and radiative component to evaluate an average electron density:

$$n_e = \frac{I_\odot(\lambda_i = \text{C II } 1037)\sigma_{1038}\mathcal{W}(\text{r})}{q_{ex,1038}}\frac{R}{2-R} \, , \, R < 2, \tag{3.2}$$

which is useful for clumps A, B, and C traveling at $\sim$250 km s^{-1}.

Using the same concepts, we can also estimate a LOS thickness of the plasma cloud. Once the plasma's intensity is measured, we can exercise a forward modelling procedure to estimate the two components of emissivity by using a model temperature, density (and ionization state), and velocity. With I_λ being measured and the emissivities being modelled, we can estimate a LOS length s_{LOS} of the emitting plasma cloud. To set an observational constraint on our model emissivities, we require that the estimated LOS length is greater than 10% of the observed clump's POS size along the slit s_{slit} and less than three times the clump's POS size:

$$0.1 \times s_{slit} < s_{LOS} < 3 \times s_{slit}, \tag{3.3}$$

which can serve as useful upper and lower limits, especially when an observed clump is very faint and its s_{slit} is difficult to determine. As an example of a typical size, clump B's average size amongst its spectral lines is $s_{slit} = 0.57 \, R_\odot$ at 2.6 $R_\odot$ and $s_{slit} = 0.63 \, R_\odot$ at 3.1 $R_\odot$. This size is defined by the distance between positions of median-intensity on either side of the peak-intensity of the composite clump.

All of the techniques used in Equations 3.1, 3.2, 3.3 can exploit the Doppler dimming effect (Hyder & Lites, 1970) of the two-component emissivity observed from coronal, ultraviolet radiation.

Techniques like these can yield diagnostics on the emitting plasma and have been employed by many spectroscopic studies of CMEs (e.g., Ciaravella et al., 2001; Raymond & Ciaravella, 2004; Bemporad et al., 2006) and the solar wind (e.g., Kohl & Withbroe, 1982; Noci et al., 1987; Cranmer et al., 2008; Strachan et al., 2012; Gilly & Cranmer, 2020).

3.3.2   Confirmation from Velocity

We use the O VI doublet ratio as a velocity diagnostic to confirm or reject the notion that the single-slit UVCS serendipitously captured images of the same unpredictable CME material at multiple heights in the corona. We assign $\pm 5\%$ uncertainties to our observed $\frac{\text{O VI 1032}}{\text{O VI 1038}}$ intensity ratios to account primarily for relatively minor uncertainties in the radiative components' solar disk line profiles and effective scattering cross sections. The ratio for each individual clump within each image of the UVCS observations is plotted in Figure 3.7.

Below 2.1 $R_{\odot}$, the $R > 2$ ratios imply that the clumps have speeds between 0 and 100 km s^{-1} (cf. §3.3.1 and Figure 3.6). In this case, the greatest intensity ratio observed, $R = 2.52$, corresponds to the slowest velocity estimate, which is roughly ~ 45 km s^{-1} depending on the density and temperature of the plasma. However, as mentioned in §3.2.3, the velocity is not confirmed by observations of the same clump at multiple heights.

At 2.1 $R_{\odot}$, the $R \approx 2$ ratios suggest that the O VI doublet alone is no longer a useful diagnostic. If the CME core material is accelerating, the instaneous velocities estimated from the $R > 2$ ratios below 2.1 $R_{\odot}$ can act as a lower limit for the velocities determined at 2.1 $R_{\odot}$ with $R \approx 2$ ratios. This still leaves much ambiguity in the clumps' velocities as well as a lack of confirmation in their multi-height detection. Thus, these clumps are not included in our observational constraints of the CME core.

Above 2.1 $R_{\odot}$, the observed $R < 2$ ratios imply that the velocity can be determined if a different, independent estimate of the velocity is first acquired. We elaborated in §3.2.3 how the three composite clumps observed at 2.6 and 3.1 $R_{\odot}$ have velocities of ~ 250 km s^{-1}. Therefore, we constrain the model intensity ratios (like that of Figure 3.6) to $R < 2$ models that correspond to velocities between 200 and 300 km s^{-1}. Figure 3.6 is an example showing how there are $R < 2$ models that

reside within this velocity range. Therefore, the physical conditions modelled can be constrained by the observed intensity ratios in a way that shows agreement between two independent velocity estimates: the instantaneous velocity estimates from Doppler dimming models and the average velocity estimates from multi-height observations of the plasma.

3.3.3 Constraints on Physical Properties

Confirming the precise details of the plasma's physical properties will require constraints from more than just the O VI ratio. Other spectral line ratios can act as useful diagnostics for various properties, including temperature, density, velocity, and ionization states. We present these observational constraints in Table 3.3. For reasons elaborated in §3.2.2, we only consider the ratios of the total intensities for the three composite clumps, instead of the many individual clumps. We conservatively assign uncertainties of 25%, 30%, 20%, 30%, and 30% for the $\frac{\text{H I 1216}}{\text{H I 1026}}$, $\frac{\text{H I 1216}}{\text{O VI 1032}}$, $\frac{\text{H I 1026}}{\text{O VI 1032}}$, $\frac{\text{O V 1218}}{\text{O VI 1032}}$, and $\frac{\text{C III 977}}{\text{O VI 1032}}$ ratios respectively which include uncertainties in model atomic rates, adopted solar disk emission line profiles, model scattering cross sections, and distinct UVCS calibrations for the primary and redundant optical paths.

Using distinct ratios as observational constraints carries distinct assumptions about the plasma cloud's environment. For example, multi-ion ratios like the $\frac{\text{H I 1216}}{\text{O VI 1032}}$ ratio, require the models to assume an isothermal plasma cloud mixed with H I ions and O VI ions. Such assumptions should be handled with care. Although Olsen et al. (1994) and Allen et al. (1998) suggested that the Lyman-α profile of the slow solar wind (from Olsen) and the fast solar wind (from Allen) acts as a good proxy for the free proton effective temperature, we do not assume this to be true for temperatures that are derived by intensity ratios that include Lyman-α emission.

3.4 Numerical Models for Heating Rates

The physical properties of the observed plasma give insight on the rate of heating experienced by the plasma. We determine these physical properties by modelling a parcel of plasma as it expands and travels radially away from the solar disk. We primarily monitor its thermal energy as we follow the

76
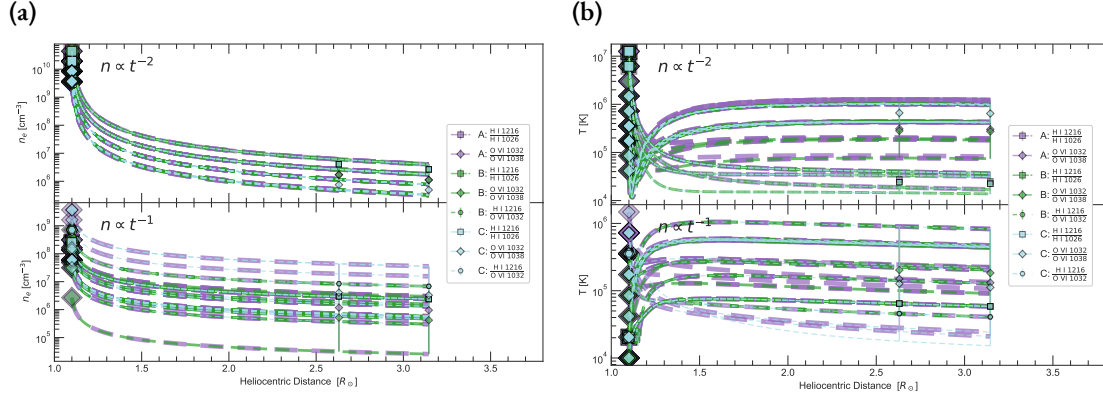
Figure 3.8: Resultant set of electron density and temperature profiles after using the Q_{KR} heating function where $\alpha_B = 2$. The square, diamond, and hexagon symbols located at 2.6 and 3.1 $R_\odot$ are arbitrarily positioned in the middle of their respective upper and lower limits for visual clarity. The vertical position of this symbol is not statistically more significant than other values within its range. **(a)** These model densities have corresponding temperatures, velocities, and ionization states that yield an intensity ratio congruent to the data. **(b)** These model temperatures have corresponding densities, velocities, and ionization states that yield an intensity ratio congruent to the data.

plasma with a Lagrangian approach and assume a self-similar expansion. We allow the total density n to monotonically decrease over a total time t and we describe this expansion rate with the power law

$$\frac{n_2}{n_1} = \left(\frac{t_2}{t_1}\right)^{-\alpha_t} \tag{3.4}$$

where the density n_1 at time t_1 changes to the density n_2 at time t_2 at a rate that corresponds to the expansion index α_t.

We model the expansion rate with an index of 3.0 (cubic), 2.0 (quadratic), or 1.0 (linear) to act as an approximation for the dimensionality of the plasma's expansion. The density is an observable quantity of the CME but the dimensionality of its expansion is unclear because observations of the three composite clumps do not provide much information about the CME's morphological properties. To minimize our geometric assumptions, only the density parameter is directly affected by our assumed expansion rate, $n \propto t^{-\alpha_t}$. However, the lack of morphological information can make the physical interpretation of α_t ambiguous. For example, it is possible for a plasma to undergo a 3D expansion at a rate of $n \propto r^{-2} \propto t^{-2}$ (i.e., α_t=2) under simplified conditions where a fluid experiences a steady state flow while its volume expands at a constant rate in each dimension. Potential discrepancies like this in dimensionality are exacerbated when considering that a filamentary structure

within a CME may be expanding in its long length faster than it expands in its short radius—thus, creating more ambiguity when defining a *single* rate of expansion for CMEs through a power law.

We use the expansion power law to drive one of our cooling terms for the plasma. Any decrease in thermal energy via expansion is represented by $dE = k_B \langle T/n \rangle dn$, where the quantity T/n is averaged over a given time interval and used to express our total thermal expansion as

$$E_{\delta n} = k_B T \frac{\delta n}{n} \quad \text{erg particle}^{-1}, \tag{3.5}$$

where T is temperature, δn is the change in density, and k_B is the Boltzmann constant. This is a portion of the thermal energy $k_B T$ that is converted into work that expands the gas. Due to the δn dependence, a cubic expansion rate would allow for a far greater cooling than a linear expansion rate.

The cooling is augmented by conversions of thermal energy into radiation that escapes the system. The radiative cooling is expressed as

$$P_{rad} = n_e n_{Z,z} \Lambda_{Z,z}(T) \quad \text{erg cm}^{-3} \text{ s}^{-1}, \tag{3.6}$$

where n_e is the free electron density (in units of cm^{-3}), $n_{Z,z}$ is the density for ion z of element Z, and $\Lambda_{Z,z}(T)$ is the cooling rate coefficient (in units of erg cm^3 s^{-1}) that accounts for the emission line and continuum processes that can occur at a given temperature for a given ion. We adopt the cooling rate coefficients computed by the CHIANTI atomic database (Dere et al., 1997, 2019).

We model these cooling mechanisms to reduce the thermal energy while an unknown heating mechanism augments the thermal energy by one of our five heating parameterizations. The first two are not motivated by any known physical mechanisms of a CME. One is proportional to the density of the plasma and the other is proportional to the square of the density. We characterize the former as $Q_n = C_H \cdot n$ and the latter as $Q_{n^2} = C_H \cdot n^2$, which each have a heating coefficient C_H. With the simple Q_n function, we can test the effects of homogeneously generating a constant rate of thermal energy within a CME. The utility of the Q_{n^2} is in its square-density dependence. We can gain insight on how the relatively high density environment near the solar surface may drastically affect the heating, and this would directly counteract the square-density dependent radiative cooling.

The third heating parameterization was adopted by Allen et al. (1998, 2000) to model the fast solar wind as the motion of neutral hydrogen, free protons, and free electrons are influenced by Alfvén waves. It is described as

$$Q_{AHH} = C_H \cdot e^{-\frac{r_a}{\mathcal{H}}} \quad \mathrm{erg\ cm^{-3}\ s^{-1}}, \tag{3.7}$$

where r_a is the altitude (equal to $r - 1.0 R_\odot$) and $\mathcal{H}$ is the scale height. We adopt 0.7 $R_\odot$ as our scale height to remain consistent with Allen et al. (1998), as this was one of two model scale heights they considered. Here, the heating rate coefficient, C_H, has units of $\mathrm{erg\ cm^{-3}\ s^{-1}}$. See also Withbroe (1988) and Lionello et al. (2009a) for additional implementations of this heating function.

Our last two parameterizations are expressed by one magnetic heating function. Just as we used a power law to express the dimensionality of our self-similar expansion, we also present a power law to express the dimensionality of this magnetic heating:

$$\begin{aligned} Q_{KR} &= C_{H,B_0} \left[\left(\frac{l}{r_{a,1}} \right)^{\alpha_B} - \left(\frac{l}{r_{a,2}} \right)^{\alpha_B} \right] \mathrm{erg\ cm^{-3}} \\ &= \frac{B_0^2}{8\pi} \left[\left(\frac{l}{r_{a,2} - \delta r_a} \right)^{\alpha_B} - \left(\frac{l}{r_{a,2}} \right)^{\alpha_B} \right], \end{aligned} \tag{3.8}$$

where the coefficient C_{H,B_0} is a constant magnetic pressure (in units of $\mathrm{erg\ cm^{-3}}$) that includes an initial magnetic field strength B_0. This magnetic field strength is mostly applicable to a CME's flux rope, for which we assign a characteristic length scale l and a magnetic expansion index α_B. We consider l to be 0.1 $R_\odot$, which is typical of a pre-CME flux rope; and, we consider α_B to be either 3.0 or 2.0, which represents a 3D or 2D expansion of the flux rope. We test both choices of α_B and distinguish each choice as its own heating parameterization. We use α_B to parameterize the unknown morphological properties of the magnetic flux rope. Such properties could influence δr_a: the plasma's change in altitude ($r_{a,2} - r_{a,1}$) within a characteristic timescale while traveling between the two altitudes at some average, bulk speed within the corona.

This magnetic heating function is inspired by the Kumar & Rust (1996) model for heating when the magnetic helicity is conserved (Taylor, 1974; Berger & Field, 1984) in a self-similarly expanding

flux rope. They analytically perform a dimensional analysis of magnetic helicity and suggest that it can follow the form $H_m \sim constant \sim l \cdot \int B^2 dV$, where l is some characteristic length scale and B^2 is the magnetic energy that must decrease as the volume increases. In their model, a portion of the free magnetic energy is gradually converted to thermal energy as the flux rope extends to higher heights in the corona. We mimic this by using a fraction (given as the total quantity in square brackets) of the magnetic energy to consistently heat the parcel of plasma. The nature of our specific Q_{KR} function's magnetic heating is useful but it is not meant to explain any specific properties of the CME's (unobserved) flux rope. Without knowing the morphology of the observed CME, we do not attempt to deduce the properties of its flux rope within this paper.
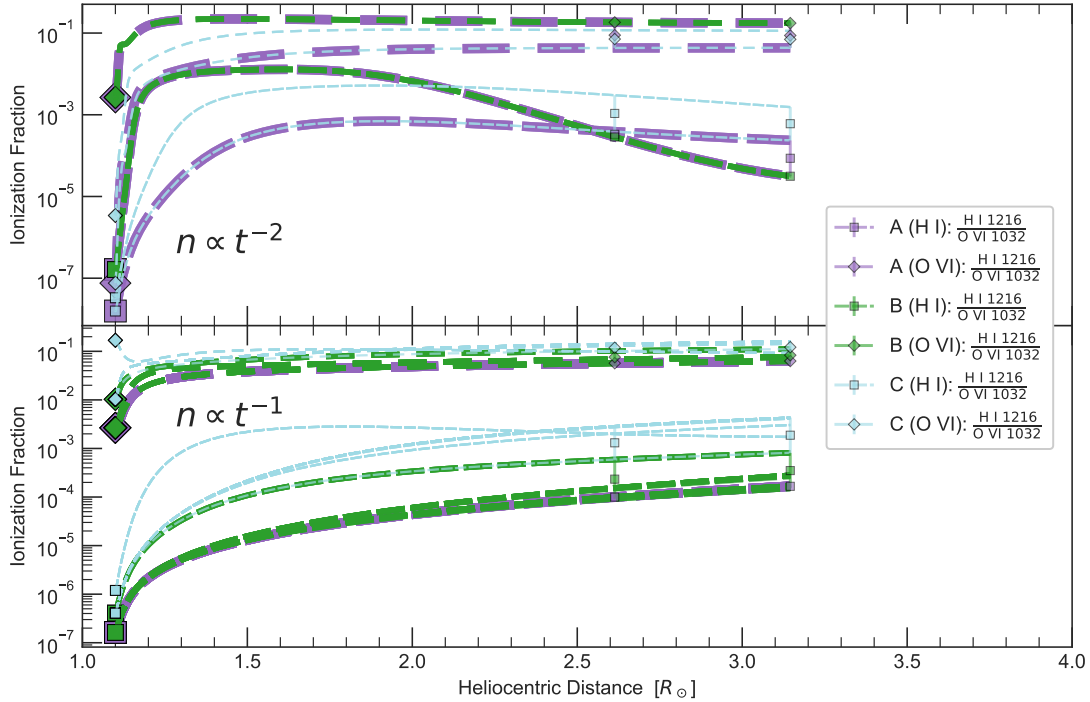
Figure 3.9: Resultant set of ionization fraction profiles after using the Q_{AHH} heating function and constraints from only the $\frac{\mathrm{H\,I\,1216}}{\mathrm{O\,VI\,1032}}$ ratio.

3.4.1 INITIAL AND FINAL PHYSICAL CONDITIONS

Our numerical modelling procedure yields the physical conditions of the plasma as a function of time and height in the corona. We have the two cooling terms counteract one of the five heating

parameterizations in order to change the internal thermal energy of the parcel of plasma: $dU = \frac{3}{2} n k_B dT$.

We start by establishing a grid of initial conditions and allow each cell (or model) of the grid to evolve until the heights of clumps A, B, and C are reached. The initial conditions we consider include densities of $\log(n_0/\mathrm{cm}^{-3}) \in [6.0, 12.0]$ and temperatures of $\log(T_0/\mathrm{K}) \in [4.0, 7.1]$ experienced by a plasma cloud in ionization equilibrium at $r = 1.1\,R_\odot$. The range of heating rate constants (C_H) we consider varies from one heating function to another. Our initial conditions also include coronal elemental abundances from Feldman et al. (1992) and ion populations in ionization equilibrium from the CHIANTI database.

After initiation, we reject models with temperatures that evolve beyond our temperature ceiling of 10^8 K or below our temperature floor of 10^4 K. Once the heights of our observed clumps are reached, we use each model's instantaneous temperature, density, and velocity to determine the emissivities and intensity ratios for the spectral lines observed by UVCS. At these heights, each model must meet the observational constraints established by the multi-height velocity limits, the LOS length limits, and the intensity ratio limits. We assign each model a range of instantaneous velocities that lie within the multi-height velocity limits: $200 \leq v\,/\,\mathrm{km\,s}^{-1} \leq 300$. When compared to the observed intensity of an emission line, the model's emissivities (derived from the model's temperature, density, and velocity) must yield an estimate for the clump's LOS length that is similar to the clump's POS size. Subsequently, the model's emissivities for a pair of emission lines must yield an intensity ratio that agrees with observations. Each cell-model within our grid that meets these criteria is included in our final evaluation of the energy budget. The model's cumulative heating (specific) energy, HE_C, is compared to the sum of the kinetic (specific) energy, $\frac{1}{2}v^2$, and the gravitational potential (specific) energy, $GM_\odot(1/1.1R_\odot - 1/r)$. The cumulative heating energy is the sum of the model's initial thermal energy and continuous production of thermal energy via the heating function. Thus, each model will have a lower cumulative heating at the lower height of $r = 2.6\,R_\odot$ than at $3.1\,R_\odot$. This 1D numerical modelling procedure is a variation of the methods utilized by other UVCS CME heating analyses (Akmal et al., 2001; Ciaravella et al., 2001; Lee et al., 2009; Landi et al., 2010; Murphy et al., 2011).
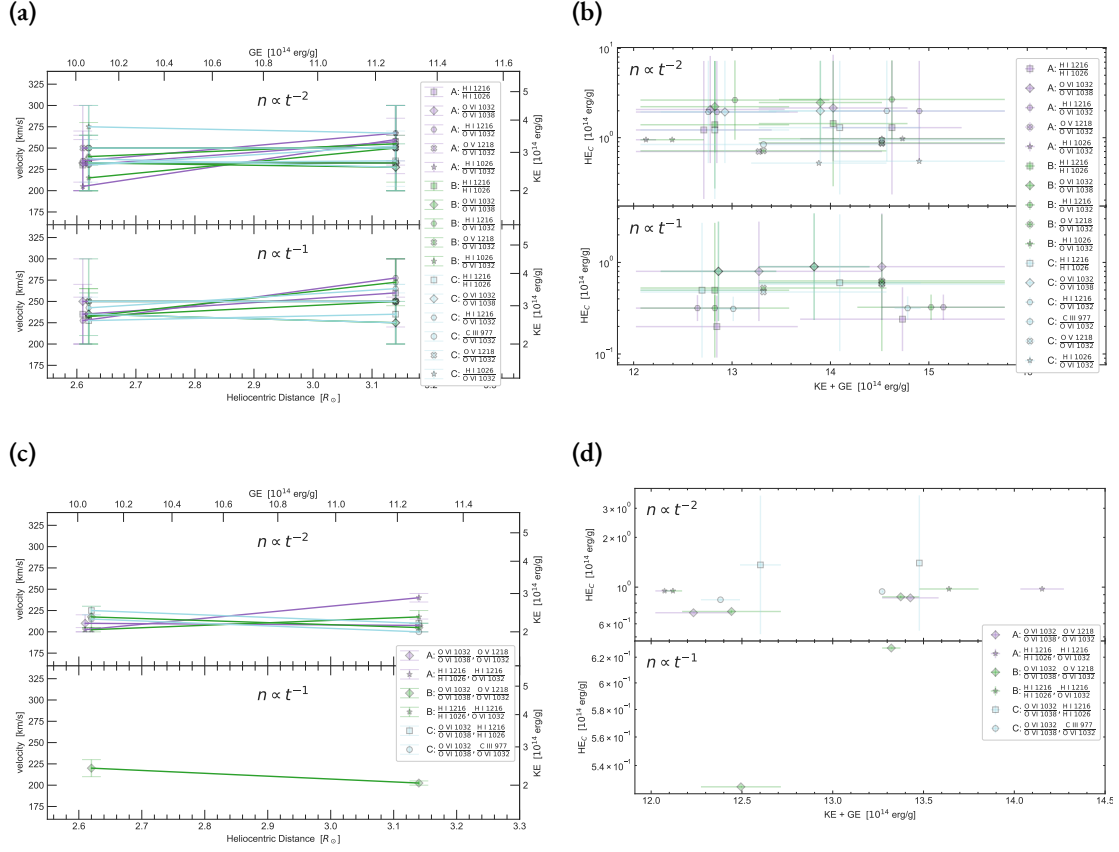
Figure 3.10: Observationally constrained models using the Q_n heating parameterization. Each symbol (i.e., each combination of color and shape) appears twice to represent each clump's observation at two distinct coronal heights, which each indicates a gravitational potential energy. This is the potential energy overcome by the CME core as it travels from the solar surface to an observation site. **(a,c)** The kinetic energy and gravitational potential energy are given. **(b,d)** The cumulative heating energy is given. The horizontal error bars derive directly from the range of model kinetic energies deduced by the constrained model velocities.

3.4.2 NON-EQUILIBRIUM IONIZATION CODE

In our procedure, the evolving ionization states directly affect each model's emissivities, intensity ratios, and radiative cooling. The initial condition for each model requires that the plasma environment changes temperature on a timescale that is long enough to allow the ions' rate of ionization to balance the rate of recombination. Within this thermodynamic timescale, the population of ionization states is independent of time and can be determined as a function of temperature. This assumption of ionization equilibrium does not hold when astrophysical phenomena compel a plasma's thermodynamic state to change more rapidly than the ionization rate or the recombination
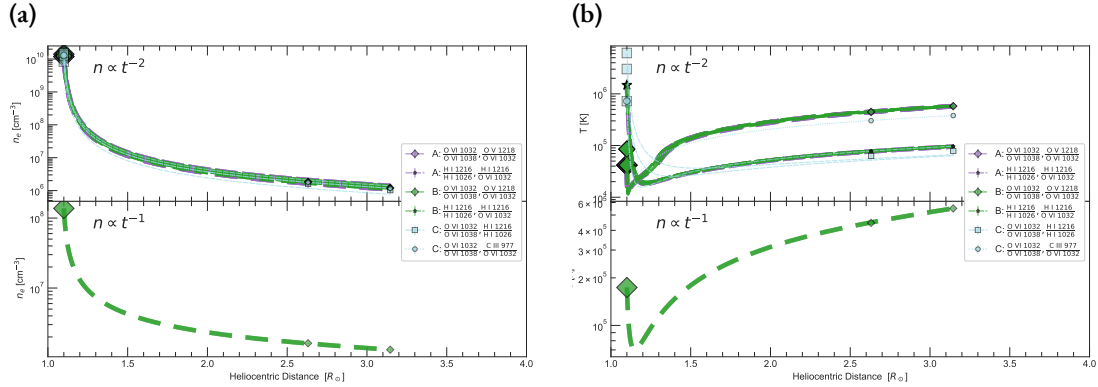
Figure 3.11: Tight constraints on evolution of physical conditions after using various double-ratio analyses (for the Q_n heating parameterization).

rate.

The ionization and recombination rates are affected by the environment's density and, even more so, the temperature. As an example, the low-density regions distant from the dense solar surface can suppress a plasma's ability to ionize or recombine despite experiencing hot coronal temperatures. Also, a high-speed solar wind affecting those regions can transfer the plasma quickly to other regions within timescales that are too short for the ionization and recombination processes to balance out. Such scenarios might occur on timescales that observations do not temporally resolve; therefore, meticulous care should be taken by accounting for a net change in the population of ionization states that is predominantly due to recombination processes or predominantly due to ionization processes (e.g., Raymond, 1990; Rakowski et al., 2007; Ko et al., 2010; Bradshaw & Klimchuk, 2011; Gruesbeck et al., 2011, 2012; Landi et al., 2012; Rivera et al., 2019a). If unknown mechanisms heat the plasma quickly while the ionization rate is much slower, an ionization equilibrium assumption for the observed ionization states would understimate the temperature. Conversely, if the plasma is quickly cooled and observations of its ionization states are taken before slow recombination processes occur, the ionization equilibrium assumption would overestimate the temperature.

In such cases, the non-equilibrium ionization states can be determined through the formula

$$
\begin{aligned}
\frac{dn_z}{dt} = {} & n_e n_{z-1} q_i(Z, z-1, T) \\
& - n_e n_z \big[q_i(Z, z, T) + \alpha_r(Z, z, T) \big] \\
& + n_e n_{z+1} \alpha_r(Z, z+1, T),
\end{aligned}
\tag{3.9}
$$

where q_i is the ionization rate coefficient and α_r is the recombination rate coefficient. This formula is incorporated into the ionization code developed by Shen et al. (2015). Originally written in FOR-TRAN[*], we use its PYTHON[†] counterpart.

The ionization code solves the time-dependent equations for a parcel of gas traveling in a La-grangian framework, in which the temporal evolution history of plasma density and temperature can be obtained. The code pre-calculated all q_i and α_r values at a grid of temperatures and saved them into structured tables based on the atomic database Chianti v9 (Dere et al., 2019). The calcu-lations are then analytically simplified with the Eigenvalue method described by Masai (1984) and Hughes & Helfand (1985) for a given temperature. To maintain temporal efficiency in the enor-mous computations, we apply an adaptive time step strategy (see Shen et al. (2015) for details), and load only the tables during the simulation. We obtain these calculations for all ionization states of ten elements: H, He, C, N, O, Ne, Mg, Si, S, and Fe. We use the resulting ionization fractions to compute $n_{Z,z}$ for the emissivity described by Equation 3.1 as well as the rate of radiative cooling described by Equation 3.6.

3.5 MHD Model from MAS Simulation

With our 1D numerical models, we can determine the physical properties of the plasma observed at two heights in the corona. The historical evolution of the plasma's physical properties can be ap-proximately evaluated as well; but, unfortunately, such a modelled evolution does not have spectra below 2.6 $R_\odot$ to act as a constraint on the evolving parameters. This would have provided more in-

---

[*]https://github.com/ionizationcalc/time_dependent_fortran
[†]https://github.com/PlasmaPy/PlasmaPy-NEI

sight on how the CME heating begins near the solar surface and continues to evolve throughout the corona.

The historical evolution of a CME's physical properties can show how one of our heating parameterizations might be better than another heating parameterization at realistically mimicking the effects of the true CME heating mechanisms that are still unknown. Therefore, we compare parameterizations by using a realistic 3D MHD model that provides the historical evolution of a simulated CME with similar properties to the one that we observe. This simulation is a product of the Magnetohydrodynamic Algorithm outside a Sphere (MAS) code.

MAS models the global solar atmosphere from the top of the chromosphere to Earth and beyond, and it has been used extensively to study coronal structure (Mikić et al., 1999; Linker et al., 1999; Lionello et al., 2009b; Downs et al., 2013; Mikić et al., 2018), coronal dynamics (Lionello et al., 2005, 2006; Linker et al., 2011) and CMEs (Linker et al., 2003; Lionello et al., 2013; Török et al., 2018; Reeves et al., 2010, 2019). MAS solves the resistive, thermodynamic MHD equations in spherical coordinates (r, θ, φ) on structured nonuniform meshes. Magnetosonic waves are treated semi-implicitly, allowing us to use large time steps for the efficient computation of long-time evolution. A simplified radial magnetic field based on observational measurements is used as the primary boundary condition. To drive the magnetic field evolution in MAS, the radial component of the magnetic field at the boundary can be evolved using a technique similar to that described by Lionello et al. (2013).

The present version of MAS employs a sophisticated thermodynamic MHD approach, where additional terms that describe energy flow in the corona and solar wind are included (coronal heating, parallel thermal conduction, radiative loss, and Alfvén wave acceleration; as fully described in Appendix A of Török et al., 2018). This treatment is essential for capturing the thermal-magnetic state of the corona and solar wind, enabling the direct comparison of a variety of forward modelled observables to real observations.

A non-equilibrium ionization module to advance the fractional charge states of minor ions according to the model of Shen et al. (2015) was recently incorporated into MAS. The implementation is very similar to that of Lionello et al. (2019) for a 1D solar wind code.

3.6 Results and Discussion

The composite clumps seen at the highest coronal heights observed, 2.6 and 3.1 $R_\odot$, are the only clumps for which we can confidently deduce two independent estimates of the velocity. The first is a multi-height, average velocity estimate that comes from the data analysis described in §3.2.3. The second is an instantaneous velocity estimate from O VI radiative pumping analytics of the 1038 Å line as described in §3.3.1. Both estimates provide upper and lower limits for the velocity that are further constrained by the uncertainties we assigned to the intensity ratios in Table 3.3. Additionally, as described in §3.3, any of our intensity ratios can serve as a diagnostic for velocity when the resonant scattering components are comparable to the collisional components. This is common for the $\frac{\text{H I } 1216}{\text{O VI } 1032}$ ratio.

We focus on the three composite clumps emphasized in Figures 3.4 and 3.5. The final results presented in this section suggest that all three clumps have experienced similar conditions. After our grid of model initial conditions evolves and reaches the clumps' respective coronal heights, a range of model velocities, densities, temperatures, and ionization states is deduced for each clump. Subsequently, we determine the historical profile of each clump from their respective models. According to the profiles we derive, the physical parameters determined at 2.6 $R_\odot$ are within an order of magnitude of the parameters determined at 3.1 $R_\odot$ for our three clumps. For this reason, we report the physical conditions as roughly the same for both heights in the corona.

Although the model parameters vary as a function of height, there are general characteristics of the historical profiles for density, temperature, and ionization states that are similar in all cases regardless of the heating function or expansion rate that we use. For example, in each case, our assumption of a simple self-similar expansion (expressed in the form of Equation 3.4) requires that the density profiles for ions and free electrons monotonically decrease. An example of these observationally constrained density profiles is given in Figure 3.8a.

For temperature profiles, the minor details vary case by case; but, there are three general trends. Examples of these three general trends can be seen in Figure 3.8b. When visualized on a logarithmic scale, the trends can be described as the following:

[1] The temperature profile begins by decreasing exponentially until it starts to plateau within 1.4 $R_\odot$, which suggests the cooling is substantially greater than the heating immediately after the eruption but balances out later.

[2] The opposite occurs. The temperature begins with an increase and continues in a logarithmic fashion until it starts to plateau within 1.4 $R_\odot$, which indicates a heating that is consistently greater than the cooling by a margin that is gradually decreasing over time.

[3] The temperature profile exponentially decays until it reaches an inflection point within 1.4 $R_\odot$, where it then gradually increases. This occurs when the heating is quickly increasing but is temporarily dominated by the cooling immediately after eruption.

We refer to general trend **[1]** as *D-F* since its curve initially decreases but later begins to flatten out within 1.4 $R_\odot$. We refer to general trend **[2]** as *I-F* since its curve initially increases but later flattens out. Lastly, we refer to general trend **[3]** as *D-I* since its curve initially decreases but later increases.

As for the evolution of ionization states, the ionization fraction profiles are not tightly constrained when using only the $\frac{\text{O VI 1032}}{\text{O VI 1038}}$ ratio. These profiles are heterogeneous and their corresponding broad range of temperature profiles are just as heterogeneous. In this context, the heterogeneity is clear when temperature profiles are not limited to a specific general trend: the *D-F*, *I-F*, or *D-I* trend. When we use the $\frac{\text{H I 1216}}{\text{O VI 1032}}$ ratio or the $\frac{\text{H I 1216}}{\text{H I 1026}}$ ratio, there is a strong anti-correlation between the H I ionization fraction profiles and their corresponding temperature profiles. This is one of the reasons why the *D-F* trend is so prevalent for all three clumps regardless of heating function and expansion rate. An example of our ionization fraction profiles is given by Figure 3.9. The cooling must be significantly greater than the heating until the temperature is low enough to yield a significant amount of H I at the clumps' respective coronal heights (cf. T_m in Table 3.2). This is why relatively high temperatures, around 10^6 or 10^7 K, are the inferred initial temperatures for many of the H I models, which often evolve to a temperature of about 10^5 K at the final two observed coronal heights. For the $\frac{\text{H I 1216}}{\text{O VI 1032}}$ ratio, the strong temperature constraints on the ionization state of H I always narrow the range of model temperatures permitted by O VI.

The multi-ion ratios provide diagnostics that are sensitive to ionization states. Our results con-

sistently indicate that the single-ion $\frac{\text{O VI 1032}}{\text{O VI 1038}}$ ratio and single-ion $\frac{\text{H I 1216}}{\text{H I 1026}}$ ratio yield a broader range of physical conditions than the constraints of the multi-ion $\frac{\text{H I 1216}}{\text{O VI 1032}}$ ratio. When we use the mulit-ion $\frac{\text{C III 977}}{\text{O VI 1032}}$ ratio and assume C III ions share the same temperature, density, and velocity as O VI ions, there is very little agreement with observations. Only the Q_n heating function shows any agreement at the two observed coronal heights but only for clump C. This lack of agreement suggests that our assumption that C III experiences the same conditions as O VI is not plausible for our three observed clumps. Using the $\frac{\text{O V 1218}}{\text{O VI 1032}}$ ratio and assuming O V shares the same conditions as O VI yields models that show more agreement with observations than did the $\frac{\text{C III 977}}{\text{O VI 1032}}$ ratio. However, this agreement is seen only when assuming the Q_n heating.

Regardless of the intensity ratio used, our analysis is done using three self-similar expansion indices (α_t) distinctly. None of our calculations using a cubic ($\alpha_t=3$) self-similar expansion rate resulted in models that agreed with the observational constraints of clumps A, B, or C. The model densities drop off excessively between the beginning of its evolution near the solar surface and the end of its evolution near 2.6 and 3.1 $R_\odot$. At these observed coronal heights, our model electron densities (which contribute to the radiation's collisional component) and our model ion densities (which contribute to both components of radiation) are too low to explain the clumps' observed intensities and POS sizes. For the few models that do yield plausible densities, there is either far too much heating or far too much cooling at the beginning of the models' corresponding temperature profiles. As a result, this excessive change in thermal energy along with our aforementioned LOS length constraint (cf. Equation 3.3) have ruled out all models that utilize a cubic self-similar expansion rate for our three clumps at 2.6 and 3.1 $R_\odot$. For this reason, we discuss results that come from only two of our self-similar expansion rates.

In the case of Q_{n^2}, only the linear expansion rate models have results that agree with the observations. The other four heating parameterizations yield results for both the quadratic and linear expansion rates. For a given expansion rate, all heating parameterizations suggest similar physical conditions for the observed clumps and similar energy budgets. Therefore, we detail the results in this section only for the Q_n parameterization and we elaborate on the results of the other heating parameterizations in §3.8.1, §3.8.2, and §3.8.3.

3.6.1 Density proportional heating

Using the Q_n heating, there are five distinct plasma clouds modelled that agree with the observations: H I, O VI, H I mixed with O VI, O V mixed with O VI, and (for only the quadratic expansion rate models) C III mixed with O VI. The H I dominant material is modelled through the $\frac{\text{H I 1216}}{\text{H I 1026}}$ ratio. The H I and O VI mixture is modelled through the $\frac{\text{H I 1216}}{\text{O VI 1032}}$ ratio or the $\frac{\text{H I 1026}}{\text{O VI 1032}}$ ratio. The O VI dominant material is modelled through the $\frac{\text{O VI 1032}}{\text{O VI 1038}}$ ratio. The O V and O VI mixture is modelled through the $\frac{\text{O V 1218}}{\text{O VI 1032}}$ ratio. The C III with O VI mixture is modelled through the $\frac{\text{C III 977}}{\text{O VI 1032}}$ ratio. For all three clumps, we find models that agree with each of these ratios, except for the $\frac{\text{C III 977}}{\text{O VI 1032}}$ ratio. There is only a very tiny region in parameter space where our models can agree with the C III observations and that agreement is only found for clump C.

We estimate the kinetic energy and gravitational potential energy of the three composite clumps, as illustrated by Figures 3.10a and 3.10c. Note that the vertical position of each symbol within its respective error bar is not statistically more significant than the other velocity values within range of its error bar. Each symbol is placed in the middle of its range of values for visual clarity. In Figure 3.10a, the O VI dominant material (plotted with diamond symbols) has the slowest velocity estimates at the height of 3.1 $R_\odot$. The H I with O VI mixture (via the $\frac{\text{H I 1216}}{\text{O VI 1032}}$ ratio models marked by hexagons) tends to have the fastest velocities at that height. Figures 3.10c and 3.10d show how for the linear expansion rate there is only one double-ratio set ($\frac{\text{O VI 1032}}{\text{O VI 1038}}$ with $\frac{\text{O V 1218}}{\text{O VI 1032}}$) that has models agreeing with observations. Overall, the double-ratio models for both expansion rates are better constrained and suggest slower velocities than the single-ratio models.

Figures 3.10b and 3.10d summarize the cumulative heating energy amongst all models for the three clumps. The vertical upper and lower limits correspond to a constrained range of temperature profiles. The horizontal upper and lower limits correspond to a constrained range of kinetic energies. Each symbol is placed in the middle (vertically and horizontally) of its range of values merely for visual clarity, and each symbol appears twice to represent each clump's observation at two coronal heights. The cumulative heating at the higher height is, by default, always slightly greater than at the lower height since we assume the CME's heating is continuous between observations. These

results derive from heating rate coefficients in range of $\log(C_H/\text{erg s}^{-1}) \in$ [-15.0, -12.6] for both the quadratic expansion rate models and the linear expansion rate models. The quadratic expansion rate models suggest cumulative heating energies in range of $10^{13.31-14.93}$ erg g^{-1}. The linear expansion rate suggests $10^{12.96-14.54}$ erg g^{-1}. Thus, our energy budget for this CME, assuming the Q_n heating, suggests that the cumulative heating energy is similar to the $\sim 10^{14}$ erg g^{-1} kinetic energy.

We now present a few examples of how the CME heating rates and energy budget may be deduced from observations of a single intensity ratio. Amongst all of the ratios that we use, we find that the three most informative results came from using the $\frac{\text{H I 1216}}{\text{H I 1026}}$ ratio, the $\frac{\text{O VI 1032}}{\text{O VI 1038}}$ ratio, and the $\frac{\text{H I 1216}}{\text{O VI 1032}}$ ratio.

$\frac{\text{H I 1216}}{\text{H I 1026}}$ RATIO ANALYSIS

All three clumps in the case of both expansion rates have velocities from 200 to 270 km s^{-1} at 2.6 $R_\odot$. At 3.1 $R_\odot$, the velocities are in the range 200–285 km s^{-1} for the quadratic expansion rate and 200–300 km s^{-1} for the linear expansion rate. The temperature profiles exhibit the general trends *D-F*, *I-F*, and *D-I*. Along both 2.6 and 3.1 $R_\odot$, the temperatures range from 1×10^4 to 1×10^5 K for the quadratic expansion rate case. In the linear expansion rate case, the temperature range is from 2×10^4 to 4×10^6 K. The million Kelvin temperatures are reached here via the *I-F* trend, which only appears for the linear expansion rate. Such hot temperatures are responsible for broadening the resonant scattering line profiles sufficiently to allow a broad range of models that pertain to relatively slow velocities near 200 km s^{-1} and relatively fast velocities near 300 km s^{-1}. (The cooler temperatures favor a narrower range of velocities that are near 200 km s^{-1} by narrowing the scattering line profiles.) The hottest model temperatures also coincide with the lowest H I ionization fractions while the coldest temperatures yield the highest ionization fractions. The temperature profiles firmly anti-correlate with the ionization fraction profiles. This is partially due to our lower limits in temperature coinciding with the H I ion's peak formation temperature (under ionization equilibrium), $T_m \sim 3 \times 10^4$ K. The density range is from 1×10^5 to 6×10^6 cm^{-3} for the quadratic expansion rate and 9×10^4 to 4×10^6 cm^{-3} for linear expansion rate. Lastly, the range of plausible initial conditions are as follows: $n_{e,0} = 10^{9.21-10.64}$ cm^{-3}, $T_{e,0} = 10^{5.24-7.10}$ K, and $\log(C_H$

/ erg s^{-1}) $\in$ [-15.0, -14.0] for the quadratic expansion rate; as well as, $n_{e,0} = 10^{6.97-8.50}$ cm^{-3}, $T_{e,0} = 10^{4.00-5.86}$ K, and log(C_H / erg s^{-1}) $\in$ [-15.0, -12.6] for the linear expansion rate.

In the case of our linear expansion rate, the models that follow the *I-F* trend and produce the million Kelvin temperatures are derived from the lowest initial temperature ($T_{e,0} = 10^4$ K) and greatest heating rate ($C_H = 10^{-12.6}$ erg s^{-1}) in our observationally constrained models. This anti-correlation between the minimum initial temperature and maximum heating rate only agrees with our $\frac{\text{H I 1216}}{\text{H I 1026}}$ ratio constraints when the *I-F* trend is followed. Under both expansion rates, the models that follow the general trends *D-F* and *D-I* do not correspond to this minimum initial temperature nor this maximum heating rate.

$\frac{\text{O VI 1032}}{\text{O VI 1038}}$ RATIO ANALYSIS

The velocities are similar at both heights for each expansion rate: 200–265 km s^{-1} for the quadratic expansion rate and 200–300 km s^{-1} for the linear expansion rate. Most of the models suggest velocities $\leq$ 225 km s^{-1} due to the radiative pumping. Compared to the collisional component, the radiative pumping effect must have increased at 3.1 $R_\odot$ because the observed $\frac{\text{O VI 1032}}{\text{O VI 1038}}$ intensity ratios are consistently lower at 3.1 $R_\odot$ than at 2.6 $R_\odot$ (cf. Table 3.3). The velocity of the O VI material has the most influence on the strength of the radiative pumping. Therefore, velocities that are closer to the speed of peak radiative pumping at ~180 km s^{-1} (due to the C II 1037 Å solar disk emission) can produce lower intensity ratios. This velocity diagnostic becomes plagued by degeneracies as the intensity ratios get closer to 2.0. Consequently, although it is reasonable to expect faster velocities at 2.6 $R_\odot$ due to its higher intensity ratios (cf. Table 3.3), our resultant models do not clearly indicate that. The intensity ratios can be affected by the lower ambient temperature and density at greater heights in the corona.

The faster velocities are only plausible in special cases where there is a balance between million-Kelvin temperatures and low densities that are less than 10^5 cm^{-3}. The hot temperatures broaden the line profiles and allow the radiative pumping to be in effect for a broader range of velocities, including velocities greater than ~250 km s^{-1}. The velocities between 250 and 300 km s^{-1} imply that the 1038 Å line profile shifts away from the peak of the C II 1037 Å line profile and thus weak-

ens the radiative pumping; but, without the thermally broadened line profile there would be no radiative pumping near 250 km s^{-1} at all. The low densities balance the ratio by diminishing the square-density dependent collisional component of the 1032 Å line much more than the density dependent resonant scattering component of the 1038 Å line that is being (weakly) pumped. Thus, the $\frac{\text{O VI 1032}}{\text{O VI 1038}}$ intensity ratio can remain below 2.0 in spite of the relatively weak radiative pumping at velocities between 250 and 300 km s^{-1}. The degeneracies that justify these relatively fast velocities are mitigated when constraints from multiple ratios are simultaneously imposed on our models. As a result, the double-ratio models that include the $\frac{\text{O VI 1032}}{\text{O VI 1038}}$ ratio consistently suggest relatively slow velocities (i.e., $200 \leq v/$ km s$^{-1} \leq 225$).

The temperature profiles exhibit the general trends *D-F*, *I-F*, and *D-I*. Along both 2.6 and 3.1 $R_\odot$, the temperatures range from 3×10^4 to 3×10^6 K for the quadratic expansion rate and from 2×10^4 to 4×10^6 K for the linear expansion rate. The density range is from 1×10^4 to 6×10^6 cm^{-3} for the quadratic expansion rate and from 3×10^4 to 4×10^7 cm^{-3} for the linear expansion rate. These wide ranges of resultant physical parameters increase the chance that another single-ratio model will overlap. Such overlap exhibited from double-ratio models will briefly be discussed later in this section. Lastly, the range of plausible initial conditions are as follows: $n_{e,0} = 10^{8.22-10.64}$ cm^{-3}, $T_{e,0} = 10^{4.00-7.10}$ K, and $\log(C_H /$ erg s$^{-1}) \in$ [-14.6, -12.6] for the quadratic expansion rate; as well as, $n_{e,0} = 10^{6.43-9.57}$ cm^{-3}, $T_{e,0} = 10^{4.00-6.48}$ K, and $\log(C_H /$ erg s$^{-1}) \in$ [-15.0, -12.6] for the linear expansion rate.

$\frac{\text{H I 1216}}{\text{O VI 1032}}$ RATIO ANALYSIS

For both expansion rates, many of the models require that the instantaneous velocity estimates increase between the heights 2.6 and 3.1 $R_\odot$. Some models suggest no acceleration while others can be as high as 70 m s^{-2}. The acceleration of our models is due to this ratio's significant drop between the two coronal heights (cf. Table 3.3), which occurs for all three clumps. Many of our models attribute the drop to a decrease in H I Lyman-α emission (as opposed to an increase in O VI 1032 Å emission). This implies that the resonant scattering component could have dropped substantially, which gives leeway for a greater change in velocity. Some models however account for the drop in

the intensity ratio by permitting the velocity to remain the same while the population of H I ions decreases substantially.

The temperature profiles only follow the *D-F* trend. The corresponding H I ionization fraction profiles anti-correlate with the temperature profiles. The corresponding O VI ionization profiles do not correlate with temperature; but, for this ratio analysis, almost all of the models suggest O VI ionization state becomes frozen-in before 1.5 $R_\odot$, and the O VI remains at its ionization fraction of ~5% onward through 2.6 and 3.1 $R_\odot$. Along both 2.6 and 3.1 $R_\odot$, the temperatures are from 4×10^4 to 1×10^5 K for the quadratic expansion rate and from 3×10^4 to 6×10^4 K for the linear expansion rate. This narrow range of upper and lower limit temperatures is due to the need for the presence of multiple ions (in this case H I and O VI). The density ranges from 8×10^5 to 1×10^7 cm^{-3} for the quadratic expansion rate and from 3×10^6 to 8×10^6 cm^{-3} for linear expansion rate. The densities are just as well-constrained as the temperatures due to the strong trade-off between density and temperature, which are both responsible for producing the emissivities that are necessary to match with the observed intensity ratios. Lastly, the range of plausible initial conditions are as follows: $n_{e,0} = 10^{9.93-11.00}$ cm^{-3}, $T_{e,0} = 10^{5.86-7.10}$ K, and $\log(C_H / \mathrm{erg\ s^{-1}}) \in$ [-14.4, -13.8] for the quadratic expansion rate; as well as, $n_{e,0} = 10^{8.50-8.85}$ cm^{-3}, $T_{e,0} = 10^{5.55-5.86}$ K, and $\log(C_H / \mathrm{erg\ s^{-1}}) \in$ [-15.0, -14.6] for the linear expansion rate.

COMMON TRAITS IN RATIO ANALYSES

As demonstrated, a single intensity ratio can provide a unique analysis to confirm the physical conditions of the observed CME, and this in turn constrains the initial conditions after eruption. In addition to the three ratios discussed in detail, we also find models that agree with the observational constraints of the following ratios: $\frac{\mathrm{H\ I\ 1026}}{\mathrm{O\ VI\ 1032}}$, $\frac{\mathrm{O\ V\ 1218}}{\mathrm{O\ VI\ 1032}}$, and $\frac{\mathrm{C\ III\ 977}}{\mathrm{O\ VI\ 1032}}$. Within the observational constraints, we find that some models work well to simultaneously explain multiple, observed intensity ratios: $\frac{\mathrm{O\ VI\ 1032}}{\mathrm{O\ VI\ 1038}}$ with $\frac{\mathrm{H\ I\ 1216}}{\mathrm{H\ I\ 1026}}$, $\frac{\mathrm{O\ VI\ 1032}}{\mathrm{O\ VI\ 1038}}$ with $\frac{\mathrm{H\ I\ 1216}}{\mathrm{O\ VI\ 1032}}$, $\frac{\mathrm{O\ VI\ 1032}}{\mathrm{O\ VI\ 1038}}$ with $\frac{\mathrm{H\ I\ 1026}}{\mathrm{O\ VI\ 1032}}$, $\frac{\mathrm{H\ I\ 1216}}{\mathrm{H\ I\ 1026}}$ with $\frac{\mathrm{H\ I\ 1216}}{\mathrm{O\ VI\ 1032}}$, $\frac{\mathrm{O\ VI\ 1032}}{\mathrm{O\ VI\ 1038}}$ with $\frac{\mathrm{O\ V\ 1218}}{\mathrm{O\ VI\ 1032}}$, and $\frac{\mathrm{O\ VI\ 1032}}{\mathrm{O\ VI\ 1038}}$ with $\frac{\mathrm{C\ III\ 977}}{\mathrm{O\ VI\ 1032}}$. Across all of the ratio or ratio-pair analyses we performed, the substantial agreement with observations of various spectral lines is partly due to the simplicity of the Q_n heating. This heating parameterization allows our models to sample

parameter space very well and thus account for many distinct characteristics that might explain our CME's evolution.

Due to the already tight limits on the physical conditions deriving from each multi-ion ratio, we do not find any models that agree simultaneously with two distinct multi-ion ratios (e.g., $\frac{\text{H I } 1216}{\text{O VI } 1032}$ with $\frac{\text{H I } 1026}{\text{O VI } 1032}$). We also note that there are no models that agree with any group of three ratios simultaneously at both of the final observation heights. This likely could have been accomplished if we used a third single-ion ratio, such as the density-sensitive ratios of $\frac{\text{O V } 1214}{\text{O V } 1218}$ and $\frac{\text{N III } 992}{\text{N III } 999}$. Due to their ionization-sensitive nature, each multi-ion ratio has a tendency to single-handedly tighten the limits on model parameters so severely that another multi-ion ratio is unlikely to match. Regardless of each unique ratio or ratio-pair analysis, there are similarities in the deduced physical properties and energetics: velocity, temperature, density, expansion, and heating.

Velocity: With respect to velocity, commonality can be seen in how the only (two) single-ion ratios that we use are typically the ratios that yield the slowest, instantaneous velocity estimates at 3.1 $R_\odot$. This is seen primarily by clumps *B* and *C* regardless of the expansion rate assumed.

Temperature: With respect to temperature evolution, the temperature profiles that follow the *D-F* trend typically yield the coolest temperature estimates at the 2.6 and 3.1 $R_\odot$ while the profiles exhibiting the *I-F* trend often yield the hottest temperatures. The inverse is true for the initial temperatures: hottest initial temperatures often correspond to the *D-F* trend and coolest initial temperatures often correspond to the *I-F* trend.

We cannot definitively confirm that the observed material is predominantly hot coronal gas that has been cooled or predominantly cool prominence gas that has been heated. In fact, our relatively broad but constrained range of plausible initial conditions suggests that we likely observed both types of CME material.

When considering plasma clouds that consist of H I, we find that a quadratic expansion rate limits the physical conditions sufficiently for there to be only one plausible explanation: a gradually cooled coronal gas tangled with the CME is predominantly the type of material we observed through the Lyman-α and Lyman-β lines. The linear expansion rate however leads to more uncertainty in the models' physical conditions and thus more possible explanations.

Akmal et al. (2001) conducted a UVCS CME heating analysis where they found plasma clouds in the core that were somewhat separated by temperature. In their observations, cool C III emission was evident in a small region interior to the hotter O V and O VI emission seen surrounding that small region. It is likely that we are also observing temperature-stratified or ion-stratified behavior along the POS and LOS of our CME's core material. Distinct regions along the LOS may be responsible for the distinct physical conditions; furthermore, we describe in §3.2.1 how there are individual clumps at two position angles observed within each composite clump, which means that one individual clump could be dominated by initially cool prominence material while the other individual clump (that is spatially-distant along the POS) could be dominated by initially hot coronal material. The temperature and ion stratification could also indicate the presence of the CME's prominence-core transition region (Engvold, 1988; Parenti et al., 2012; Rivera et al., 2019a).

Ionization states: With respect to ionization states, the initial ionization fractions have strong correlations and anti-correlations with temperature due to our assumed initial condition of ionization equilibrium; however, our time-dependent non-equilibrium ionization calculations ensured that the evolution of the ionization fractions did not always (anti-)correlate strongly with the evolution of the respective plasma cloud's temperature. Only the ionization fraction profiles of H I consistently showed a strong relationship with its respective plasma cloud's temperature profile.

Density: With respect to density, there are many models that exhibit degeneracies due to the trade-off that can occur between density and temperature in order to generate the same observed intensity ratio. Frequently, the upper limit we determine for final temperatures corresponds to the lower limit we determine for final densities. Fortunately, we significantly mitigate such degeneracies by performing the robust double-ratio analyses. This trade-off occurs only to meet the required intensity ratios at the coronal heights of our observations; therefore, the trade-off is not always present in the plausible initial conditions we infer.

Expansion Rates: Our inferred initial densities are often influenced by the assumed expansion rate. The initial conditions can differ substantially between distinct expansion rate assumptions while still producing the observed intensity ratios at the final two observation heights. Different initial conditions suggested by our models infer different historical evolutions for the CME's physical

conditions. Therefore, models using different expansion rates can be in agreement by yielding the same observed intensity ratios while disagreeing on the CME's historical evolution.

The expansion rate's influence on the density also manifests through its simple monotonic decrease (from the aforementioned power law of Equation 3.4) between the beginning of our models at 1.1 $R_\odot$ and the observations at 2.6 and 3.1 $R_\odot$. Our models suggest that when α_t=2 the density drops by four orders of magnitude between the inferred initial density and the final density. The density only drops by 2 orders of magnitude when α_t=1. This is because the observational constraints on the density must be met regardless of expansion rate. Thus, in order for a model to reach a given density at the observation heights, its corresponding initial density must be greater for greater expansion rates.

Heating Energy: With respect to the constant heating rates, the constraints are influenced by the expansion rates. In the three analyses detailed earlier, we report a lower limit of $C_H = 10^{-15}$ erg s^{-1} consistently when $\alpha_t = 1$; but in this case, the heating becomes negligible compared to the cooling. Any heating rate coefficient $C_H \leq 10^{-15}$ erg s^{-1} makes the heating negligible when α_t=1. However, this low heating rate coefficient is still significant when α_t=2. This is because the square-density dependent radiative cooling drops quickly for α_t=2 and eventually becomes low enough to make the total cooling comparable to the low heating. Due to this low heating's significance for the case of α_t=2, the thermal energy is often allowed to be very low and thus be in disagreement with observational constraints. In other words, the low heating rate coefficients that work well for α_t=1 (e.g., $C_H < 10^{-15}$ erg s^{-1}) are often too low for α_t=2.

The relationship between the heating rate, assumed expansion rate, and inferred initial conditions affects the cumulative heating energy. As mentioned in §3.4, the cumulative heating energy is determined by accounting for the initial thermal energy and the continuous input of thermal energy via the heating function. Our resultant models show that a slower expansion rate permits a lower heating rate coefficient and a lower initial temperature. This is why the cumulative heating energies we report (in Figure 3.10) are typically lower for the α_t=1 models than the α_t=2 models.

Degeneracies: All of the relationships exhibited amongst our various ratio analyses become more ambiguous as analyses are plagued by more degeneracies. The single-ratio analysis using the $\frac{\text{O VI 1032}}{\text{O VI 1038}}$

ratio suffers the most from degeneracies, and thus, although the aforementioned relationships are present, they have a minor effect on the (lack of) constraints. However, the $\frac{\text{O VI 1032}}{\text{O VI 1038}}$ ratio proved to be the most useful ratio in our double-ratio analyses as we mitigated the degeneracies and tightened the energy budget constraints. The tight constraints of the double-ratio analyses are exemplified in Figures 3.10d and 3.10d for the energy budget and Figures 3.11b and 3.11b for the physical conditions.
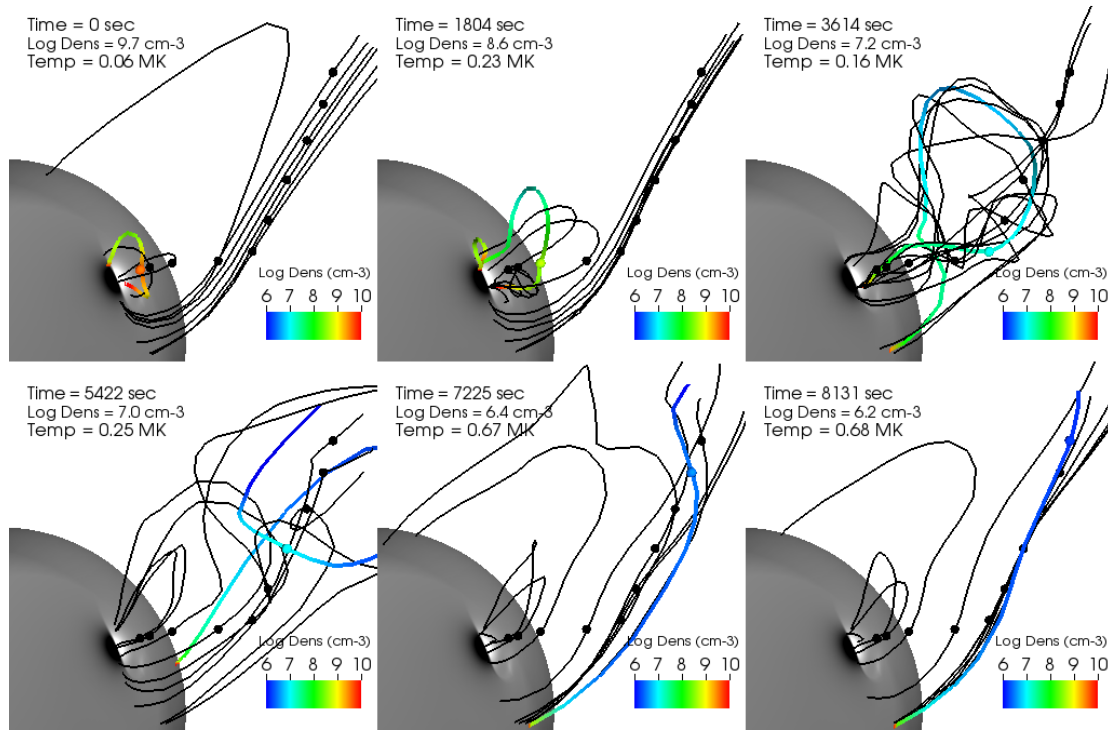
Figure 3.12: MAS code's simulation of a slow CME (Reeves et al., 2019). The trajectory for a parcel of plasma within the dense CME core is visualized. It's local density and temperature are listed in each panel. The only magnetic field lines that are illustrated are those for which the plasma will eventually be frozen into. These are shown as black lines. In each of the six panels, the one colored field line indicates where the plasma is currently located. The color indicates the density of the environment along that field line and the large dot shows the parcel's position along that field line. As time progresses the field lines elongate, get tangled, and extend outward into the corona. Such morphology from the magnetic flux rope is partly responsible for the decelerations and accelerations seen in Figure 3.13a.

3.6.2   Insight from MAS MHD model

We use a simulated CME to compare the evolutionary effects of our heating parameterizations. Our resultant 1D numeral models derive from the heating rate coefficients that are necessary to produce

models that agree with the observations at 2.6 and 3.1 $R_\odot$. We can use the resultant coefficients to suggest if one heating parameterization evolves the physical properties in a way that is more realistic than another heating parameterization. This can be done if the realistic simulation of a CME exhibits physical conditions similar to that of the observed 1999 CME.

Reeves et al. (2019) thoroughly describes the global behavior and energetics of the CME simulation that we use. Within this CME, we extract an exemplary parcel of plasma and monitor its characteristics as we follow its evolution. Its environment and localized properties are illustrated in Figure 3.12. As can be seen, the plasma is sometimes located in a high density environment compared to the regions along its respective magnetic field line. These densities imply that the plasma would seem very bright along one part of the field line but would seem faint if it were at another part of the field line and observed with UVCS at a given slit height.

The trajectory of the plasma is reported in Figure 3.13a. We only focus on its journey from $r = 1.2\ R_\odot$ to 2.7 $R_\odot$ since that reaches a height similar to the heights of the three observed composite clumps. As can be seen from the simulated plasma's v_r, v_θ, and v_φ components, it does not travel in a purely radial direction. Moreover, its absolute speed can be as high as 220 km s^{-1}, which is also similar to the three observed composite clumps. There is a consistent deceleration beyond 6,000 seconds (and beyond 2.3 $R_\odot$), which corresponds to many of the magnetic field lines being radially oriented. In the last two panels of Figure 3.12, at the two times beyond 7,000 seconds, the plasma is frozen-in a nearly radial magnetic field line, which allows the gravitational deceleration to strongly influence the plasma motion. At these times, there is a $\sim$40 m s^{-2} gravitational deceleration that is largely responsible for the consistent $\sim$140 m s^{-2} deceleration reported in Figure 3.13a.

The evolution of the plasma's localized physical conditions is reported in Figure 3.13b. As seen from the plasma β, the magnetic pressure consistently dominates early in the plasma's evolution but gradually decreases compared to the plasma pressure. The density gradually decreases but has a momentary increase near 1.9 $R_\odot$. The evolution of the plasma temperature is affected by the local environment's radiation cooling, conduction, expansion, compression, ohmic heating, ambient coronal heating, and the advection of the plasma through this environment. Also, the dominant magnetic pressure may allow a portion of magnetic energy to be converted into thermal energy throughout

the plasma's evolution. The simulation's physical model, including its heating and cooling terms, are described in detail by Reeves et al. (2019). Although this simulation was not constructed to duplicate the observed 1999 CME, we find that at certain times and heights, the simulated plasma within the dense CME core exhibits a density and temperature that are similar to that of the observed clumps.

To compare heating parameterizations, we focus only on moments in the simulated plasma's journey when the density and temperature agree with the observed clumps. We treat the simulated density and temperature as data inputs for our 1D modelling procedure (cf. §3.4) and re-evaluate the coefficient C_H for each heating parameterization. Now, we make the heating rate coefficient vary with time. We consider the length of time in which it agrees with the observationally constrained C_H coefficients.

To choose an expansion rate for our calculations, we considered the simulated plasma's density profile. It does not follow a smooth power law but the density profile does drop by at least three orders of magnitude, which is done consistently by our constrained quadratic expansion rate models but is never done by our linear expansion rate models. This suggests that an expansion index of $\alpha_t = 2$ for our power law is more realistic than $\alpha_t = 1$ when describing a plasma within the CME core.

The evolution of each time-variant heating rate coefficient is presented in Figure 3.13c as a black solid line. The red dotted lines indicate the upper and lower limits of the time-invariant coefficient that described the observed clumps. Since we have ruled out the linear expansion rate, only the limits derived from quadratic expansion rate models are plotted as red dotted lines. The coefficient for the Q_{n^2} parameterization is not considered since only the linear expansion rate models could describe the observed clumps (cf. §3.8.1). This implies that the Q_{n^2} parameterization is not as realistic as the rest of our five parameterizations, which all attempt to imitate the rate of heating caused by the unknown CME heating mechanisms.

For the four remaining parameterizations, each time-variant coefficient drops drastically near $1.9\ R_\odot$. Within this region, the coefficients become negative. This is due to the increase in density (i.e., compression) at the time of 4,300 seconds which is also one of the times at which the plasma's

TABLE 3.4: Using 3D MHD CME evolution to compare
realistic heating rates and parameterizations

Heating	1D model limits for observed plasma (cf. §3.4)			3D evolution matches observed limits (cf. §3.6.2)	
	$\text{Log } n_e$	$\text{Log } T_e$	$\text{Log } C_H$	$(\%)_{n,T}$	$(\%)_{C_H,(n,T)}$
Q_n	[4.176, 7.146]	[4.167, 6.399]	[-15, -12.6]	43	0
Q_{AHH}	[5.529, 6.788]	[4.370, 6.621]	[-6.6, -5.0]	19	0
$Q_{\text{KR}}(\alpha_B = 3)$	[5.852, 7.146]	[4.088, 5.808]	[-2.400, -0.760]*	30	30
$Q_{\text{KR}}(\alpha_B = 2)$	[5.495, 6.788]	[4.139, 6.100]	[-2.400, -0.760]*	19	71

Notes. The heating rate coefficient C_H is re-evaluated as a time-variant parameter while the density and temperature profiles from the MHD CME simulation act as data inputs for the modelling procedure described in §3.4.

Only the 1D model limits derived from the quadratic expansion rate models are considered, which excludes the Q_{n^2} parameterization (cf. §3.8.1).

The $(\%)_{n,T}$ is the fraction of time covered by the dashed turquoise lines (cf. Figure 3.13c) compared to the 2.3 hours covered by the black solid lines in Figure 3.13. The solid green line is overplotted onto the turquoise dashed line. The $(\%)_{C_H,(n,T)}$ is the fraction of time covered by the green line compared to the total turquoise line. See Figure 3.13c and §3.6.2 for details.

*This corresponds to $\log(B_0/G) \in [-0.5, 0.32]$, which ranges from 0.3 to 2.1 Gauss.

radial acceleration a_r peaks and begins to drop (cf. Figure 3.13a). The temperature increases at this moment also. This is a result of the cooling from adiabatic expansion being reversed substantially while the plasma experiences a high temperature via advection. At this moment, the heating rates from the simulated plasma's advection and adiabatic compression are at their greatest; however, this is counteracted by the thermal conduction becoming a cooling term as it carries thermal energy away from the local environment near 1.9 $R_\odot$. For our 1D modelling, the time-variant coefficients account for this cooling by becoming negative and converting our heating term into a cooling term, which is a systematic response to how the increase in density near 1.9 $R_\odot$ converts our expansion cooling term into a heating term (cf. Equation 3.5).

The turquoise dashed line in Figure 3.13c indicates the period of time when the plasma simultaneously has a density and temperature that agree with the observed clumps. Since these two physical conditions match with observations, this is a period of time for which the time-variant C_H coefficient is likely to match with the observationally constrained time-invariant C_H coefficient. When

this matching of C_H also occurs, the moment is marked by a solid green line, which obscures a portion of the turquoise line. These moments are reported in Table 3.4. The $(\%)_{n,T}$ is the portion of time when the density and temperature simultaneously match with the observed clumps (i.e., the turquoise line) compared to the total 2.3 hours of data extracted from the MAS simulation (i.e., the black line). The $(\%)_{C_H,(n,T)}$ is the portion of time when the density, temperature, and time-variant C_H all simultaneously match with the observed clumps (i.e, the green line) compared to the total time in which only the physical conditions of density and temperature match (i.e., the turquoise line).

The $(\%)_{C_H,(n,T)}$ signifies how well the heating parameterization can produce a realistic C_H coefficient within the period of time that the physical conditions of density and temperature are realistic. The realistic limits for these three parameters are defined by the observed clumps' results and are summarized in Table 3.4. The simulated plasma exhibits the same density and temperature as the observed clumps for 43% of the time when the observed clumps are analyzed with the Q_n parameterization; however, the re-evaluated C_H is never the same as the observed clumps within this portion of time (i.e., 0% of this time). In contrast, the simulated plasma exhibits the same density and temperature as the observed clumps for 19% of the time when the $Q_{KR}(\alpha_B = 2)$ parameterization is used; and, within this time interval, the C_H coefficient matches 71% of the time. This suggests that the rate of heating given by our $Q_{KR}(\alpha_B = 2)$ parameterization can realistically describe the heating of a plasma for a longer portion of time than our other heating parameterizations. However, this does not imply that the parameterization is an accurate description of a plasma's heating mechanisms.

3.7 Summary and Conclusions

We have presented an analysis detailing the physical properties and energetics for the core material of a CME. This CME event occurred in 1999 and was observed by *SOHO*'s EIT, LASCO, and UVCS instruments. We proved that there were structures within the CME's core that crossed the (single) slit of UVCS once at 2.6 $R_\odot$ and once again at 3.1 $R_\odot$. Three different approaches were used to

confirm this serendipitous result. For the clumps of plasma observed, we revealed patterns of behavior in their positioning along the slit and in the shape of their light curves. The third form of confirmation came from the agreement between their average velocity estimates from multi-height observations and their instantaneous velocity estimates from the O VI doublet intensity ratios.

To better understand the CME heating problem, we used 1D numerical models to evaluate the internal thermal energy of the plasma as a function of height. We assumed the plasma is being continuously heated and we investigated five different parameterizations to represent the unknown CME heating mechanisms. We monitored the evolution of the model plasma's physical conditions, which included the temperature, density, and ionization states. The evolutionary profiles for these conditions extended from 1.1 to 3.1 $R_\odot$. We monitored the ionization states of H I, C III, O V, and O VI by using non-equilibrium ionization calculations. We required that these model ions produce emission that gives the same intensity ratios that UVCS observed at 2.6 and 3.1 $R_\odot$.

The intensity ratios allowed us to exploit the Doppler dimming effect and diagnose the instantaneous physical conditions of the observed clumps of plasma within the CME core. The evolutionary profiles were constrained by the observed intensity ratios, which in turn constrained the initial conditions of the CME material. We found evidence of initially cool but gradually heated prominence material as well as initially hot but gradually cooled coronal material being present within the observed clumps of plasma. We also found that the cumulative heating energy is comparable to the kinetic energy and gravitational potential energy, which signifies how important the heating processes are during the eruption and evolution of the CME.

We monitored the evolution of a realistic MHD simulation of plasma being heated within the dense CME core in order to determine which heating parameterizations provide the most realistic heating rates. We found that a quadratic self-similar expansion rate is more realistic than a linear self-similar expansion rate. Models derived from the quadratic expansion rate suggest that our magnetic heating parameterization is the most realistic parameterization when its magnetic field expansion is predominantly two-dimensional instead of three-dimensional.

Our robust analyses could have been improved if our observational constraints came from three heights in the corona instead of just two or if the two heights in the corona were more than 0.5 $R_\odot$

apart from each other. In either case, a longer baseline of the plasma's historical behavior would have been observed, which would have tightened our range of plausible evolutionary profiles—including our inferred initial conditions of the CME. For coronagraph spectrometers, the observations of the same CME structures at merely two heights is actually a fortuitous achievement. Historically, the lack of such observations is due partly to the single-slit aperture of these instruments; and, even more so, it is due to the unpredictable nature of a CME's initial location, time of eruption, and velocity. This problem is exacerbated for observations of diffuse and dynamic features in the CME core, which are difficult to track from one height to another.

Coronagraph spectrometers have been acquiring ultraviolet spectroscopic measurements of the extended corona (d_H=1.5–10$R_\odot$) since 1979, and yet, the type of fortuitous multi-height observations that we examined in our analysis is still seldom acquired (e.g., Ko et al., 2005). The first coronagraph spectrometer acquired measurements during its three suborbital flights (in 1979, 1980, and 1982) on the Nike boosted Black Brant V sounding rockets (e.g., Kohl et al., 1980). Later, the Ultraviolet Coronal Spectrometer (UVCS) instrument on board *SPARTAN 201* acquired measurements during four of NASA's Space Transportation System (STS) missions (in 1993, 1994, 1995, and 1998) (e.g., Strachan et al., 1994; Kohl et al., 1994). The *SOHO*/UVCS instrument was launched in 1995 as an improved version of *SPARTAN*/UVCS. Unfortunately, all three of these space-based ultraviolet coronagraph spectrometers are no longer operational.

Now, the new era of coronagraph spectrometers will have more than one slit aperture. In this way, the type of multi-height CME spectra analyzed in this paper can be achieved more frequently. The unpredictable nature of CMEs may remain but the multiple slits will monitor different heights in the corona simultaneously along the same position angle. Therefore, if a three-part CME is observed by one slit at one height then all three parts can be observed again by the next slit at the next height. We expect to see CME observations like this from the following multi-slit coronagraph spectrometer missions: the UltraViolet Spectro-Coronagraph (UVSC) Pathfinder instrument (Strachan et al., 2017) is scheduled to launch in 2021, and the Large Optimized Coronagraphs for KeY Emission line Research (LOCKYER) instrument (Ko et al., 2016; Laming & Vourlidas, 2019) is currently being designed.

3.8 APPENDIX

3.8.1 SQUARE-DENSITY PROPORTIONAL HEATING

Using the Q_{n^2} heating, there are three distinct plasma clouds modelled that agree with the observations: H I, O VI, and H I mixed with O VI. The same observational constraints applied to the Q_n heating analysis are also applied here. As a result, the physical conditions we derive for the CME when using this Q_{n^2} heating are similar to that of our Q_n heating results. However, this is only true for our linear expansion rate. This Q_{n^2} heating compels our models to have an excessive amount of heating near the solar surface when we use the quadratic expansion rate. As explained in §3.6.1, there is a correlation between the expansion rates and our inferred initial densities. The inferred initial densities are systematically greater for the faster expansion rate and, consequently, the square-density dependence of the Q_{n^2} function drives the thermal energy to excessively high temperatures. Conversely, lower initial densities lead to excessively low final densities that cannot explain our observed intensity ratios.

The energy budget under this heating parameterization is summarized in Figure 3.14. The kinetic and potential energies for the three clumps are given in Figure 3.14a. At the height of 3.1 $R_\odot$, our models describe the O VI dominant material as having the slowest velocity estimates, just as in the Q_n results. The cumulative heating energies are given in Figure 3.14b. We find this to be in the range of $10^{12.64-14.59}$ erg g^{-1}, which is similar to the Q_n heating results for its linear expansion rate models. The corresponding heating rate coefficients are in the range $\log(C_H$ / erg cm^3 s$^{-1}) \in$ [-

22.0, -19.8].

For each of the three single-ratio analyses detailed in §3.6.1, the characteristics exhibited when using the Q_n heating function are similar to the characteristics exhibited when using the Q_{n^2} heating function. For a given expansion rate, the common traits seen across all of our ratio analyses are also present with this heating function. However, the relationships that correlate or anti-correlate with the choice of expansion rate cannot be reaffirmed due to the lack of models that agree with observations when a quadratic expansion rate is assumed. Also, none of our resultant models match to give a double-ratio analysis with this heating function.

3.8.2   Wave Heating Parameterization

Using the Q_{AHH} heating, there are three distinct plasma clouds modelled that agree with the observations: H I, O VI, and H I mixed with O VI. As with the Q_{n^2} heating results, the physical conditions we derive for these plasma clouds are similar to that of our Q_n heating results due to our use of the same observational constraints. The evolution of these physical conditions varies between heating parameterizations, but the energy budgets remain similar regardless of the heating parameterizations. Also, the common traits seen in various ratio analyses for this heating parameterization exhibit the same relationships that we detailed in §3.6.1.

The kinetic and potential energies are given in Figures 3.15a and 3.15c. Just as in the Q_n and Q_{n^2} heating results, the O VI dominant material has the slowest velocities at 3.1 $R_\odot$. For our double-ratio analyses, we find very few models that agree with observations, and among these models, agreement is found only with clumps B and C. The cumulative heating energies, given in Figures 3.15b and 3.15d, are within the range $10^{13.97-14.86}$ erg g^{-1} for the quadratic expansion rate and $10^{12.84-14.36}$ erg g^{-1} for the linear expansion rate.

The corresponding heating rate coefficients are in the range $\log(C_H\,/\,\mathrm{erg\,cm}^{-3}\,\mathrm{s}^{-1}) \in$ [-6.6, -5.0] for the quadratic expansion rate and $\log(C_H\,/\,\mathrm{erg\,cm}^{-3}\,\mathrm{s}^{-1}) \in$ [-11.0, -5.8] for the linear expansion rate. The heating rate's lower limit of $C_H = 10^{-11.0}$ erg cm^{-3} s^{-1} gives negligible heating (compared to the cooling) under a linear expansion rate. Thus, within our observational constraints, all heating rates of $C_H \leq 10^{-11.0}$ erg cm^{-3} s^{-1} suggest that a model with no heating is sufficient to explain the

physical conditions when assuming a linear expansion rate. We presented a similar circumstance in our Q_n heating results (cf. §3.6.1). A model with negligible heating is more likely to be valid when the cooling is more steady due to slower expansion rates. The total cooling has a significant contribution from the square-density dependent radiative cooling that drops slowly under slow expansion rates. This steady cooling with no heating creates only small changes in the evolution of the material's physical conditions. Such a model is valid only when the initial density and initial temperature were already close to meeting our observational constraints at 2.6 and 3.1 $R_\odot$.

For comparison, we have used the same heating function (Q_{AHH}) and scale height ($\mathcal{H}$) as Allen et al. (1998) used in their thermal energy equations as they modelled the electron temperature (T_e) for the fast solar wind. They found that a heating rate coefficient 2.5×10^{-7} (or $10^{-6.6}$) erg cm^{-3} s^{-1} sufficed to have their models agree with observations. This is within the upper and lower limits of our heating rate coefficient (C_H) for both the quadratic expansion rate and the linear expansion rate models. This supports the notion that some of our models correspond to the coronal material (as opposed to prominence material) within regions of the CME core along the LOS and POS.

3.8.3 Magnetic Heating Parameterization

Using the Q_{KR} heating, there are three distinct plasma clouds modelled that agree with the observations: H I, O VI, and H I mixed with O VI. None of our models for the H I with O VI mixture agree with observations when a quadratic expansion rate is assumed. The physical conditions we derive for these plasma clouds are similar to the results obtained when using the Q_n, Q_{n^2}, and Q_{AHH} heating functions. This is the case for both the three-dimensional magnetic field expansion ($\alpha_B = 3$) and the two-dimensional magnetic field expansion ($\alpha_B = 2$). For each choice of α_B, the common traits seen in various ratio analyses for this Q_{KR} heating exhibit the same relationships that we detailed in §3.6.1.

The energy budget in the case of $\alpha_B = 3$ is summarized in Figure 3.16. In our kinetic energy estimates, the O VI dominant material has the slowest velocity at 3.1 $R_\odot$. The cumulative heating energies of the three plasma clouds we model are in the range $10^{13.73-14.90}$ erg g^{-1} for a quadratic expansion rate and $10^{12.83-14.33}$ erg g^{-1} for a linear expansion rate. The cumulative heating en-

ergy is influenced by our choice of an initial magnetic energy that can contribute to the heating. We considered magnetic field strengths within the range $\log(B_0/\mathrm{G}) \in [-0.50, 4.0]$. The magnetic field strengths that correspond to the cumulative heating results are within the range $\log(B_0/\mathrm{G})$ $\in [-0.50, 0.32]$ for the quadratic expansion rate and within the range $\log(B_0/\mathrm{G}) \in [-0.50, 0.73]$ for the linear expansion rate. The lower limits of $10^{-0.50}$ G are due to our cutoff for plausible magnetic field strengths. These initial conditions correspond to ratios of plasma pressure to magnetic pressure in the range of (initial) plasma-beta $\beta_0 \in [0.26, 3 \times 10^3]$ for the quadratic expansion rate and $\beta_0 \in [2 \times 10^{-5}, 40.8]$ for the linear expansion rate.

The energy budget in the case of $\alpha_B = 2$ is summarized in Figure 3.17. As with all other heating parameterizations, our models suggest that the O VI dominant material has the lowest kinetic energy at 3.1 $R_\odot$ among the plasma clouds we consider. The cumulative heating energies we find are in the range $10^{13.93-14.88}$ erg g^{-1} for the quadratic expansion rate and $10^{13.25-14.17}$ erg g^{-1} for the linear expansion rate. Their corresponding magnetic field strengths are within the range $\log(B_0/\mathrm{G})$ $\in [-0.50, 0.32]$ for the quadratic expansion rate and $\log(B_0/\mathrm{G}) \in [-0.50, 0.73]$ for the linear expansion rate. The corresponding initial plasma-beta values are in the range $\beta_0 \in [0.75, 2 \times 10^4]$ for the quadratic expansion rate and $\beta_0 \in [4 \times 10^{-5}, 190]$ for the linear expansion rate.

Between $\alpha_B = 3$ and $\alpha_B = 2$, the limits for B_0 are the same although the limits for β_0 differ. This attests to how the observational constraints from our intensity ratios influence the acceptable initial plasma pressure much more than the initial magnetic pressure. This is perhaps a consequence of using intensity ratios that come from emissivities that are directly affected by the plasma density and temperature.
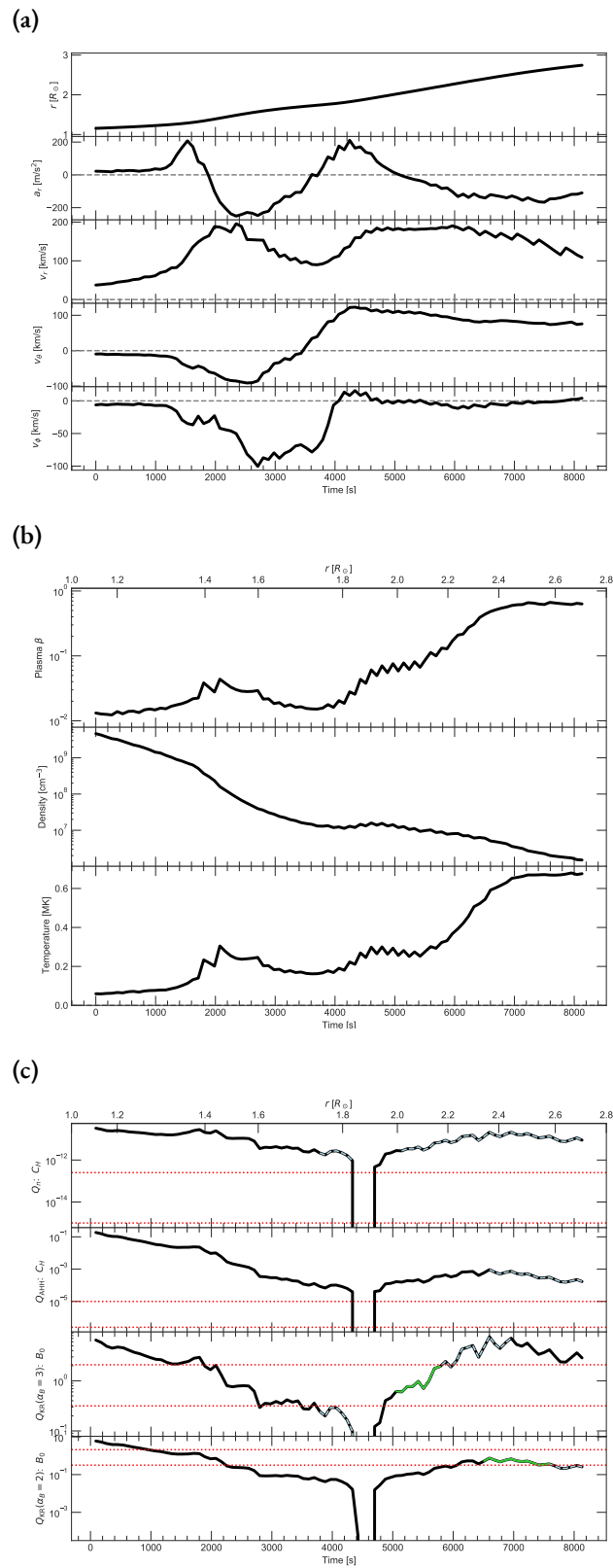
Figure 3.13: Simulation data is plotted for a parcel of plasma within the CME core as it travels for over 2 hours. The **(a)** trajectory, **(b)** physical conditions, and **(c)** time-variant heating rate coefficients for the plasma are given. See §3.6.2 and Table 3.4 for details.

(a)

(b)
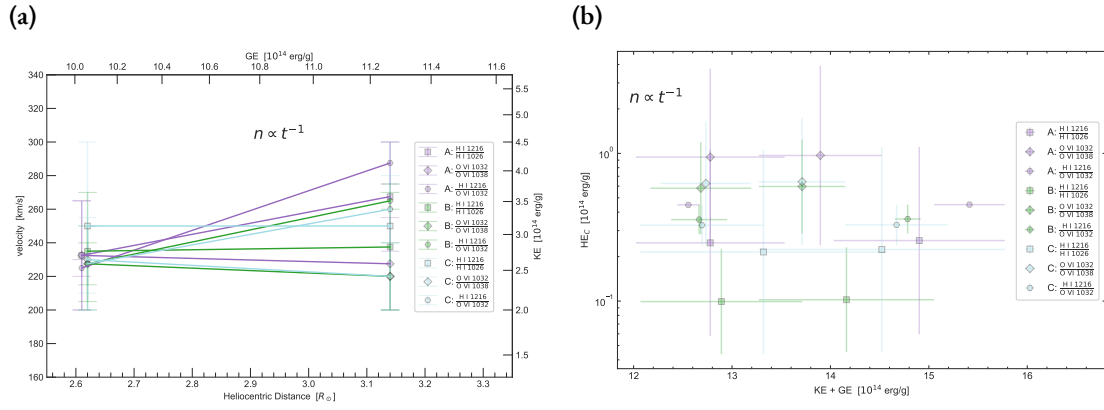
Figure 3.14: Observationally constrained models using the Q_{n^2} heating parameterization.

(a)

(b)

(c)

(d)
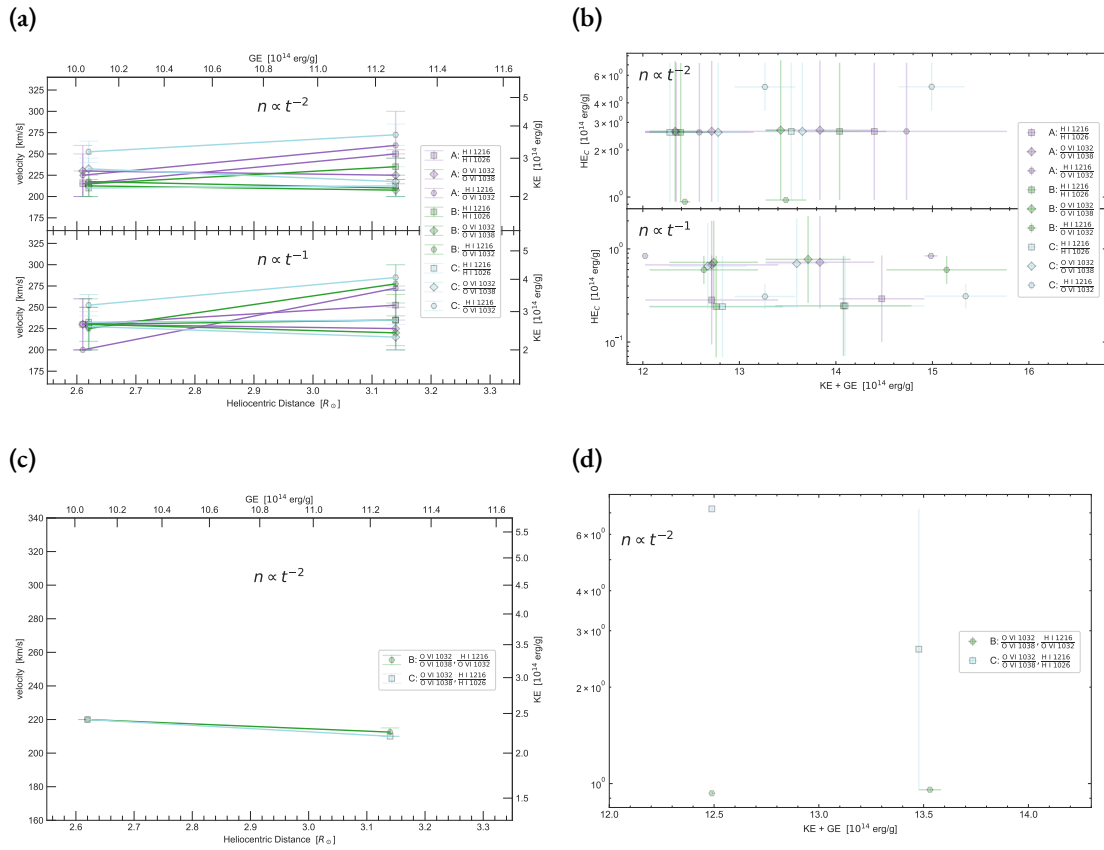
Figure 3.15: Observationally constrained models using the Q_{AHH} heating parameterization.
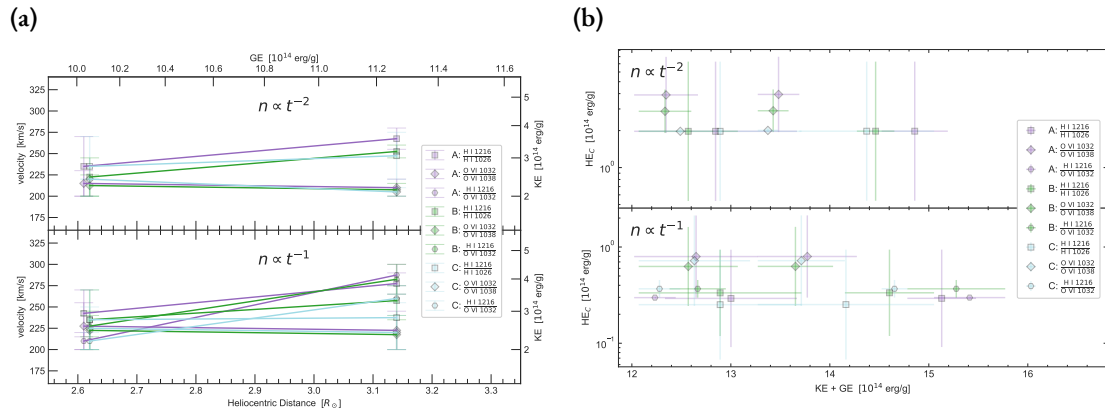
Figure 3.16: Observationally constrained models using the the Q_{KR} heating function with $\alpha_B = 3$.
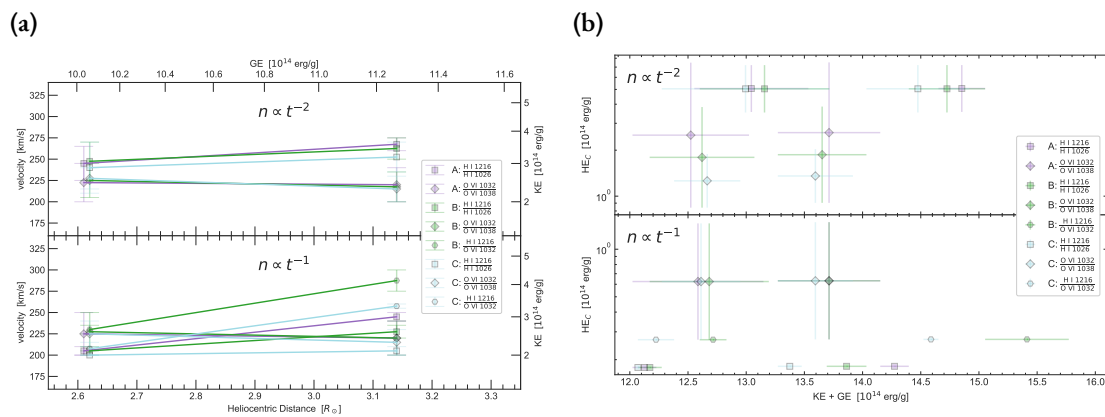
Figure 3.17: Observationally constrained models using the Q_{KR} heating function with $\alpha_B = 2$.

4

Solar CME Plasma Diagnostics Expressed

as Potential Stellar CME Signatures

On the solar surface, magnetized plasma frequently experience vehement instabilities within local

magnetic field structures that spawn the eruption of coronal mass ejections (CMEs). Since their

original discovery, a plethora of CMEs have been studied but the mechanisms that drive the ini-

tial eruption are still not fully understood (Hansen et al., 1971; Tousey et al., 1973; Gosling et al.,

1974). However, much progress has been made on this front as a variety of observational techniques

have been used to give unique perspectives on these transient events. Imagers monitoring the solar

disk in high-energy bandpasses have worked well with white light coronagraphs when attempting to

evaluate the CME kinetic energy. Its accelerating velocities have been seen to be a few tens to a few thousand km s^{-1}. Its accumulating mass is typically in the range 10^{14-16} g. As the CME traverses the corona, its physical conditions can be deduced from spectroscopic measurements. Its heating and cooling processes dictate the temperature for the relatively cool material at 10^4 K and hot material at 10^7 K.

Such physical properties inform the thermal energy, kinetic energy, and other components of the CME energy budget but can vary for distinct structures within the CME. Three commonly recognized CME parts that are adjacent but exhibit distinct properties are the leading edge, the flux rope, and the prominence core (Illing & Hundhausen, 1985). The energy budget is distributed throughout these features and originates primarily from the magnetic energy released upon eruption. This magnetic energy is liberated through a series of magnetic reconnections that reconfigure the magnetic structures that typically reside above flare loops.

A complex arcade of many magnetic loops can form two parallel structures with their chromospheric footpoints and yield the two-ribbon flare that resides below a current sheet that connects the (pre-eruption) flux rope and prominence to the surface flare loops. Such flares can brighten in Hα for several minutes, reach its peak, and take hours for its radiative energy to decay as its heating remains somewhat steady (Carmichael, 1964; Sturrock, 1966; Hirayama, 1974; Kopp & Pneuman, 1976; Tsuneta et al., 1992). Conversely, a compact flare comprises only one or a few magnetic loops that become unstable and are impulsively heated. Compared to the two-ribbon flare, the compact flare's profile has a faster rise and decay while also emitting less radiation (Alfvén & Carlqvist, 1967; Pallavicini et al., 1977; Dennis & Schwartz, 1989; Masuda et al., 1994).

Solar flares do not always occur with solar CMEs, but there is evidence to suggest that both phenomena become more coupled as the flare energy increases, which then corresponds to an increasing CME kinetic energy (Yashiro & Gopalswamy, 2009; Aarnio et al., 2011). Solar flares radiate energies of 10^{28-32} ergs and CMEs exhibit kinetic energies of 10^{28-33} ergs (e.g., Emslie et al., 2012; Aschwanden, 2017). Their coinciding occurrence at high energies, particularly when the two-ribbon flare is involved, may be the consequence of their common place of origin when both phenomena commence under the same magnetic fields of high pressure and complexity.

Between both forms of solar magnetic activity, it is not clear if their empirically derived coupling at high energies is valid for other stars. For stellar magnetic activity, statistical surveys on flare-CME relations are not feasible due to the dearth of stellar CME candidates detected.

Evidence for the detection of a stellar CME candidate is bolstered when accompanied by a stellar flare. Since their initial discoveries (Hertzsprung, 1924), stellar flares have been observed to have characteristics similar to solar flares (Hawley et al., 1995; Guedel et al., 1996). Thus, there is a chance that the processes initiating stellar CMEs are similar to solar CMEs. Furthermore, correlations with flare-CME occurrence rates as seen from the Sun may also be present on other stars. Although, these solar to stellar extrapolations cannot be verified until many stellar CME candidates are found, confirmed, and applied to statistical surveys. Thus far, the candidates are plagued with large uncertainties due to the lack of spatial, temporal, or spectral resolution and therefore require significant assumptions to interpret the features as CMEs.

Favorable geometric assumptions have been invoked to infer the presence of stellar CME candidates from coronal ultraviolet dimmings. Ambruster et al. (1986) used spectra from the International Ultraviolet Explorer (IUE) to investigate a flare from the M4.5V star, EV Lacertae, at a distance of 5.1 pc away. For exposure times of 45 minutes, the spectra for ultraviolet emission lines, such as the C IV 1550 Å line and the Mg II 2800 Å line, formed light curves that revealed a dimming, which occurred about an hour after a flaring event and lasted for almost 1.5 hours. Ambruster et al. (1986) favored a CME conclusion to explain the dimming. The CME could have erupted near the limb of the star during the flare onset but travelled non-radially outward at an angle heading closer to the stellar disk's center. During its travel, the CME's prominence core would have the cool C IV and Mg II plasma absorb radiation coming from the stellar surface.

Doppler blueshifts and spectral line asymmetries have been used to propose stellar CME candidates. Such techniques were used by Houdebine et al. (1990), Argiroffi et al. (2019), and Namekata et al. (2021) to introduce their plausible candidates, but many other stellar CME candidates also give unique incentives for why additional scrutiny should be applied to each CME candidate's magnetically active host star as the resolution and precision of modern instruments continues to improve.

Houdebine et al. (1990) used the European Southern Observatory (ESO) to investigate an im-

pulsive flaring event on the M4.5V star, AD Leonis (AD Leo), 5.0 pc away. During the flare, enhancements in the blue wings of the Hγ and Hδ Balmer line profiles were seen. Over 1-minute exposure times, the line asymmetry indicated a Doppler velocity of 5830 km s^{-1} and later 3750 km s^{-1}. In a separate analysis, Leitzinger et al. (2011) studied two flares from AD Leo with spectra from the Far Ultraviolet Spectroscopic Explorer (FUSE) (Christian et al., 2006). For exposure times ranging from a few minutes to about 30 minutes, the prominent features derived from C III emission lines at 977 and 1176 Å as well as O VI emission lines at 1032 Å and 1038 Å. A blueshift in the O VI 1032 emission line implied a Doppler velocity of 84 km s^{-1} while the other lines conveyed substantially slower Doppler velocities.

Argiroffi et al. (2019) used Chandra to study the flaring of the G1III star, OU Andromedae (OU And), 139.5 pc away. The duration of the flare's rise and decay lasted for 40 ks, and the spectra conveyed significant redshifts and blueshifts. Blueshifts of several hundred km s^{-1} were seen during the flare's rising phase and were interpreted as the motion of heated chromospheric plasma within a flare loop. Evidence for a CME was seen in a blueshift of 90 km s^{-1} that occurred after the flare, over an integration time of 58 ks.

Namekata et al. (2021) introduced a stellar CME candidate in their study of a flaring event on the G1.5V star, EK Draconis (EK Dra), 34.4 pc away. The flare was detected with the optical photometry of the Transiting Exoplanet Survey Satellite (TESS) while the spectroscopic instruments on the Seimei and Nayuta telescopes monitored the flare's Hα profile Ricker et al. (2014); Kurita et al. (2020). The impulsive flare lasted for 16 minutes and coincided with the brightening of redshifted Hα emission. Post-flare, the Hα line exhibited blueshifted absorption signatures that lasted for at least 1.5 hours. During this time, the spectra was acquired with exposure times of either 30 seconds or 3 minutes and an initial blueshift of 510 km s^{-1} was followed by a series of decelerating blueshifts. This was interpreted as the presence of relatively cool H I plasma from a stellar filament eruption traveling toward the observer for almost two hours.

These exemplary candidates (and many more) are interpreted as potential stellar CMEs primarily because their detected signals are analogous in some way to the observational signatures of solar CMEs (e.g., Osten & Wolk, 2017; Moschou et al., 2019; Vida et al., 2019). However, without spa-

tially resolving the star, these candidates require that assumptions be made about the morphology of the CME. Furthermore, the plasma diagnostics are often not determined by a variety of spectral lines, which would help constrain the travelling plasma's ever-changing physical conditions. Among many parameters, the candidates have estimates of mass, absolute velocity, temperature, density, and ionization states that are largely uncertain. Consequently, each candidate's identity as a stellar CME remains uncertain.

If more spectral lines are utilized simultaneously in the hunt for stellar CMEs, deducing the plasma properties would require less assumptions. Considering this, we emphasize the benefits of using observationally constrained plasma diagnostics from solar CMEs and we make predictions for how bright the same CME signal would be for certain spectral lines if observed as stellar CMEs. In this work, we scrutinize three previously studied solar CMEs and determine the feasibility of detecting the same spectral signal for the generic case of a stellar CME producing emission lines in the ultraviolet wavebands. For our predictions, we assume the hypothetical emitting plasma has a mass larger than that of solar CMEs, corresponding to 10^{17} g. For an emission line observed during a solar CME, we calculate the luminosity and amplify it by a factor corresponding to the ratio between the solar CME's mass and our assumed stellar CME mass, which can equate to a factor of 10^3. Similarly, this factor can also correspond to how the observed energy of stellar superflares ($> 10^{33}$ ergs) can be hundreds or thousands of times greater than the most energetic of solar flares. We assume that the scaled up luminosity yields a flux that will be detected by an instrument that is subject to an effective area similar to that of the *Hubble Space Telescope's* (*HST*) Cosmic Origins Spectrograph (COS).

For distinct solar CMEs, the calculations are described in Sections §4.1, §4.2, and §4.3. We give our final remarks in §4.4 regarding important caveats that must be considered when searching for stellar CMEs, including the utility (or futility) of assuming solar-like properties to make sense of constrained (or unconstrained) properties of stellar magnetic activity signatures.

4.1 Solar CME Event, 9 April 2008

We consider the CME studied by Landi et al. (2010), which erupted on 9 April 2008. They examined the data acquired by instruments on the *SOHO* (Domingo et al., 1995), *Hinode* (Kosugi et al., 2007), and *STEREO* (Kaiser, 2005) spacecrafts. To gather spectra, the slit apertures of *Hinode*/EIS (Culhane et al., 2007) and *SOHO*/UVCS (Kohl et al., 1995) were monitoring the corona at heliocentric distances of 1.1 $R_\odot$ and 1.9 $R_\odot$ respectively. During the initial eruption, photometry of the solar disk was captured by *Hinode*/XRT (Golub et al., 2007), *SOHO*/EIT (Delaboudinière et al., 1995), and *STEREO-A*/EUVI; and, this was complemented by the coronagraph imagers *SOHO*/LASCO (Brueckner et al., 1995) and *STEREO-A*/SECCHI/COR 1 and COR 2. As a result, the cumulative spatial coverage for which this event was studied ranged from the solar disk out to 22 $R_\odot$.

4.1.1 Solar CME Characteristics

The CME was initially seen near the southwest limb of the solar disk. The CME's leading edge was only visible off the limb within the *STEREO-A* photometry. The flux rope was too faint and thus observed by none of the instruments, while the CME core was sufficiently bright for all of the instruments to capture it. Consequently, the physical properties deduced were based solely on the observed core and leading edge.

The total mass was roughly 10^{14} g. The leading edge was consistently accelerating as its velocity approached 700 km s^{-1} near 3 $R_\odot$, which is where the plasma became too dim to track any further. The core material's acceleration persisted until the plasma reached 5 $R_\odot$, which is where its velocity reached 475 km s^{-1} and remained constant out to 22 $R_\odot$. The velocity estimates were derived from the observed trajectory of the CME as it travelled across the imagers' plane of sky (POS) and created Doppler shifts in the spectrometers' spectra via the CME's motion along the line of sight (LOS).

The physical conditions experienced by the CME were determined primarily from the *Hinode*/EIS spectra at 1.1 $R_\odot$. Only the CME core was detected, and its density was found from density-sensitive intensity ratios between the emission lines observed by EIS. Assuming ionization equilib-

rium, the temperature was estimated for the ions detected and used to model the thermal distribution of the CME core plasma. The emission line ratios indicated the presence of various plasma environments within the core volume that experience distinct densities and temperatures. The densities evaluated were in the range $\log n_e$ [cm^{-3}] = 7.75–11.3, and the thermal distribution conspicuously revealed two distinct temperature ranges for the core material: $\log T_e$ [K] 4.9–5.4 and 5.5–5.9. Presumably the CME expanded and cooled as it travelled beyond 1.1 $R_\odot$, but there were no detectable density- nor temperature-sensitive line ratios to verify the evolving plasma diagnostics.

4.1.2 Solar to Stellar Extrapolation

The large range of spectral lines and ions detected by EIS allowed for a large range in temperature to be found in the CME core's thermal distribution. This distribution was given in the form of the differential emission measure (DEM), which describes how the amount of plasma emitting the observed radiation changes with the temperature. We use the DEM of this CME event to estimate the luminosity given off for a few ultraviolet spectral lines, and we consider if certain emission lines would be detectable if the CME's brightness derived from a distant star.

For each emission line that we consider, we estimate the plasma's emission measure (EM) and convert it to an absolute intensity by applying the emissivity model of Raymond & Doyle (1981). With the temperature-dependent DEM curve given by Landi et al. (2010), we integrate the DEM over a small interval of temperatures (0.1 dex) near the emitting ion's temperature of maximum formation (T_{max}). This yields the EM for each spectral line of interest.

We chose spectral lines that were already used to constrain the model of Raymond & Doyle (1981), which introduces a proportionality between the emission measure and absolute intensity:

$$I_{EM} = \frac{\text{EM}}{10^{26}\,[\text{cm}^{-5}]} I_{RD}, \tag{4.1}$$

where the predicted intensity I_{EM} for a given emission line is proportional the line's empirically derived intensity I_{RD} from Raymond & Doyle (1981), which corresponds to an emission measure of 10^{26} cm^{-5}.

TABLE 4.1: Solar ultraviolet emission lines considered for stellar CME detection

λ [Å]	Ion	Transition			$\log T_{max}$ [K]	$\log$ DEM [cm^{-5} K^{-1}][a]	I_{RD} [erg s^{-1} cm^{-2} sr^{-1}][b]	A_{eff} [cm^2][c]	$F_{10pc,CME}$ [photons][d]	$F_{Proxima,CME}$ [photons][d]
1663.5	O III	$2p^2$ $^3P_{1,2}$	-	$2s2p^3$ $^5S_2$	5.0	20.8	87.9	400	86	5.1×10^3
1549.5	C IV	$2s$ $^2S_{1/2}$	-	$2p$ $^2P_{1/2,3/2}$	5.0	20.8	3.40×10^3	900	7.0×10^3	4.1×10^5
1484.9	N IV	$2s^2$ $^2S_0$	-	$2s2p$ $^3P_{1,2}$	5.1	21.0	69.2	1200	365	2.2×10^4
1718.6	N IV	$2s2p$ $^1P_1$	-	$2p^2$ $^1D_2$	5.1	21.0	8.53	300	13	768
1238.8	N V	$2s$ $^2S_{1/2}$	-	$2p$ $^2P_{3/2}$	5.3	20.2	4.75×10^2	2400	1.0×10^3	6.2×10^4
1031.9	O VI	$2s$ $^2S_{1/2}$	-	$2p$ $^2P_{3/2}$	5.5	19.0	1.44×10^3	20	2	131

[a] DEM is for the CME studied by Landi et al. (2010).

[b] The I_{RD} is from Raymond & Smith (1977).

[c] The A_{eff} from the HST/COS gratings is merely a realistic reference we apply to our predicted signal (Fischer, 2021).

[d] The detected photons (cf. Equation 4.3) account for the assumed A_{eff}.

Once the model intensity I_{EM} is calculated for an observationally constrained EM, we convert the intensity into the following photon luminosity for any given transition line,

$$L_{\odot,CME} \,[\text{photons s}^{-1}] = 4\pi r^2 I_{EM}, \tag{4.2}$$

where we find the emitting plasma's radius to be approximately R=0.105 $R_\odot$ over the POS. The area roughly encompasses the size and shape of the CME core as seen from the *Hinode*/XRT images presented by Landi et al. (2010).

For this solar CME luminosity, we estimate the flux that might be observed if the same CME was successfully launched from a distant star. The detected flux is expressed in the simplified form,

$$F_{\star,CME} \,[\text{photons}] \sim \frac{L_{\odot,CME} \cdot f_\star}{4\pi d_\star^2} \cdot A_{\text{eff}} \cdot \Delta t, \tag{4.3}$$

which considers a star of distance $d_\star$ away, a telescope with an effective area of A_{eff}, an integration time of Δt, and a factor of $f_\star$ to account for a plausible discrepancy between typical solar CMEs and stellar CMEs of magnetically active stars. The flux corresponds to the generic case of an ultraviolet instrument with a wavelength-dependent A_{eff} that observes a stellar CME from d=10 pc away that is a factor $f_\star$ times brighter than the reference solar CME. For the CME examined by Landi et al. (2010), we scale the luminosity up by a factor of $f_\star = 10^3$, which corresponds to the ratio of our assumed stellar CME mass and this solar CME mass. If Δt=3600 seconds and the data gathered over an hour of observations are co-added, the resultant fluences are as shown in Table 4.1.

Among the emission lines tested, the C IV line gives the greatest signal and results in a signal-to-noise ratio of S/N $\approx$ 85 if only poisson photon noise is assumed. The evaluation of this signal employs generic assumptions that do not account for all of the specific sources of astrophysical and instrumental noise that could hinder the detection of this predicted signal. A detailed study of a predicted stellar CME's signal for a specific detector's systematic noise is beyond the scope of this paper; but, such an in-depth study would benefit from specifically considering the M dwarf flare star Proxima Centauri as a promising candidate for launching detectable stellar CMEs. Being the closest star system to our solar system, its distance of d=1.30 pc away results in a factor of $\sim$60 increase to

our flux approximations. Consequently, the stellar CME signal from the C IV emission line would give a S/N $\approx$ 640. In this case, a shorter integration time may suffice.

4.2 SOLAR CME EVENT, 12 DECEMBER 1997

Another CME event that we consider occurred during 12 December 1997 (Ciaravella et al., 2000, 2001). Images of the CME's footpoints and eruption from the *Yohkoh* Soft X-ray Telescope (SXT) and the Meudon Observatory Hα photometry complemented the data acquired by three *SOHO* instruments: EIT, LASCO, and UVCS. Ciaravella et al. (2000) used the pre-CME solar disk images from SXT and Meudon to monitor the evolution of the active regions near the CME's launch site (Tsuneta et al., 1991; Duff, 1982). The CME's morphology and physical conditions were determined from the EIT, LASCO, and UVCS post-eruption observations.

4.2.1 SOLAR CME CHARACTERISTICS

Upon eruption, only the prominence core component of the CME was clearly discerned in the *SOHO* fields of view. In EIT's 195 Å filter, it could be seen up to 1.2 $R_\odot$. Ciaravella et al. (2000) suggested that it was mostly cool ions, such as O IV at 1.5×10^5 K or O V at 2.5×10^5 K, that were captured in the images. This is in spite of there usually being hot Fe XII at 1.3×10^6 K that dominates the 195 Å bandpass of EIT. The prominence material was seen off the northwest limb traveling at 140 km s^{-1} near 1.7 $R_\odot$ and later seen traveling at more than 200 km s^{-1} in the LASCO/C3 field of view. The Doppler shifts from the UVCS spectra conspicuously indicate the plasma's helical motion, which is similar to the behavior theorized by CME flux rope models (e.g., Gibson & Low, 1998; Guo & Wu, 1998).

The physical conditions were deduced from the UVCS spectra acquired when the slit was positioned at 1.7 $R_\odot$. A temperature-sensitive intensity ratio from two Si lines (at 1303 and 1206 Å) was used to confirm the plasma's state of ionization equilibrium. Thus, the temperatures of maximum ion formation were utilized for the plasma diagnostics and ranged from 4.2 $< \log T_e$ [K] < 5.5. With these temperatures, the ions' emission measures were evaluated from the spectral lines de-

tected and the fiducial atomic transition rates (Raymond & Smith, 1977; Scholz & Walters, 1991; Griffin et al., 1993). For almost all of the ions observed, Ciaravella et al. (2000) found a flat emission measure distribution across their range of temperatures. The column emission measure can be approximated as $EM \approx \int n_e^2 dl$, which integrates over the observed plasma's column depth along the LOS. Strands of filamentary prominence material were seen crossing the UVCS slit, and the width of their presumably cylindrical structures were estimated as the column depths. Ciaravella et al. (2001) inferred the densities from the EMs and column depths which were in the range $6.0 < \log n_e \, [\text{cm}^{-3}] < 7.5$. The volume was estimated from the aforementioned LOS column depth and the prominence material's POS area as seen from LASCO. Consequently, the mass of the structures ranged from roughly 10^{13} to 10^{14} g.

4.2.2   Solar to Stellar Extrapolation

We primarily consider the EIT observations of the CME prominence material when extrapolating the flux out to stellar distances. We use the detected count rates from the CME and apply the EIT instrumental response function as summarized by Delaboudinière et al. (1995) in Figure 9 of their work. As a result, we estimate the CME's volume emission measure ($EM_V \approx \int n_e^2 dV$) with the following relationship,

$$\frac{EM_{V,\text{CME}}}{10^{44} \text{ cm}^{-3}} = \frac{\mathcal{L}_{\odot,\text{CME}}}{\mathcal{L}_{\text{EIT}}}, \tag{4.4}$$

which utilizes EIT's signal $\mathcal{L}_{\text{EIT}}$ in CCD counts per second as a function of temperature when the volume emission measure is 10^{44} cm^{-3}. EIT observations can detect plasma of temperatures within the range 0.06–3 MK. At a temperature of 10^5 K, the instrumental response is reported to be $\mathcal{L}_{\text{EIT}}[\text{counts s}^{-1}] = 2.0$. At the same 10^5 K temperature, the plasma will likely be bright in the C IV emission line that is discussed in §4.1.2. We estimate the average $\mathcal{L}_{\odot,\text{CME}} = 4.2 \times 10^3$ counts s^{-1} from the EIT images of the prominence material and, with Equation 4.4, find that $EM_{V,\text{CME}} = 2.1 \times 10^{47}$ cm^{-3}. This excludes the image (at the time of 23:34 UTC) that is the first to expose the erupting prominence material but is likely spatially coherent with bright flare material.

Relatively cool prominence material typically has a temperature of about 10^5 K upon eruption

and is seen at a similar temperature later in the the mid-to-high corona. This implies that there must be a substantial amount of heating within the plasma that is capable of being balanced with the CME's radiative and expansion cooling (Akmal et al., 2001; Lee et al., 2009; Murphy et al., 2011; Rivera et al., 2019b). Thus, the radiative loss rate of the emitting plasma can act as a lower limit of the heating rate that levels out (or increases) the plasma temperature and therefore yields a corresponding emission measure. At the temperature of maximum ion formation for C IV, we use its radiative loss rate coefficient, $\Lambda_{C\ IV}(T = 10^{5.0} \text{ K}) = 5.4 \times 10^{-8} \frac{\text{photons cm}^3}{s}$ from the CHIANTI database (Dere et al., 1997, 2019). We characterize the luminosity as

$$L_{\odot,CME} \, [\text{photons s}^{-1}] = A_Z f_{Z,z} \Lambda(T) \times \text{EM}_{V,\text{CME}} \tag{4.5}$$

which includes the (coronal) elemental abundance A_Z and ionization fraction $f_{Z,z}$ for ion z of element Z (Feldman et al., 1992). We find that $L_{\odot,CME} = 1.2 \times 10^{36}$ photons s^{-1} for C IV.

With this luminosity, we apply Equation 4.3 with $f_\star = 10^3$ and estimate the expected stellar fluences. We find $F_{10\text{pc},\text{CME}}$ and $F_{Proxima,CME}$ equate to 5.2×10^3 and 3.1×10^5 counts which suggests the S/N ≈ 70 and 555, respectively, if the integration time is only 1 minute. Since these estimates are heavily dependent on the EIT's instrumental response function, the detected signal and the required exposure time may vary drastically for the capabilities of a different instrument.

As a comparison, the O VI 1032 Å line is also worth considering since it is typically one of the brightest spectral lines observed when UVCS spectra are taken of the ambient corona and the transient coronal mass ejections. The instrumental response is at most 5.0 counts s^{-1} for plasma at $T_e = 10^{5.5}$ K. The radiative loss rate coefficient is $\Lambda_{O\ VI}(T_e = 10^{5.5} \text{ K}) = 3.1 \times 10^{-8} \frac{\text{photons cm}^3}{s}$, which results in the following predicted fluxes for detection over an integration time of 1 minute: $F_{10\text{pc},\text{CME}}$ and $F_{Proxima,CME}$ are 48 and 2.9×10^3 counts which imply a S/N ≈ 5 and 50, respectively. In this case, a longer exposure time may be preferable when attempting to detect a stellar CME signal from the O VI 1032 Å line.

4.3 Solar CME Event, 17 May 1999

The first CME of interest (cf. §4.1) was analyzed primarily from its spectra at 1.1 $R_\odot$. The same is true for the second CME of interest (cf. §4.2) at 1.7 $R_\odot$. We now pay heed to a CME event where its detailed spectral information was gathered at 2.6 and 3.1 $R_\odot$. This CME event was observed on 17 May 1999 by *SOHO*'s EIT, LASCO, and UVCS (Wilson et al., 2022).

4.3.1 Solar CME Characteristics

Upon eruption off the northwest limb, strands of the prominence material were captured by EIT. In the white light images of LASCO/C2, the canonical three-part CME can be discerned. Evidently, beyond 3 $R_\odot$, the leading edge accelerated to 500 km s^{-1} and was followed by a featureless void that separated it from the large, amorphous prominence core. The column density of the CME features discerned along the LASCO's plane of sky suggests a mass of 10^{15} g.

For UVCS, its automated observing program serendipitously placed the slit aperture at heights in the corona that were along the CME's unpredictable path. Only the prominence core was seen crossing the slit's field of view at any given exposure. Coincidentally, some specific plasma structures within the core were seen crossing the slit twice—once at 2.6 $R_\odot$ and once at 3.1 $R_\odot$. Thus, the average POS velocity was determined between the two heights along with the LOS velocity from the Doppler shifts of the spectra. Together, the absolute velocity was found to be 250 km s^{-1} for the prominence core. The plasma diagnostics were only evaluated for the core material featured in the UVCS spectra.

Due to the many spectral lines detected, a variety of observed intensity ratios were modelled to estimate the density of the expanding plasma and the temperature of the plasma under non-equilibrium ionization (NEI) conditions. The models employed ionization equilibrium as an assumed initial condition but still depended on NEI calculations when modelling the evolution of the plasma properties out to heights of 2.6 $R_\odot$ and 3.1 $R_\odot$.

As the plasma's thermal energy evolved, the observationally constrained temperature profile varied in accordance with a given heating parameterization. Among the five parameterizations that

Wilson et al. (2022) used to define the plasma's rate of heating, one proved to be the most consistent throughout the CME's evolution when the parameterization was applied to the UVCS CME data as well as the data from a similar CME that was constructed by the 3D magnetohydrodynamic (MHD) simulation of the MHD Algorithm outside a Sphere (MAS) code (Mikić et al., 1999; Downs et al., 2013; Lionello et al., 2013; Török et al., 2018; Reeves et al., 2019). This heating parameterization produced plasma heating rates that depend on the conservation of magnetic helicity as the CME flux rope expands (in two dimensions akin to a cylinder) and dissipates free magnetic energy (Taylor, 1974; Berger & Field, 1984; Kumar & Rust, 1996). We use the constrained plasma parameters that derived from this magnetic heating parameterization in order to estimate the flux as if the CME belonged to a distant star.

4.3.2 Solar to Stellar Extrapolation

The model temperature profiles of interest were given by Wilson et al. (2022) in Figure 8 of their work where they assume an inverse square law to express the expansion rate of the plasma. The evolving density and temperature affects the collisional and radiative excitation rates that yield the model luminosity for the observed plasma. The model plasma commences its journey at 1.1 $R_\odot$ and takes 1.3 hours to reach the final UVCS slit height of 3.1 $R_\odot$. During this journey, we model the luminosity as

$$L_{\odot, CME} \, [\text{photons s}^{-1}] = \varepsilon_\lambda \frac{M_{\odot, \text{CME}}}{\rho_{\text{CME}}}, \tag{4.6}$$

which incorporates the total emissivity ε_λ and models its collisonal and radiative excitation rate components as described in the following:

$$\varepsilon_\lambda = \varepsilon_{c,\lambda} + \varepsilon_{r,\lambda}$$

$$\varepsilon_{c,\lambda} = n_{Z,z} \cdot n_e q_{ex,\lambda}(Z, z, T), \tag{4.7}$$

$$\varepsilon_{r,\lambda} = n_{Z,z} \cdot I_\odot(\lambda_i + \delta\lambda_i)\sigma_\lambda \mathcal{W}(r).$$

The total mass density, $\rho_{\text{CME}} = m_e n_e + \sum\limits^{Z} \sum\limits^{z} m_{Z,z} n_{Z,z}$, is derived from the electron mass density $m_e n_e$, the atomic mass $m_{Z,z}$, and the ion density $n_{Z,z} = n_H A_Z f_{Z,z}$. The total mass of the CME $M_{\odot,\text{CME}}$ is estimated from LASCO white light images.

For Equation 4.7, the emissivity's collisional component $\varepsilon_{c,\lambda}$ depends on the excitation rate coefficient $q_{ex,\lambda}$ for a given spectral line. The radiative component $\varepsilon_{r,\lambda}$ depends the solar disk emission line profile $I_{\odot}$, which scatters off of the escaping CME plasma at a Doppler redshift $\delta\lambda_i$ from its incident wavelength that corresponds to the speed of the CME. The scattered radiation also correlates with the absorption cross section σ_λ and the solid angle $\mathcal{W}(r)$ of the scattering plasma that is subtended by the solar disk. These plasma parameters were constrained by UVCS observations and subsequently resulted in the evolutionary profiles presented by Wilson et al. (2022) for the densities, temperatures, and ionization states.

We evaluate the extrapolated stellar flux of the modelled solar radiation from O VI at 1032 Å and C III at 977 Å. The O VI and C III ions have maximum formation temperatures of $10^{5.5}$ and $10^{4.8}$ K, respectively. A reliable temperature-dependent emission measure distribution is not feasible to construct with the given observations of the plasma at 2.6 and 3.1 $R_{\odot}$. Thus, we do not apply an emission measure proportionality to estimate the flux from C IV. An EM distribution would be subject to large uncertainties considering the detected plasma was at heights near 3.0 $R_{\odot}$, which implies that it is likely subject to NEI conditions, relatively significant contributions from resonant scattering radiation, and subject to frozen-in ionization states. For C IV, we take note of how its maximum formation temperature of $10^{5.0}$ K is between that of O VI and C III; consequently, the results from O VI and C III can act as a qualitative proxy for what the unobserved C IV emission might yield.

For an integration time lasting the duration of the modelled 1.3-hour journey, we approximate the stellar CME fluence via Equation 4.3 with $f_\star = 10^2$. For the O VI 1032 Å line, the constrained model profiles yield the fluences $F_{10\text{pc,CME}} = 50$ photons and $F_{Proxima,CME} = 3.0 \times 10^3$ photons which suggest that S/N $\approx$ 5 and 55, respectively. For the C III 977 Å line, we assume $A_{eff} = 20$ cm^2 and find that $F_{10\text{pc,CME}} = 44$ photons and $F_{Proxima,CME} = 2.6 \times 10^3$ photons which imply that the S/N $\approx$ 5 and 50, respectively.

4.4 CME Search Caveats and Conclusion

The search for stellar CMEs is still heavily dependent on the simultaneous occurrence of stellar flares. Furthermore, *stellar* CME candidates are often confidently proclaimed when their observational signatures are similar to what is predicted from *solar* CME models or what is seen through *solar* CME observations. The candidates' dependence on stellar flares and solar analogs would not be a contentious point of concern if the plasma diagnostics for each candidate were robustly determined from a variety of observational techniques. Such techniques can include the concurrent use of several spectroscopic line ratios, where each ratio correlates with a parameter that describes the plasma conditions (e.g., density) and morphology (e.g., expansion speed).

In this work, we have reviewed a few solar CME studies that benefitted from the diagnostic capabilities of ultraviolet emission lines and line intensity ratios. We propose that such plasma diagnostics can strengthen the credibility of stellar CME detections, as long as the emission lines have a distinguishable signal. We focused mostly on three emission lines: C IV 1550 Å, O VI 1032 Å, and C III 977 Å. As summarized in Figure ??, we estimated the brightness of the lines' stellar-based signals, assuming the hypothetical stellar CME radiates similarly to solar CMEs. Presumably, the radiative profile (and underlying physics) of stellar CMEs would be similar to solar CMEs since the plethora of detected stellar flares often exhibit plasma properties that scale directly with solar flare properties, regardless of the wavelength regime or the unsolar-like radiative energy of stellar super-flares ($> 10^{33}$ ergs) (Guedel et al., 1996; Aschwanden et al., 2008; Pandey & Singh, 2012).
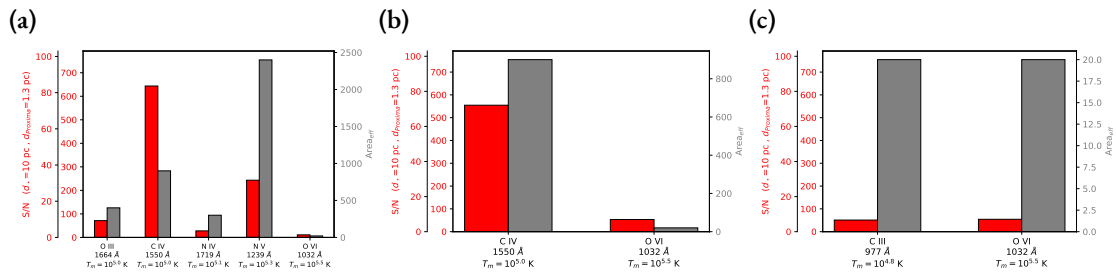

Figure 4.1: Predicted emission line signals for potential stellar CMEs, as extrapolated from the diagnostics of solar CMEs studied by **(a)** Landi et al. (2010) with an integration time of $\Delta t = 1$ hr, **(b)** Ciaravella et al. (2000) with $\Delta t = 1$ min, and **(c)** Wilson et al. (2022) with $\Delta t = 1.3$ hr. The estimated flux for a CME is scaled generically to a distance of 10 pc and specifically to the distance of Proxima Centauri at 1.30 pc.

If the physical coupling and statistical association of solar flare-CME events holds true for the stellar events, an efficient search for stellar CMEs might aim at targets that give off high-energy stellar flare signals. If magnetically active M dwarfs are the primary targets, their frequent flaring, as well as their abundance in the solar neighborhood, should improve the probability of finding superflares with their associated CMEs. This high energy stellar flare-CME relationship is qualitatively corroborated by the aforementioned CME candidates from Houdebine et al. (1990), Argiroffi et al. (2019), and Namekata et al. (2021), which were each associated with superflares.

Despite being a convenient source of observable magnetic activity, caution must be taken when depending on an active flaring star to successfully expel detectable CMEs. The strength and occurrence rate of such stellar magnetic activity phenomena are attributed partly to the dynamo-generated magnetic fields (Parker, 1955; Duvall et al., 1984; Noyes et al., 1984; Wright et al., 2011). Ambient fields of high magnetic pressure can confine the plasma that erupts below it. As a result, the plasma that would have escaped to become a CME reverses its direction and travels back to the coronal floor. Such failed CMEs might occur frequently on active flaring stars, as long as the kinetic energy of the erupted material is suppressed by the overbearing magnetic field energy (Joshi et al., 2013; Drake et al., 2016; Zuccarello et al., 2017; Alvarado-Gómez et al., 2018).

Since CMEs need not occur alongside (super)flares, a robust methodology for confirming CME candidates would consistently be capable of constraining the candidate's plasma motions, physical conditions, and energy budget without the simultaneous presence of a flare. Although counterintuitive, the presence of a flare can introduce scenarios for a false-positive CME detection. Flare-induced chromospheric brightenings (e.g., Kirk et al., 2017) and chromospheric evaporation (e.g., Milligan & Dennis, 2009) can generate upward plasma flows that yield a Doppler blueshift of several hundred km s^{-1} or less. From this perspective, the spectroscopic detection and characterization of flare-less stellar CME candidates may be more reliable than detections of stellar flare-CME candidates.

Furthermore, a flare-less stellar CME candidate may exhibit Doppler redshifts that can be used to confirm its CME identity. In this case, a detectable redshift would be less likely to derive from the flare-induced plasma downflows of chromospheric condensation (Milligan et al., 2006). Instead,

this redshift could be the result of the geometry between the CME's propagation direction and limb of the spatially unresolved stellar disk. As illustrated by Moschou et al. (2019), the redshift can derive from a CME erupting near the limb but behind the face of the stellar disk. As the CME expands and travels at an angle directed partially away from the observer, the plasma can eventually be seen off the limb of the stellar disk. Since the eruption began behind the face of the star, the possible presence of a concurrent flare would be unknown or impossible to detect directly.

A survey searching for flare-less stellar CMEs will likely be more successful when observing quiescent, Sun-like stars as opposed to observing magnetically active, young, late-type, low-mass stars that flare frequently. Despite their energetically weaker and less frequent magnetic activity, stars like our Sun might make for efficient survey targets since their weaker ambient magnetic fields make them less susceptible to failed CME events. Fortunately, although our Sun successfully launches CMEs every day, the planetary magnetosphere and atmosphere of the Earth has not been damaged beyond repair by these CMEs. By analogy, this bodes well for exoplanets within the habitable zones of CME-launching Sun-like stars. Furthermore, exoplanets orbiting active M dwarfs may witness more failed CMEs that are confined to the stellar corona than witness successful CMEs that strip them of their (exo)planetary atmosphere. These hypotheses can be tested if the search for stellar CMEs coincides with exoplanet surveys.

There is one space-based exoplanet mission that might coincidentally detect the type of stellar CME signatures that we have extensively discussed. The UV-SCOPE (Ultraviolet Spectroscopic Characterization of Planets and their Environments) mission concept is designed to have a space-based spectrograph sit and stare at the host stars of transiting exoplanets in order to study the upper atmospheres of exoplanets with transmission spectroscopy (Shkolnik et al., 2021; Line et al., 2021; Loyd et al., 2021). Due to its expected long-term temporal coverage (per target) and its spectral coverage of near-to-far UV wavelengths, promising stellar CME candidates may be detected and characterized via diagnostic UV emission lines.

5

Conclusion

In this dissertation, we have discussed a variety of spectroscopic techniques that we have applied to various research topics: spectrograph instrumentation, exoplanet characterization, solar CME diagnostics, stellar CME detections.

We began by presenting the results of commissioning the MINERVA spectrograph. Since then, the Southern Hemisphere analog has been commissioned: MINERVA-Australis, also known as MINERVA-South (Addison et al., 2019). Both MINERVA-North and MINERVA-South collectively utilizes their all-sky coverage to confirm and characterize exoplanet candidates that were originally introduced by the *Transiting Exoplanet Survey Satellite* (*TESS*). Both observatories exercise the Doppler Tomography technique to measure stellar obliquity during exoplanet transits. The mea-

sured Doppler shifts can indicate the angle between the host star's (projected) rotation axis and the angular momentum vector of the planet's orbit. Consequently, the estimated alignment between planet and star can be used to constrain planetary formation and migration models.

The exoplanet work was followed by the solar CME analysis. Upon the completion of the study, a call to action was implicitly given in order to encourage the design, funding, building, and utilization of coronagraph spectrometers, especially if it is capable of monitoring the corona at two or more heights simultaneously. Multi-slit coronagraph spectrometers provide the opportunity to precisely determine the propagation speeds and velocity amplitudes of oscillating Alfven waves, sound waves, and magnetosonic waves as these perturbations travel along the spectrometer's POS and crosses two or more slits consecutively. Additionally, multi-slit coronagraph spectrometers will allow multiple components of a CME to be observed simultaneously. As an example, the spectra of the prominence core can be acquired from one slit while spectra for the lesser-known prominence-corona transition region (PCTR) is acquired from another slit at a higher height in the corona.

Lastly, we discussed our predictions for detecting spectral signatures of stellar CMEs. We emphasized the use of CME-related ultraviolet emission lines that are likely to be successfully detected if an instrument similar to *HST*/COS were used. We also gave ideas on how a search for stellar CMEs would efficiently make use of (exoplanet) observing runs and spectroscopic techniques.

Hopefully, this dissertation will serve as encouragement for the astronomy community to promote and fund interdisciplinary research efforts and collaborations. There are obvious ways in which, historically, scientists of one field of study have benefitted from the work of scientists in a very different field; however, it seems like there are social, intellectual, and financial boundary conditions between astronomy subfields that are excessively tedious to overcome. It seems like the obvious connections between subfields are ideas that seldom come to fruition despite being ideas that are frequently discussed amongst astronomy colleagues. Historically, many precedents for interdisciplinary research efforts and collaborations have already been set; however, the sheer difficulty and discouragement experienced when following the interdisciplinary path (especially, before receiving a tenured position) is hindering great ideas from coming to fruition and thus is also hindering astronomers from making a greater impact on the scientific community and the lives of those around

us who become inspired by our knowledge of the universe.

References

Aarnio, A. N., Stassun, K. G., Hughes, W. J., & McGregor, S. L. 2011, SoPh, 268, 195

Addison, B., Wright, D. J., Wittenmyer, R. A., et al. 2019, arXiv e-prints, arXiv:1901.11231

Akmal, A., Raymond, J. C., Vourlidas, A., et al. 2001, ApJ, 553, 922

Alfvén, H., & Carlqvist, P. 1967, SoPh, 1, 220

Allan, D. W. 1966, IEEE Proceedings, 54, 221

Allen, L. A., Habbal, S. R., & Hu, Y. Q. 1998, JGR, 103, 6551

Allen, L. A., Habbal, S. R., & Li, X. 2000, JGR, 105, 23123

Alvarado-Gómez, J. D., Drake, J. J., Cohen, O., Moschou, S. P., & Garraffo, C. 2018, ApJ, 862, 93

Ambruster, C. W., Pettersen, B. R., Hawley, S., Coleman, L. A., & Sandmann, W. H. 1986, in ESA Special Publication, Vol. 263, New Insights in Astrophysics. Eight Years of UV Astronomy with IUE, ed. E. J. Rolfe & R. Wilson, 137–140

Argiroffi, C., Reale, F., Drake, J. J., et al. 2019, Nature Astronomy, 3, 742

Aschwanden, M. J. 2017, ApJ, 847, 27

Aschwanden, M. J., Stern, R. A., & Güdel, M. 2008, ApJ, 672, 659

Aschwanden, M. J., Xu, Y., & Jing, J. 2014, ApJ, 797, 50

Bakos, G. Á., Lázár, J., Papp, I., Sári, P., & Green, E. M. 2002, PASP, 114, 974

Barnes, S. I., Gibson, S., Nield, K., & Cochrane, D. 2012, in ProcSPIE, Vol. 8446, Ground-based and Airborne Instrumentation for Astronomy IV, 844688

Bemporad, A., Poletto, G., Suess, S. T., et al. 2006, ApJ, 638, 1110

Berger, M. A., & Field, G. B. 1984, Journal of Fluid Mechanics, 147, 133–148

Bernstein, R. M., Burles, S. M., & Prochaska, J. X. 2015, PASP, 127, 911

Bertin, E., & Arnouts, S. 1996, AAPS, 117, 393

Bolton, A. S., & Schlegel, D. J. 2010, PASP, 122, 248

Bradshaw, S. J., & Klimchuk, J. A. 2011, ApJS, 194, 26

Broomhall, A. M., Chaplin, W. J., Davies, G. R., et al. 2009, MNRAS, 396, L100

Brueckner, G. E., Howard, R. A., Koomen, M. J., et al. 1995, SoPh, 162, 357

Butler, R. P., Marcy, G. W., Williams, E., et al. 1996, Publications of the Astronomical Society of the Pacific, 108, 500

Butler, R. P., Wright, J. T., Marcy, G. W., et al. 2006, ApJ, 646, 505

Campbell, B., Walker, G. A. H., & Yang, S. 1988, ApJ, 331, 902

Carmichael, H. 1964, in NASA Special Publication, Vol. 50, 451

Choi, J., Dotter, A., Conroy, C., et al. 2016, ApJ, 823, 102

Christian, D. J., Mathioudakis, M., Bloomfield, D. S., et al. 2006, AAP, 454, 889

Ciaravella, A., Raymond, J. C., Reale, F., Strachan, L., & Peres, G. 2001, ApJ, 557, 351

Ciaravella, A., Raymond, J. C., van Ballegooijen, A., et al. 2003, ApJ, 597, 1118

Ciaravella, A., Raymond, J. C., Thompson, B. J., et al. 2000, ApJ, 529, 575

Cranmer, S. R., Panasyuk, A. V., & Kohl, J. L. 2008, ApJ, 678, 1480

Crause, L. A., Butler, R. P., Nave, G., et al. 2018, in Society of Photo-Optical Instrumentation Engineers (SPIE) Conference Series, Vol. 10702, 107025S

Croll, B., Dalba, P. A., Vanderburg, A., et al. 2017, ApJ, 836, 82

Culhane, J. L., Harra, L. K., James, A. M., et al. 2007, SoPh, 243, 19

Cutri, R. M., Skrutskie, M. F., van Dyk, S., et al. 2003, VizieR Online Data Catalog, II/246

Czekala, I. 2017, PSOAP: Precision Spectroscopic Orbits A-Parametrically, ascl:1705.013

Davies, E. E., Forsyth, R. J., Good, S. W., & Kilpua, E. K. J. 2020, SoPh, 295, 157

Delaboudinière, J. P., Artzner, G. E., Brunaud, J., et al. 1995, SoPh, 162, 291

Dennis, B. R., & Schwartz, R. A. 1989, SoPh, 121, 75

Dere, K. P., Del Zanna, G., Young, P. R., Landi, E., & Sutherland, R. S. 2019, ApJS, 241, 22

Dere, K. P., Landi, E., Mason, H. E., Monsignori Fossi, B. C., & Young, P. R. 1997, AAPS, 125, 149

Diego, F., Charalambous, A., Fish, A. C., & Walker, D. D. 1990, in Society of Photo-Optical Instrumentation Engineers (SPIE) Conference Series, Vol. 1235, Instrumentation in Astronomy VII, ed. D. L. Crawford, 562–576

Domingo, V., Fleck, B., & Poland, A. I. 1995, SoPh, 162, 1

Dotter, A. 2016, ApJS, 222, 8

Downs, C., Linker, J. A., Mikić, Z., et al. 2013, Science, 340, 1196

Drake, J. J., Cohen, O., Garraffo, C., & Kashyap, V. 2016, in Solar and Stellar Flares and their Effects on Planets, ed. A. G. Kosovichev, S. L. Hawley, & P. Heinzel, Vol. 320, 196–201

Dravins, D. 1990, A&A, 228, 218

Duff, I. 1982, Journal of the British Astronomical Association, 92, 278

Dumusque, X. 2012, PhD thesis, Observatory of Geneva

Duvall, T. L., J., Dziembowski, W. A., Goode, P. R., et al. 1984, Nature, 310, 22

Eastman, J. 2017, EXOFASTv2: Generalized publication-quality exoplanet modeling code, ascl:1710.003

Eastman, J., Gaudi, B. S., & Agol, E. 2013, Publications of the Astronomical Society of the Pacific, 125, 83

Eastman, J., Siverd, R., & Gaudi, B. S. 2010, PASP, 122, 935

Emslie, A. G., Dennis, B. R., Holman, G. D., & Hudson, H. S. 2005, Journal of Geophysical Research (Space Physics), 110, A11103

Emslie, A. G., Kucharek, H., Dennis, B. R., et al. 2004, Journal of Geophysical Research (Space Physics), 109, A10104

Emslie, A. G., Dennis, B. R., Shih, A. Y., et al. 2012, ApJ, 759, 71

Engvold, O. 1988, in Solar and Stellar Coronal Structure and Dynamics, ed. R. C. Altrock, 151–169

Feldman, U., Mandelbaum, P., Seely, J. F., Doschek, G. A., & Gursky, H. 1992, ApJS, 81, 387

Feldman, U., Schühle, U., Widing, K. G., & Laming, J. M. 1998, ApJ, 505, 999

Feng, X., Yang, L., Xiang, C., et al. 2010, ApJ, 723, 300

Filippov, B., & Koutchmy, S. 2002, SoPh, 208, 283

Fischer, W. J. 2021, Cycle 27 COS NUV Spectroscopic Sensitivity Monitor, Instrument Science Report COS 2021-9

Fuhrmann, K., Pfeiffer, M. J., & Bernkopf, J. 1997, AAP, 326, 1081

Gaia Collaboration, Prusti, T., de Bruijne, J. H. J., et al. 2016, AAP, 595, A1

Gaia Collaboration, Brown, A. G. A., Vallenari, A., et al. 2018, AAP, 616, A1

Gao, P., Plavchan, P., Gagné, J., et al. 2016, PASP, 128, 104501

Gardner, L. D., Atkins, N., Fineschi, S., et al. 2000, in Society of Photo-Optical Instrumentation Engineers (SPIE) Conference Series, Vol. 4139, Instrumentation for UV/EUV Astronomy and Solar Missions, ed. S. Fineschi, C. M. Korendyke, O. H. Siegmund, & B. E. Woodgate, 362–369

Gardner, L. D., Kohl, J. L., Daigneau, P. S., et al. 1996, in Society of Photo-Optical Instrumentation Engineers (SPIE) Conference Series, Vol. 2831, Ultraviolet Atmospheric and Space Remote Sensing: Methods and Instrumentation, ed. R. E. Huffman & C. G. Stergis, 2–24

Gardner, L. D., Smith, P. L., Kohl, J. L., et al. 2002, ISSI Scientific Reports Series, 2, 161

Gibson, S., Barnes, S. I., Hearnshaw, J., et al. 2012, in ProcSPIE, Vol. 8446, Ground-based and Airborne Instrumentation for Astronomy IV, 844648

Gibson, S. E., & Low, B. C. 1998, ApJ, 493, 460

Gilly, C. R., & Cranmer, S. R. 2020, ApJ, 901, 150

Golub, L., Deluca, E., Austin, G., et al. 2007, SoPh, 243, 63

Gopalswamy, N., Yashiro, S., Michalek, G., et al. 2009, Earth Moon and Planets, 104, 295

Gosling, J. T., Hildner, E., MacQueen, R. M., et al. 1974, JGR, 79, 4581

Grevesse, N. 1984, Physica Scripta Volume T, 8, 49

Griffin, D. C., Pindzola, M. S., & Badnell, N. R. 1993, PhRvA, 47, 2871

Gruesbeck, J. R., Lepri, S. T., & Zurbuchen, T. H. 2012, ApJ, 760, 141

Gruesbeck, J. R., Lepri, S. T., Zurbuchen, T. H., & Antiochos, S. K. 2011, ApJ, 730, 103

Guedel, M., Benz, A. O., Schmitt, J. H. M. M., & Skinner, S. L. 1996, ApJ, 471, 1002

Gunn, A. G., Doyle, J. G., Mathioudakis, M., Houdebine, E. R., & Avgoloupis, S. 1994, A&A, 285, 489

Guo, W. P., & Wu, S. T. 1998, ApJ, 494, 419

Halverson, S., Roy, A., Mahadevan, S., et al. 2015, ApJ, 806, 61

Hansen, R. T., Garcia, C. J., Grognard, R. J. M., & Sheridan, K. V. 1971, PASA, 2, 57

Hawley, S. L., Fisher, G. H., Simon, T., et al. 1995, ApJ, 453, 464

Haywood, R. D., Collier Cameron, A., Unruh, Y. C., et al. 2016, MNRAS, 457, 3637

Hertzsprung, E. 1924, BAN, 2, 87

Hirayama, T. 1974, SoPh, 34, 323

Høg, E., Fabricius, C., Makarov, V. V., et al. 2000, AAP, 355, L27

Horne, K. 1986, PASP, 98, 609

Houdebine, E. R., Foing, B. H., & Rodono, M. 1990, AAP, 238, 249

Howard, A. W., Johnson, J. A., Marcy, G. W., et al. 2009, ApJ, 696, 75

Howard, R. A., & Vourlidas, A. 2018, SoPh, 293, 55

Hughes, J. P., & Helfand, D. J. 1985, ApJ, 291, 544

Hyder, C. L., & Lites, B. W. 1970, SoPh, 14, 147

Illing, R. M. E., & Hundhausen, A. J. 1985, JGR, 90, 275

Irwin, J., Charbonneau, D., Nutzman, P., & Falco, E. 2009, in IAU Symposium, Vol. 253, Transiting Planets, ed. F. Pont, D. Sasselov, & M. J. Holman, 37–43

Isaacson, H., & Fischer, D. 2010, ApJ, 725, 875

Joshi, N. C., Srivastava, A. K., Filippov, B., et al. 2013, ApJ, 771, 65

Kahler, S. 1994, ApJ, 428, 837

Kaiser, M. L. 2005, Advances in Space Research, 36, 1483

Kirk, M. S., Balasubramaniam, K. S., Jackiewicz, J., & Gilbert, H. R. 2017, in Fine Structure and Dynamics of the Solar Atmosphere, ed. S. Vargas Domínguez, A. G. Kosovichev, P. Antolin, & L. Harra, Vol. 327, 117–127

Ko, Y.-K., Raymond, J. C., Vrsnak, B., & Vujić, E. 2010, ApJ, 722, 625

Ko, Y. K., Vourlidas, A., Korendyke, C., & Laming, J. M. 2016, in AGU Fall Meeting Abstracts, SH43B–2569

Ko, Y. K., Raymond, J. C., Gibson, S. E., et al. 2005, ApJ, 623, 519

Kohl, J. L., Gardner, L. D., Strachan, L., & Hassler, D. M. 1994, SSRv, 70, 253

Kohl, J. L., Noci, G., Cranmer, S. R., & Raymond, J. C. 2006, AAPR, 13, 31

Kohl, J. L., Reeves, E. M., & Kirkham, B. 1978, in New Instrumentation for Space Astronomy, ed. K. A. van der Hucht & G. Vaiana, 91–94

Kohl, J. L., Weiser, H., Withbroe, G. L., et al. 1980, ApJL, 241, L117

Kohl, J. L., & Withbroe, G. L. 1982, ApJ, 256, 263

Kohl, J. L., Esser, R., Gardner, L. D., et al. 1995, SoPh, 162, 313

Kopp, R. A., & Pneuman, G. W. 1976, SoPh, 50, 85

Kosugi, T., Matsuzaki, K., Sakao, T., et al. 2007, SoPh, 243, 3

Kumar, A., & Rust, D. M. 1996, JGR, 101, 15667

Kurita, M., Kino, M., Iwamuro, F., et al. 2020, PASJ, 72, 48

Labadie-Bartz, J., Rodriguez, J. E., Stassun, K. G., et al. 2019, The Astrophysical Journal Supplement Series, 240, 13

Laming, J. M., Moses, J. D., Ko, Y.-K., et al. 2013, ApJ, 770, 73

Laming, J. M., & Vourlidas, A. 2019, in AGU Fall Meeting Abstracts, Vol. 2019, SH31B–15

Landi, E., Alexander, R. L., Gruesbeck, J. R., et al. 2012, ApJ, 744, 100

Landi, E., Raymond, J. C., Miralles, M. P., & Hara, H. 2010, ApJ, 711, 75

Lang, D., Hogg, D. W., Mierle, K., Blanton, M., & Roweis, S. 2010, AJ, 139, 1782

Latham, D. W., Mazeh, T., Stefanik, R. P., Mayor, M., & Burki, G. 1989, Nature, 339, 38

Lee, J. Y., Raymond, J. C., Ko, Y. K., & Kim, K. S. 2009, ApJ, 692, 1271

Lee, J.-Y., Raymond, J. C., Reeves, K. K., Moon, Y.-J., & Kim, K.-S. 2017, ApJ, 844, 3

Leitzinger, M., Odert, P., Ribas, I., et al. 2011, AAP, 536, A62

Lepri, S. T., Zurbuchen, T. H., Fisk, L. A., et al. 2001, JGR, 106, 29231

Leroy, J. L., Bommier, V., & Sahal-Brechot, S. 1983, SoPh, 83, 135

Liewer, P. C., de Jong, E. M., Hall, J. R., et al. 2009, SoPh, 256, 57

Line, M. R., Lothringer, J., Barman, T., et al. 2021, in American Astronomical Society Meeting Abstracts, Vol. 53, American Astronomical Society Meeting Abstracts, 428.02

Linker, J. A., Lionello, R., Mikić, Z., Titov, V. S., & Antiochos, S. K. 2011, ApJ, 731, 110

Linker, J. A., Mikić, Z., Lionello, R., et al. 2003, Physics of Plasmas, 10, 1971

Linker, J. A., Mikić, Z., Biesecker, D. A., et al. 1999, JGR, 104, 9809

Lionello, R., Downs, C., Linker, J. A., et al. 2019, SoPh, 294, 13

—. 2013, ApJ, 777, 76

Lionello, R., Linker, J. A., & Mikić, Z. 2009a, ApJ, 690, 902

—. 2009b, ApJ, 690, 902

Lionello, R., Linker, J. A., Mikić, Z., & Riley, P. 2006, ApJL, 642, L69

Lionello, R., Riley, P., Linker, J. A., & Mikić, Z. 2005, ApJ, 625, 463

Loyd, P., Shkolnik, E., Ardila, D., et al. 2021, in American Astronomical Society Meeting Abstracts, Vol. 53, American Astronomical Society Meeting Abstracts, 505.04

Lund, M. B., Rodriguez, J. E., Zhou, G., et al. 2017, AJ, 154, 194

Ma, S., Raymond, J. C., Golub, L., et al. 2011, ApJ, 738, 160

Malkin, Z. M. 2011, Kinematics and Physics of Celestial Bodies, 27, 42

Masai, K. 1984, AP&SS, 98, 367

Masuda, S., Kosugi, T., Hara, H., Tsuneta, S., & Ogawara, Y. 1994, Nature, 371, 495

Mayor, M., & Queloz, D. 1995, Nature, 378, 355

Meyer, J. P. 1985, ApJS, 57, 151

Mikić, , Z., Downs, C., et al. 2018, Nature Astronomy, 2, 913

Mikić, Z., Linker, J. A., Schnack, D. D., Lionello, R., & Tarditi, A. 1999, Physics of Plasmas, 6, 2217

Milligan, R. O., & Dennis, B. R. 2009, ApJ, 699, 968

Milligan, R. O., Gallagher, P. T., Mathioudakis, M., et al. 2006, ApJL, 638, L117

Moschou, S.-P., Drake, J. J., Cohen, O., et al. 2019, ApJ, 877, 105

Murphy, N. A., Raymond, J. C., & Korreck, K. E. 2011, ApJ, 735, 17

Namekata, K., Maehara, H., Honda, S., et al. 2021, Nature Astronomy, 6, 241

Nave, G. 2011, in Imaging and Applied Optics (Optical Society of America), FTuA1

Noci, G., Kohl, J. L., & Withbroe, G. L. 1987, ApJ, 315, 706

Noyes, R. W., Hartmann, L. W., Baliunas, S. L., Duncan, D. K., & Vaughan, A. H. 1984, ApJ, 279, 763

Olsen, E. L., Leer, E., & Holzer, T. E. 1994, ApJ, 420, 913

Osten, R. A., & Wolk, S. J. 2017, in Living Around Active Stars, ed. D. Nandy, A. Valio, & P. Petit, Vol. 328, 243–251

O'Toole, S. J., Tinney, C. G., & Jones, H. R. A. 2008, MNRAS, 386, 516

Pallavicini, R., Serio, S., & Vaiana, G. S. 1977, ApJ, 216, 108

Pandey, J. C., & Singh, K. P. 2012, MNRAS, 419, 1219

Parenti, S., Schmieder, B., Heinzel, P., & Golub, L. 2012, ApJ, 754, 66

Parker, E. N. 1955, ApJ, 122, 293

Payne, C. H. 1925, PhD thesis, RADCLIFFE COLLEGE.

Pepe, F., Lovis, C., Ségransan, D., et al. 2011, AAP, 534, A58

Pepper, J., Rodriguez, J. E., Collins, K. A., et al. 2017, AJ, 153, 215

Pernechele, C., Naletto, G., Nicolosi, P., et al. 1997, ApOpt, 36, 813

Piskunov, N. E., & Valenti, J. A. 2002, AAP, 385, 1095

Rakowski, C. E., Laming, J. M., & Lepri, S. T. 2007, ApJ, 667, 602

Raymond, J. C. 1990, ApJ, 365, 387

—. 1999, SSRv, 87, 55

Raymond, J. C., & Ciaravella, A. 2004, ApJL, 606, L159

Raymond, J. C., & Doyle, J. G. 1981, ApJ, 245, 1141

Raymond, J. C., & Smith, B. W. 1977, ApJS, 35, 419

Raymond, J. C., Kohl, J. L., Noci, G., et al. 1997, SoPh, 175, 645

Reeves, K. K., Linker, J. A., Mikić, Z., & Forbes, T. G. 2010, ApJ, 721, 1547

Reeves, K. K., McCauley, P. I., & Tian, H. 2015, ApJ, 807, 7

Reeves, K. K., Török, T., Mikić, Z., Linker, J., & Murphy, N. A. 2019, ApJ, 887, 103

Ricker, G. R., Winn, J. N., Vanderspek, R., et al. 2014, in Society of Photo-Optical Instrumentation Engineers (SPIE) Conference Series, Vol. 9143, Space Telescopes and Instrumentation 2014: Optical, Infrared, and Millimeter Wave, ed. J. Oschmann, Jacobus M., M. Clampin, G. G. Fazio, & H. A. MacEwen, 914320

Riddle, R. L., Burse, M. P., Law, N. M., et al. 2012, in Adaptive Optics Systems III, Vol. 8447, 84472O

Rivera, Y. J., Landi, E., & Lepri, S. T. 2019a, ApJS, 243, 34

Rivera, Y. J., Landi, E., Lepri, S. T., & Gilbert, J. A. 2019b, ApJ, 874, 164

Rodriguez, J. E., Zhou, G., Cargile, P. A., et al. 2017, ApJ, 836, 209

Rodriguez, J. E., Eastman, J. D., Zhou, G., et al. 2019, arXiv e-prints, arXiv:1906.03276

Rottman, G., Woods, T., Snow, M., & DeToma, G. 2001, Advances in Space Research, 27, 1927

Saar, S. H., & Donahue, R. A. 1997, ApJ, 485, 319

Schlafly, E. F., & Finkbeiner, D. P. 2011, ApJ, 737, 103

Scholz, T. T., & Walters, H. R. J. 1991, ApJ, 380, 302

Scolini, C., Chané, E., Temmer, M., et al. 2020, ApJS, 247, 21

Shen, C., Raymond, J. C., Murphy, N. A., & Lin, J. 2015, Astronomy and Computing, 12, 1

Shkolnik, E. L., Ardila, D. R., Barman, T., et al. 2021, in American Astronomical Society Meeting Abstracts, Vol. 53, American Astronomical Society Meeting Abstracts, 231.02

Siverd, R. J., Collins, K. A., Zhou, G., et al. 2018, AJ, 155, 35

Solanki, S. K., Lagg, A., Woch, J., Krupp, N., & Collados, M. 2003, Nature, 425, 692

Strachan, L., Gardner, L. D., Hassler, D. M., & Kohl, J. L. 1994, SSRv, 70, 263

Strachan, L., Panasyuk, A. V., Kohl, J. L., & Lamy, P. 2012, ApJ, 745, 51

Strachan, L., Laming, J. M., Ko, Y.-K., et al. 2017, in AAS/Solar Physics Division Meeting, Vol. 48, AAS/Solar Physics Division Abstracts #48, 110.07

Sturrock, P. A. 1966, Nature, 211, 695

Swift, J. J., Bottom, M., Johnson, J. A., et al. 2015, Journal of Astronomical Telescopes, Instruments, and Systems, 1, 027002

Szentgyorgyi, A. H., Geary, J. G., Latham, D. W., et al. 2005, in Bulletin of the American Astronomical Society, Vol. 37, American Astronomical Society Meeting Abstracts, 1339

Taylor, J. B. 1974, Phys. Rev. Lett., 33, 1139

Teriaca, L., Falchi, A., Cauzzi, G., et al. 2003, ApJ, 588, 596

Tokovinin, A., Fischer, D. A., Bonati, M., et al. 2013, Publications of the Astronomical Society of the Pacific, 125, 1336

Török, T., Downs, C., Linker, J. A., et al. 2018, ApJ, 856, 75

Tousey, R., Bartoe, J. D. F., Bohlin, J. D., et al. 1973, SoPh, 33, 265

Tsuneta, S., Hara, H., Shimizu, T., et al. 1992, PASJ, 44, L63

Tsuneta, S., Acton, L., Bruner, M., et al. 1991, SoPh, 136, 37

Usmanov, A. V., & Dryer, M. 1995, SoPh, 159, 347

Valenti, J. A., Butler, R. P., & Marcy, G. W. 1995, PASP, 107, 966

Valenti, J. A., & Fischer, D. A. 2005, The Astrophysical Journal Supplement Series, 159, 141

Vanderburg, A., Johnson, J. A., Rappaport, S., et al. 2015, Nature, 526, 546

Vernazza, J. E., & Reeves, E. M. 1978, ApJS, 37, 485

Vida, K., Leitzinger, M., Kriskovics, L., et al. 2019, AAP, 623, A49

Vogt, S. S. 1987, Publications of the Astronomical Society of the Pacific, 99, 1214

Vogt, S. S., Allen, S. L., Bigelow, B. C., et al. 1994, in Society of Photo-Optical Instrumentation Engineers (SPIE) Conference Series, Vol. 2198, Instrumentation in Astronomy VIII, ed. D. L. Crawford & E. R. Craine, 362

Vourlidas, A., Howard, R. A., Esfandiari, E., et al. 2010, ApJ, 722, 1522

Wang, S. X. 2016, PhD thesis, The Pennsylvania State University

Wilson, M. L., Raymond, J. C., Lepri, S. T., et al. 2022, ApJ, 927, 27

Wilson, O. C. 1978, ApJ, 226, 379

Winn, J. N. 2010, arXiv e-prints, arXiv:1001.2010

Withbroe, G. L. 1988, ApJ, 325, 442

Wright, E. L., Eisenhardt, P. R. M., Mainzer, A. K., et al. 2010, AJ, 140, 1868

Wright, J. T. 2005, Publications of the Astronomical Society of the Pacific, 117, 657

Wright, J. T., & Eastman, J. D. 2014, Publications of the Astronomical Society of the Pacific, 126, 838

Wright, J. T., Marcy, G. W., Butler, R. P., & Vogt, S. S. 2004, The Astrophysical Journal Supplement Series, 152, 261

Wright, J. T., & Robertson, P. 2017, Research Notes of the American Astronomical Society, 1, 51

Wright, N. J., Drake, J. J., Mamajek, E. E., & Henry, G. W. 2011, ApJ, 743, 48

Yashiro, S., & Gopalswamy, N. 2009, in Universal Heliophysical Processes, ed. N. Gopalswamy & D. F. Webb, Vol. 257, 233–243

Zechmeister, M., Anglada-Escudé, G., & Reiners, A. 2014, AAP, 561, A59

Zuccarello, F. P., Chandra, R., Schmieder, B., Aulanier, G., & Joshi, R. 2017, AAP, 601, A26